

Abayomi David OYELEYE

**Experimental and Numerical Analysis
of Wooden Structures for Sustainable
Means of Transport: IMOCA Boats
and Bicycle Frame**



FRP++

Advanced structural analysis and
design using composite materials

Master Dissertation
European Master Advanced Structural Analysis
and Design using Composite Materials

Work developed under the supervision of
Professor Bruno CASTANIE



Funded by
the European Union

DECLARATION

Name: Abayomi David OYELEYE

Email: oyeleyeabayomi64@gmail.com **Phone number:** +33687659862

Citizen Card Number: XXXXXXXXXXXXXXXXXXXXXXXX

Title of the Thesis: Experimental and Numerical Analysis of Wooden Structures for Sustainable Means of Transport: IMOCA Boats and Bicycle Frame

Supervisors:

Professor Bruno CASTANIE

[Categoria]

Year of Conclusion: 2025

Master Course in Advanced Structural Analysis and Design using Composite Materials

THE ENTIRE REPRODUCTION OF THIS THESIS IS AUTHORIZED ONLY FOR RESEARCH PURPOSES, UPON WRITTEN DECLARATION BY THE INTERESTED PERSON, WHICH IS COMMITTED TO.

University of Toulouse III Paul Sabatier, 01/09/2025

Signature: 

ACKNOWLEDGEMENTS

I would like to express my heartfelt gratitude, first and foremost, to God Almighty, who made it possible for me to begin and successfully complete this important phase of my life.

I am deeply thankful for the support I have received—academically, emotionally, and financially—through the Erasmus+ Master’s Programme of the European Union. This support, especially the financial assistance, made it possible for someone from a humble background like me to pursue a Master’s degree, not just within my country, but in Europe. It also marked my very first trip outside Nigeria, my home country. This unique opportunity has allowed me to meet brilliant minds, expand my network, and significantly broaden my academic horizons and perspective on life.

I want to extend my sincere appreciation to the entire FRP++ teaching team. Your collective wealth of knowledge, dedication, and passion for teaching has played a vital role in shaping my academic journey. Each course added a new layer to my understanding and growth, and I am truly grateful for the privilege of learning from you all. In particular, I would like to thank Prof. Cristina Barris, for being such a kind, welcoming, and approachable person. I also deeply appreciate Prof. Norbert Blanco, who generously gave his time outside class hours to help me understand areas of his course that I initially struggled with.

I sincerely thank my amazing supervisor, Professor Bruno Castanié, who was always there for me. He consistently followed up on my progress at every stage and never failed to offer his technical expertise and guidance whenever I needed it.

Special thanks to the incredible PhD student, Anthony Viste, who was undoubtedly God-sent. He was always willing to demystify complex concepts and provided constant support, especially in teaching me software tools I had never used before the start of this thesis.

I thank God for blessing me with a supportive family and wonderful friends, who stood by me in moments when I felt emotionally and mentally drained—lifting me through prayers, encouragement, and kind words.

To all my colleagues in the FRP++ 2024/25 cohort, thank you for being a vital part of my journey. Your support, collaboration, and shared experiences pushed me beyond my limits and inspired me in many ways. As the program draws to a close, I know I will deeply miss each and every one of you.

Lastly, I would like to appreciate myself for persevering through tough times, overcoming inner struggles and doubts, and staying committed to the goal till the very end.

Analyse expérimentale et numérique des structures en bois pour les moyens de transport durables : bateaux IMOCA et cadres de vélo

RÉSUMÉ

La demande croissante de matériaux de transport durables a suscité un regain d'intérêt pour le bois et les composites à base de bois comme alternative aux métaux traditionnels et aux fibres synthétiques. Cette thèse utilise une combinaison d'approches expérimentales et numériques pour étudier le comportement mécanique de structures sandwich en bois de chêne et en contreplaqué. Deux études de cas ont été menées : (i) un cadre de vélo en chêne à échelle réelle renforcé par des couches internes de verre E, et (ii) des éprouvettes sandwich à âme en contreplaqué inspirées des bateaux de course IMOCA, avec des feuilles de surface en carbone, basalte et fibre de verre. Les essais expérimentaux ont impliqué des bancs d'essai sur mesure pour évaluer la rigidité des vélos et des essais de flexion conformes à la norme ASTM pour les panneaux sandwich. Des modèles par éléments finis ont été développés dans Abaqus/CAE pour reproduire les configurations de chargement, et un post-traitement a été effectué en Python pour évaluer la rupture selon le critère de Tsai-Wu.

Les résultats ont montré que la charpente en chêne conservait ses performances élastiques sous charge statique, avec des valeurs de rigidité conformes aux exigences fonctionnelles. Cependant, des concentrations de contraintes ont été observées aux interfaces acier-bois. Les essais sur panneaux sandwich ont confirmé que le renforcement par fibres améliore significativement la capacité de flexion et la rigidité, la fibre de verre offrant les gains de résistance les plus rentables, le basalte excellant en rigidité et le carbone offrant une performance intermédiaire. Si les simulations numériques ont permis de saisir les tendances du comportement élastique, leurs prédictions de rigidité divergeaient en raison de l'idéalisation des conditions limites et de l'incertitude des données sur les matériaux.

Dans l'ensemble, ces résultats confirment le potentiel des structures en bois comme alternative durable pour les applications de mobilité, tout en soulignant l'importance d'une caractérisation précise des matériaux, du détail des assemblages et de la modélisation des défaillances pour une conception fiable.

MOTS-CLES: Transport durable, Bois de chêne, Panneaux sandwich, Cadre de vélo, Analyse par éléments finis, Critère de Tsai–Wu.

Experimental and Numerical Analysis of Wooden Structures for Sustainable Means of Transport: IMOCA Boats and Bicycle Frame

ABSTRACT

The growing demand for sustainable transport materials has sparked renewed interest in wood and wood-based composites as an alternative to traditional metals and synthetic fibres. This thesis uses a combination of experimental and numerical approaches to investigate the mechanical behaviour of oak wood and plywood-based sandwich structures. Two case studies were conducted: (i) a full-scale oak bicycle frame reinforced with internal E-glass layers, and (ii) plywood-core sandwich specimens inspired by IMOCA racing boats, with face-sheets made of carbon, basalt and glass fibre. Experimental testing involved custom-designed rigs to assess bicycle stiffness and ASTM-standard flexural tests for sandwich panels. Finite element models were developed in Abaqus/CAE to replicate the loading configurations, and post-processing was performed using Python to evaluate failure based on the Tsai–Wu criterion.

The results showed that the oak frame maintained elastic performance under static loading, with stiffness values consistent with functional requirements. However, stress concentrations were observed at the steel–wood interfaces. Sandwich panel tests confirmed that fibre reinforcement significantly improves flexural capacity and stiffness, with glass fibre offering the most cost-effective strength gains, basalt excelling in stiffness and carbon providing an intermediate performance. While numerical simulations captured elastic behaviour trends, they diverged in stiffness predictions due to boundary condition idealisation and uncertainty in material data.

Overall, these findings confirm the potential of wooden structures as a sustainable alternative for mobility applications, while emphasising the importance of accurately characterising materials, detailing joints, and modelling failure for reliable design.

KEYWORDS: Sustainable transport, Oak wood, Sandwich panels, Bicycle frame, Finite element analysis, Tsai–Wu criterion.

TABLE OF CONTENTS

Cover.....	i
DECLARATION	ii
Acknowledgements	III
Résumé	IV
Abstract	V
Table of Contents	VI
List of Figures	VIII
List of Tables.....	XI
List of Abbreviations and Symbols.....	XII
1. Introduction.....	15
1.1. Wooden Structures as Material for Means of Transport (Boats and Bicycle Frame) Overview	15
1.2. Motivation	17
1.3. Research aim and objectives.....	17
1.3.1. Scope of the Study.....	18
1.3.2. Significance of the Study	18
1.4. Structure of the dissertation.....	18
2. LITERATURE REVIEW	21
2.1. OVERVIEW OF THE MECHANICAL BEHAVIOUR OF OAK WOOD.....	21
2.2. Failure mode of wooden material.....	24
2.3. FEM Failure Criteria mode study of Wood.....	28
2.4. Bicycle Frame: Materials, Loading, stiffness and test setup	30
2.4.1. Evolution and Selection of Frame Materials.....	30
2.4.2. Load Conditions and Structural Demands	32
2.4.3. Stiffness Evaluation, Frame Performance and Test Rig Design	32
2.4.4. Numerical and Experimental Correlation	33
2.5. Sandwich Panel Design and Marine Applications	33
2.5.1. Plywood based core Sandwich Panel Mechanical Performance	35
2.5.2. Wood Based Sandwich structure in Marine Application	36

2.6.	Failure Modes and Testing Relevance.....	37
3.	METHODOLOGY	39
3.1.	Overview	39
3.2.	Case Study 1: Bicycle Frame.....	40
3.2.1.	Materials and Construction	40
3.2.2.	Reverse Engineering and Numerical Modelling of Bicycles Frame	42
3.2.3.	Finite Element Model (FEM) Boundary condition and Load Application	43
3.2.4.	Post-Processing and Failure Evaluation.....	44
3.2.5.	Experimental Testing of the Bicycle Frame.....	45
3.3.	Case Study 2: IMOCA Sandwich Specimens.....	47
3.3.1.	Experimental Procedures and Equations.....	47
3.3.2.	Numerical Model Setup	51
4.	RESULTS AND DISCUSSIONS.....	53
4.1.	Case Study 1: Wooden Bicycle Frame	53
4.1.1.	Bicycle Experimental Stiffness Results	53
4.1.2.	FEM Stiffness Predictions and Correlation.....	54
4.1.3.	Post Processing for failure assessment.....	62
4.1.4.	Experimental and FEM Validation	66
4.2.	Case Study 2: IMOCA Sandwich Specimens.....	67
4.2.1.	Experimental Flexural Test (3-point and 4-Point) Results.....	67
4.2.2.	FEM Predictions and Comparison	83
5.	Conclusions and further developments.....	85
5.1.	Main conclusions.....	85
5.1.1.	Wooden bicycle frame	85
5.1.2.	IMOCA sandwich specimens.....	86
5.1.3.	General outcomes	86
5.2.	Further developments	87
	<i>References</i>	88
	Annex I.....	93
	Annex II.....	97

LIST OF FIGURES

FIGURE 1.1: GREENHOUSE GAS EMISSIONS FROM TRANSPORT IN THE EU BY TRANSPORT MODE (2019). SOURCE: EUROPEAN ENVIRONMENT AGENCY, 2022[7].	16
FIGURE 1.2: EVOLUTION OF CO ₂ EMISSIONS FROM NEW PASSENGER CARS IN THE EU (2010–2030). SOURCE: EUROSTAT AND EUROPEAN ENVIRONMENT AGENCY, 2021[7].	16
FIGURE 2.1: THREE PRINCIPAL AXES OF WOOD WITH RESPECT TO GRAIN DIRECTION AND GROWTH RINGS[8]	21
FIGURE 2.2: STATIC BENDING TEST SPECIMEN WITH ACOUSTIC EMISSION SENSOR ATTACHED[10]	24
FIGURE 2.3: TYPICAL BICYCLE FRAMES PART LABEL [1]	31
FIGURE 2.4: DIFFERENT CORE STRUCTURES IN SANDWICH COMPOSITES[28]	34
FIGURE 3.1: METHODOLOGY PROCESS FOR BOTH STUDY CASES	39
FIGURE 3.2: WOODEN BIKE FRAME FOR TEST	42
FIGURE 3.3: SCANNED IMAGE OF TEST BIKE FRAME STL FILE	43
FIGURE 3.4: REVERSED ENGINEERING OF TEST BIKE FRAME STP FILE	43
FIGURE 3.5: LOAD APPLICATION AND BOUNDARY CONDITIONS FOR THE BICYCLE FRAME STIFFNESS TESTS: (A) HEAD TUBE – LOAD APPLICATION, (B) BOTTOM BRACKET – LOAD APPLICATION, (C) REAR TRIANGLE – LOAD APPLICATION, (D) HEAD TUBE – BOUNDARY CONDITIONS, (E) BOTTOM BRACKET – BOUNDARY CONDITIONS, (F) REAR TRIANGLE – BOUNDARY CONDITIONS.	44
FIGURE 3.6: DETAILED DESIGN OF TEST RIG FOR BICYCLE STIFFNESS ASSESSMENT	46
FIGURE 3.7: LABORATORY SET-UP OF BICYCLE TEST RIG FOR HEAD TUBE STIFFNESS CHECK	46
FIGURE 3.8: LABORATORY SET-UP OF BICYCLE TEST RIG FOR BOTTOM BRACKET STIFFNESS CHECK	46
FIGURE 3.9: LABORATORY SET-UP OF BICYCLE TEST RIG FOR REAR TRIANGLE STIFFNESS CHECK	47
FIGURE 3.10: UNIVERSAL TESTING MACHINE WITH 3-POINT FLEXURAL TEST CONFIGURATION	48
FIGURE 3.11: FLEXURE TEST CONFIGURATION (A) 3-POINT CONFIGURATION (B) 4-POINT CONFIGURATION	49
FIGURE 3.12: MICROSCOPIC IMAGE OF IMOCA SPECIMEN SHOWING EACH PLY THICKNESS (A) SANDWICH WITH PLYWOOD CORE AND BASALT FACE-SHEET (B) CONTROL SPECIMEN OF PLYWOOD ONLY ORIENTATED AT 0° AND 90°	52
FIGURE 3.13: BENDING TEST MODEL SET-UP (A) 3-POINT FLEXURAL TEST (B) 4-POINT FLEXURAL TEST	52
FIGURE 4.1: BOTTOM BRACKET STIFFNESS EXPERIMENTAL LOAD-DISPLACEMENT CURVE	53
FIGURE 4.2: REAR TRIANGLE STIFFNESS EXPERIMENTAL LOAD-DISPLACEMENT CURVE	54
FIGURE 4.3: HEAD TUBE LOAD RESPONSE STRESS DISTRIBUTION DIAGRAM: (A) NORMAL STRESS DISTRIBUTION IN S11 DIRECTION, (B) NORMAL STRESS DISTRIBUTION IN S22 DIRECTION, (C) NORMAL STRESS DISTRIBUTION IN S33 DIRECTION, (D) SHEAR STRESS DISTRIBUTION IN S12 DIRECTION	55

FIGURE 4.4: HEAD TUBE LOAD RESPONSE DISPLACEMENT DIAGRAM: (A) GLOBAL MAXIMUM DEFLECTION, (B) DEFLECTION RESPONSE IN THE U1 DIRECTION, (C) DEFLECTION RESPONSE IN THE U2 DIRECTION, (D)) DEFLECTION RESPONSE IN THE U3 DIRECTION	56
FIGURE 4.5: BOTTOM BRACKET LOAD RESPONSE STRESS DISTRIBUTION DIAGRAM: (A) NORMAL STRESS DISTRIBUTION IN S11 DIRECTION, (B) NORMAL STRESS DISTRIBUTION IN S22 DIRECTION, (C) NORMAL STRESS DISTRIBUTION IN S33 DIRECTION, (D) SHEAR STRESS DISTRIBUTION IN S23 DIRECTION.....	57
FIGURE 4.6: BOTTOM BRACKET LOAD RESPONSE DISPLACEMENT DIAGRAM: (A) GLOBAL MAXIMUM DEFLECTION, (B) DEFLECTION RESPONSE IN THE U1 DIRECTION, (C) DEFLECTION RESPONSE IN THE U2 DIRECTION, (D)) DEFLECTION RESPONSE IN THE U3 DIRECTION.....	59
FIGURE 4.7: REAR TRIANGLE LOAD RESPONSE STRESS DISTRIBUTION DIAGRAM: (A) NORMAL STRESS DISTRIBUTION IN S11 DIRECTION, (B) NORMAL STRESS DISTRIBUTION IN S22 DIRECTION, (C) NORMAL STRESS DISTRIBUTION IN S33 DIRECTION, (D) SHEAR STRESS DISTRIBUTION IN S23 DIRECTION.....	60
FIGURE 4.8: REAR TRIANGLE LOAD RESPONSE DISPLACEMENT DIAGRAM: (A) GLOBAL MAXIMUM DEFLECTION, (B) DEFLECTION RESPONSE IN THE U1 DIRECTION, (C) DEFLECTION RESPONSE IN THE U2 DIRECTION, (D)) DEFLECTION RESPONSE IN THE U3 DIRECTION	61
FIGURE 4.9: PYTHON CUSTOM TSAI-WU FAILURE CHECK OUTPUT: (A) HEAD TUBE FAILED ELEMENT RESULTS (B) BOTTOM BRACKET TUBE FAILED ELEMENT RESULTS (C) REAR TRIANGLE FAILED ELEMENT RESULTS	63
FIGURE 4.10: STRESS CONTOUR OF WOODEN SECTION OF FRAME ONLY BASED ON STIFFNESS CHECK	63
FIGURE 4.11: STRESS CONTOUR OR REAR DROPOUT	64
FIGURE 4.12: DEFLECTION CONTOUR OF REAR DROPOUT	64
FIGURE 4.13: VISUALIZATION OF STRESS CONCENTRATION OF FAILED ELEMENTS FROM REAR TRIANGLE STIFFNESS CHECK.....	65
FIGURE 4.14: BOTTOM BRACKET EXPERIMENTAL AND FEM FORCE-DISPLACEMENT COMPARISM.....	66
FIGURE 4.15: REAR TRIANGLE EXPERIMENTAL AND FEM FORCE-DISPLACEMENT COMPARISM	67
FIGURE 4.16: FORCE-DISPLACEMENT GRAPH FOR PURE PLYWOOD UNDER A 3-POINT FLEXURAL TEST	68
FIGURE 4.17: FORCE-DISPLACEMENT GRAPH FOR BASALT 0 DEGREE UNDER A 3-POINT FLEXURAL TEST	68
FIGURE 4.18: FORCE-DISPLACEMENT GRAPH FOR GLASS 0 DEGREE UNDER A 3-POINT FLEXURAL TEST	69
FIGURE 4.19:FORCE-DISPLACEMENT GRAPH FOR CARBON 0 DEGREE UNDER A 3-POINT FLEXURAL TEST	69
FIGURE 4.20: 3-POINT FLEXURAL AFTER TEST IMAGE OF SPECIMENS : (A) PURE PLYWOOD (B) BASALT FACE-SHEET 0 DEGREE (C) GLASS FACE-SHEET 0 DEGREE (D) CARBON FACE-SHEET 0 DEGREE	70
FIGURE 4.21: FORCE-DISPLACEMENT GRAPH FOR PURE PLYWOOD UNDER A 4-POINT FLEXURAL TEST.....	72
FIGURE 4.22: FORCE-DISPLACEMENT GRAPH FOR BASALT 0 DEGREE UNDER A 4-POINT FLEXURAL TEST	72
FIGURE 4.23: FORCE-DISPLACEMENT GRAPH FOR GLASS 0 DEGREE UNDER A 4-POINT FLEXURAL TEST	73
FIGURE 4.24: FORCE-DISPLACEMENT GRAPH FOR CARBON 0 DEGREE UNDER A 4-POINT FLEXURAL TEST	73
FIGURE 4.25: 4-POINT FLEXURAL AFTER TEST IMAGE OF SPECIMENS : (A) PURE PLYWOOD (B) BASALT FACE-SHEET 0 DEGREE (C) GLASS FACE-SHEET 0 DEGREE (D) CARBON FACE-SHEET 0 DEGREE	74
FIGURE 4.26:FORCE-DISPLACEMENT GRAPH FOR BASALT 90 DEGREE UNDER A 3-POINT FLEXURAL TEST	76
FIGURE 4.27: FORCE-DISPLACEMENT GRAPH FOR GLASS 90 DEGREE UNDER A 3-POINT FLEXURAL TEST	76

FIGURE 4.28: FORCE-DISPLACEMENT GRAPH FOR CARBON 90 DEGREE UNDER A 3-POINT FLEXURAL TEST	77
FIGURE 4.29: 3-POINT FLEXURAL AFTER TEST IMAGE OF SPECIMENS : (A) BASALT FACE-SHEET 90 DEGREE (B) GLASS FACE-SHEET 90 DEGREE (C) CARBON FACE-SHEET 90 DEGREE	78
FIGURE 4.30: FORCE-DISPLACEMENT GRAPH FOR BASALT 90 DEGREE UNDER A 4-POINT FLEXURAL TEST	79
FIGURE 4.31: FORCE-DISPLACEMENT GRAPH FOR GLASS 90 DEGREE UNDER A 4-POINT FLEXURAL TEST	80
FIGURE 4.32: FORCE-DISPLACEMENT GRAPH FOR CARBON 90 DEGREE UNDER A 4-POINT FLEXURAL TEST	80
FIGURE 4.33: 4-POINT FLEXURAL AFTER TEST IMAGE OF SPECIMENS : (A) BASALT FACE-SHEET 90 DEGREE (B) GLASS FACE-SHEET 90 DEGREE (C) CARBON FACE-SHEET 90 DEGREE	81
FIGURE 4.34: FEM SIMULATION FOR SANDWICH SPECIMEN (A) 0-DEGREE (B) 90-DEGREE	83
FIGURE 5.1: SUMMARY OF MAXIMUM FORCE CAPACITY FOR EACH SANDWICH SPECIMEN	86
FIGURE 5.2: B1 B45 T10	93
FIGURE 5.3: B1 BOIS F3 5	93
FIGURE 5.4: B2 B0 T5	93
FIGURE 5.5: B3 B90 F3 10.....	93
FIGURE 5.6: B3 B90 F4 5.....	93
FIGURE 5.7: B4 B0 F3 10.....	93
FIGURE 5.8: B4 B0 F4 5	94
FIGURE 5.9: C1 BOIS F4 6	94
FIGURE 5.10: C1 C45 T5.....	94
FIGURE 5.11: C2 C0 T1.....	94
FIGURE 5.12: C2 C90 T9.....	94
FIGURE 5.13: C3 C90 F3 5.....	94
FIGURE 5.14: C3 C90 F4 TEST	95
FIGURE 5.15: C4 C0 F3 10.....	95
FIGURE 5.16: C4 C0 F4 5.....	95
FIGURE 5.17: CPO T10.....	95
FIGURE 5.18: V1 V45 T1	95
FIGURE 5.19: V2 V0 T5	95
FIGURE 5.20: V3 V90 F3 6	96
FIGURE 5.21: V4 V0 F3 5	96

LIST OF TABLES

TABLE 1: COMPARISM OF FAILURE CRITERIA MODEL AND THE STANDARD ERROR[15]	29
TABLE 2: OAK, RED BLACK WOOD MECHANICAL PROPERTIES[8], [38]	41
TABLE 3: MECHANICAL PROPERTY OF INTERNAL UD- GLASS LAMINATE	42
TABLE 4: TEST MATRIX OF PLYWOOD CORE BASED SANDWICH STRUCTURES FOR QUASI-STATIC BENDING TEST (3P-3 POINTS, 4P-4 POINTS) WITH DIFFERENT FACE-SHEET AND CONTROL SPECIMEN	49
TABLE 5: FLEXURAL AND TENSILE TEST EQUATIONS	50
TABLE 6: SANDWICH FACE-SHEET MECHANICAL PROPERTY	52
TABLE 7: HEAD TUBE SUMMARY TABLE OF THE MAXIMUM STRESS DISTIBUTION AND DIRECTION OF STRESSES	55
TABLE 8: HEAD TUBE SUMMARY TABLE OF THE MAXIMUM DEFLECTIONS IN VARIOUS DIRECT	56
TABLE 9: BOTTOM BRACKET SUMMARY TABLE OF THE MAXIMUM STRESS DISTIBUTION AND DIRECTION OF STRESSES	58
TABLE 10: BOTTOM BRACKET SUMMARY TABLE OF THE MAXIMUM DEFLECTIONS IN VARIOUS DIRECTION	59
TABLE 11: REAR TRIANGLE SUMMARY TABLE OF THE MAXIMUM STRESS DISTIBUTION AND DIRECTION OF STRESSES	60
TABLE 12: REAR TRIANGLE SUMMARY TABLE OF THE MAXIMUM DEFLECTIONS IN VARIOUS DIRECTION	62
TABLE 13: SUMMARY OF STRESSES COMPUTATION RESULTS FOR SPECIMEN GROUP OF 0 DEGREE, 3-POINT AND THE COV(IN %)	70
TABLE 14: SUMMARY OF STRESSES COMPUTATION RESULTS FOR SPECIMEN GROUP OF 0 DEGREE, 4-POINT AND THE COV(IN %)	74
TABLE 15: SUMMARY OF STRESSES COMPUTATION RESULTS FOR SPECIMEN GROUP OF 90 DEGREE, 3-POINT AND THE COV(IN %)	77
TABLE 16: SUMMARY OF STRESSES COMPUTATION RESULTS FOR SPECIMEN GROUP OF 90 DEGREE, 4-POINT AND THE COV(IN %)	81

LIST OF ABBREVIATIONS AND SYMBOLS

Abbreviations

AE – Acoustic Emission
CAD – Computer-Aided Design
CAE – Computer-Aided Engineering
DIC – Digital Image Correlation
FEM – Finite Element Method
FEA – Finite Element Analysis
FRP – Fiber Reinforced Polymer
IMOCA – International Monohull Open Class Association
LVL – Laminated Veneer Lumber
MOE – Modulus of Elasticity
MOR – Modulus of Rupture
COV – Coefficient of Variation
SS – Sum of Squared errors

Standards and Test Methods

ASTM D6272 – Standard Test Method for Flexural Properties of Unreinforced and Reinforced Plastics (4-Point Bending)
ASTM D790 – Standard Test Method for Flexural Properties of Plastics and Composites
ASTM C393 – Standard Test Method for Flexural Properties of Sandwich Constructions
ISO 4210 – Safety Requirements for Bicycles

Symbols

E – Elastic modulus (Young's modulus)
 E_1 – Longitudinal modulus (parallel to grain/fibre direction)
 E_2, E_3 – Transverse moduli (perpendicular to grain/fibre)
 G – Shear modulus
 G_{12}, G_{13}, G_{23} – Shear moduli in respective planes
 ν – Poisson's ratio
 $\nu_{12}, \nu_{13}, \nu_{23}$ – Poisson's ratios in material directions
 σ – Normal stress

σ_1 – Stress parallel to fibre/grain direction
 σ_2, σ_3 – Stresses in transverse directions
 τ – Shear stress
 $\tau_{12}, \tau_{13}, \tau_{23}$ – Shear stresses in respective planes
 S – Shear Strength
 X_t – Tensile strength parallel to grain
 X_c – Compressive strength parallel to grain
 Y_t – Transverse Tensile strength
 Y_c – Transverse Compressive strength
 FI – Failure Index (Tsai–Wu criterion)
 P – Applied load/force
 δ – Displacement/deflection
 K – Stiffness (N/mm)

THIS PAGE WAS INTENTIONALLY LEFT BLANK

1. INTRODUCTION

1.1. Wooden Structures as Material for Means of Transport (Boats and Bicycle Frame) Overview

The utilization of wood as a medium for bicycle frames can be traced back several centuries, with the earliest models dating back to the 1800s, including the Von Draisienne and other equine-drawn vehicles. Although metal construction became predominant in the late 19th century, wood continued to be used intermittently for frames, rims, and mudguards until the 1930s. Contemporary frames are predominantly composed of aluminium, steel, titanium, and carbon fibre; however, some less prevalent materials, such as bamboo, are also utilized[1].

In the same vein, the history of wooden boats in the domain of marine engineering is a subject of considerable interest, particularly with regard to the structural design of such vessels, the material properties of the wood utilized in their construction, and their environmental impact. Several other materials have been introduced that are replacing wood in boat and ship construction, especially since the development of composites and fibre-reinforced plastic (FRP), as well as lightweight metals[2].

However, the increasing demand for sustainable transport solutions has driven interest in alternative materials with lower environmental impact. Subsequently, wood has emerged as a compelling option due to its renewability, carbon sequestration ability, and favourable mechanical properties[3].

The transportation sector continues to be a major contributor to greenhouse gas emissions within the European Union, accounting for 31% of energy-related emissions in 2022 [4]. Unlike other sectors, which have seen a decrease in emissions since 1990, transport emissions have increased by 25.9% between 1990 and 2022. This increase is primarily due to growth in road and air traffic [5] as shown in Figure 1. According to data from the Haut Conseil pour le Climat [6], national emissions in France have decreased by 31% since 1990. However, the transport sector has not followed a similar trend. This situation requires an urgent and comprehensive response. Alongside the development of clean energy solutions, the materials used in mobility products must be prioritised. Using eco-friendly materials such as wood, bamboo and natural fibre composites presents a sustainable alternative with reduced embodied carbon.

Incorporating these materials into bicycles, boats, and other low-impact transportation systems is essential for reducing life cycle emissions and aligning with EU climate objectives.

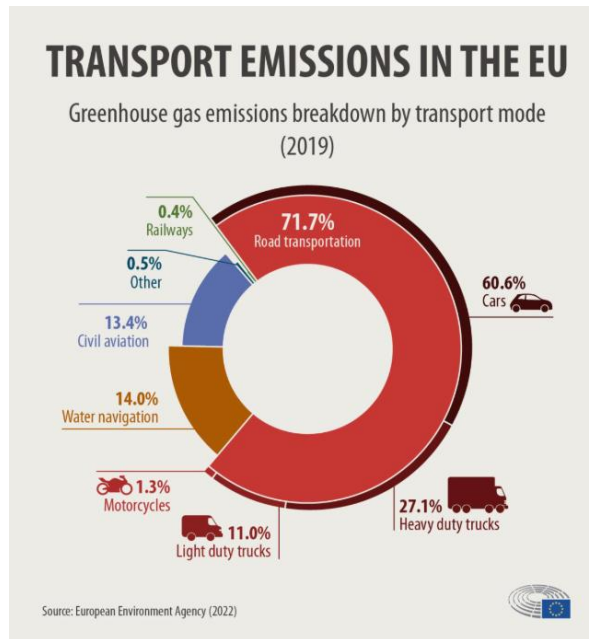


FIGURE 1.1: GREENHOUSE GAS EMISSIONS FROM TRANSPORT IN THE EU BY TRANSPORT MODE (2019). SOURCE: EUROPEAN ENVIRONMENT AGENCY, 2022[7].

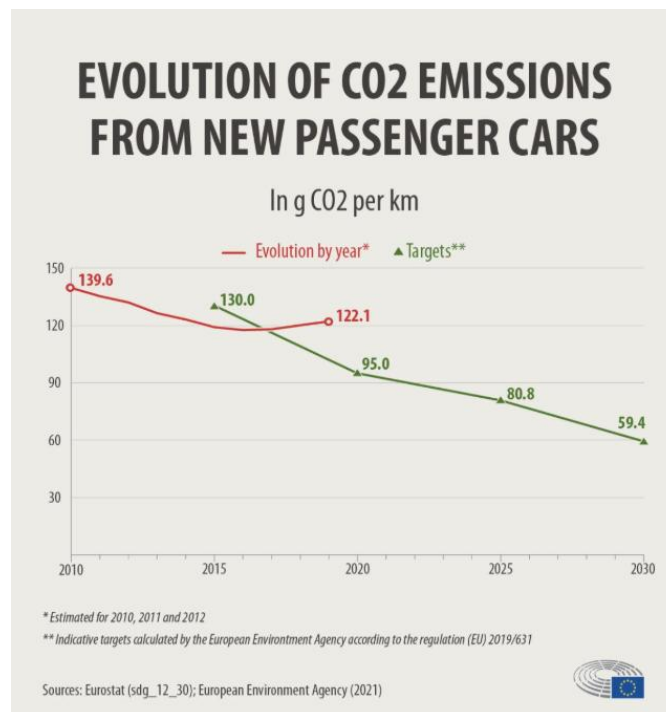


FIGURE 1.2: EVOLUTION OF CO₂ EMISSIONS FROM NEW PASSENGER CARS IN THE EU (2010–2030). SOURCE: EUROSTAT AND EUROPEAN ENVIRONMENT AGENCY, 2021[7].

Unlike conventional materials such as steel and aluminium, wood requires less energy to process, reducing overall carbon emissions. Furthermore, sustainable forestry practices guarantee a consistent wood supply, particularly in regions such as Europe and North America, where forest growth surpasses harvesting rates[3].

Given these advantages, wood is gaining recognition as a viable material for eco-friendly transportation structures, including bicycle frames and marine vessels. Despite the prevalence of conventional materials such as fiberglass, aluminium, and steel within these industries, wood boasts a distinctive amalgamation of mechanical strength, lightweight properties, and sustainability, rendering it a compelling substitute[3].

1.2. Motivation

The global push to reduce greenhouse gas emissions, particularly those from the transportation sector, has sparked interest in sustainable mobility solutions. Although efforts often focus on electrification and changing transportation modes, the environmental impact of construction materials is equally important. Wood is a compelling alternative because it is renewable, biodegradable, and has a high strength-to-weight ratio and aesthetic qualities. Despite its potential, wood's use in modern transport structures, such as bicycle frames and marine sandwich boats, has received limited experimental validation and numerical modelling. Most existing studies address only conceptual or small-scale material analyses, leaving a gap in full-scale structural assessment. This study fills that gap by conducting realistic testing and simulations, which support the broader integration of sustainable materials in vehicle and vessel design.

1.3. Research aim and objectives

This study aims to investigate the structural behaviour of wood in transport systems by combining experimental testing with finite element modelling. Two case studies are investigated:

- A full-scale oak bicycle frame with embedded E-glass fibre reinforcement is assessed for stiffness, strength and failure modes under static loading. Including the design of a

custom test rig to replicate real-world loading conditions, thereby enhancing the correlation between simulations and physical outcomes.

- Sandwich specimens inspired by IMOCA racing boats are composed of a rigid plywood core and synthetic fibre face-sheets. They are tested for flexural performance and damage mechanisms. Finite element models will simulate the mechanical response of the structures, guide design optimisation and be validated against the experimental results.

1.3.1. Scope of the Study

This study focuses on the structural use of wood in two specific contexts within the transport sector: bicycle frames for city and trekking bikes, and marine sandwich structures modelled on IMOCA boats. The investigation is limited to static loading conditions and does not cover dynamic fatigue or environmental degradation. Only existing frame geometries provided by manufacturers are considered, although opportunities for optimisation are explored. The sandwich specimens are examined at component level rather than full-vessel scale. Material properties, structural behaviour and design feasibility are evaluated through laboratory testing and simulation.

1.3.2. Significance of the Study

This research advances sustainable engineering by offering practical insights into using wood as the main structural material in transport. Through rigorous testing and simulation, the study validates the mechanical performance of wooden bicycle frames and composite sandwich structures, proposing viable alternatives to traditional materials such as aluminium and steel. These findings could inform design practices in the industry and be extended to other applications, such as marine structures and lightweight vehicle components, thereby promoting innovation in environmentally responsible transportation solutions.

1.4. Structure of the dissertation

This thesis is organized into five chapters, each addressing a critical component of the research:

Chapter 1: Introduction

This chapter introduces the background and context of the study, highlighting the motivation for exploring wood as a sustainable material for transportation applications. It presents the research aim, specific objectives, and the identified research gap, laying the foundation for the subsequent chapters.

Chapter 2: Literature Review

This chapter provides a comprehensive review of existing research on wooden structures, with particular emphasis on sandwich structures and their mechanical behaviours. The chapter discusses the application of wood in bicycle frames and marine vessels, compares it with conventional materials such as steel, aluminium, and composites, and outlines the advantages and limitations of each. It also explores existing failure criteria and modelling techniques used in structural analysis, thereby establishing the theoretical framework for this study.

Chapter 3: Methodology

This chapter describes the research methodology employed to achieve the study objectives. It details the experimental procedures for static testing of a wooden bicycle frame and material testing of IMOCA-inspired sandwich specimens. Additionally, it outlines the finite element modelling (FEM) approach used to simulate mechanical behaviour, assess stress distribution, and evaluate structural performance under realistic loading conditions. Custom test rigs and laboratory setups developed for the tests are also presented.

Chapter 4: Results and Discussion

This chapter presents and analyses the experimental and numerical results obtained during the study. It includes detailed evaluations of the mechanical properties, stiffness, failure modes, and comparison between FEM simulations and experimental findings. The chapter discusses the implications of the results in the context of sustainable design and performance of transport structures.

Chapter 5: Conclusion and Recommendations

The final chapter summarizes the key outcomes of the research, highlighting the major findings in relation to the research objectives. It also provides recommendations for future work, identifying areas where further investigation could enhance the understanding and application of wood in sustainable transportation engineering.

THIS PAGE WAS INTENTIONALLY LEFT BLANK

2. LITERATURE REVIEW

2.1. OVERVIEW OF THE MECHANICAL BEHAVIOUR OF OAK WOOD

Different study has sought to understand the unique properties of different species of wood so as to understand its structural application among these studies is that published by Kretschmann [8], where mechanical tests were performed on different species including Oak, which is the main focus. It was stated that the mechanical properties presented were obtained from tests of pieces of wood termed as “clear” and “straight grained” because they did not contain characteristics such as knots, cross grain, checks, and splits.

It was added that the properties represent the average properties of each species were uncertain due the variability of a natural composite like wood which is subjected to constant changing influences such as moisture, soil conditions defects among many others. This shows the unique orthotropic nature of wood. Like every other wood, Oak wood being an orthotropic material is known for its orthotropic mechanical, meaning it possesses unique and independent mechanical properties in three mutually perpendicular directions: longitudinal (parallel to the grain), radial (normal to growth rings), and tangential (perpendicular to the grain, tangent to growth rings) [8]. The sign convention presented in the aforementioned book which is as shown in Figure 2.1 will be adopted in this thesis.

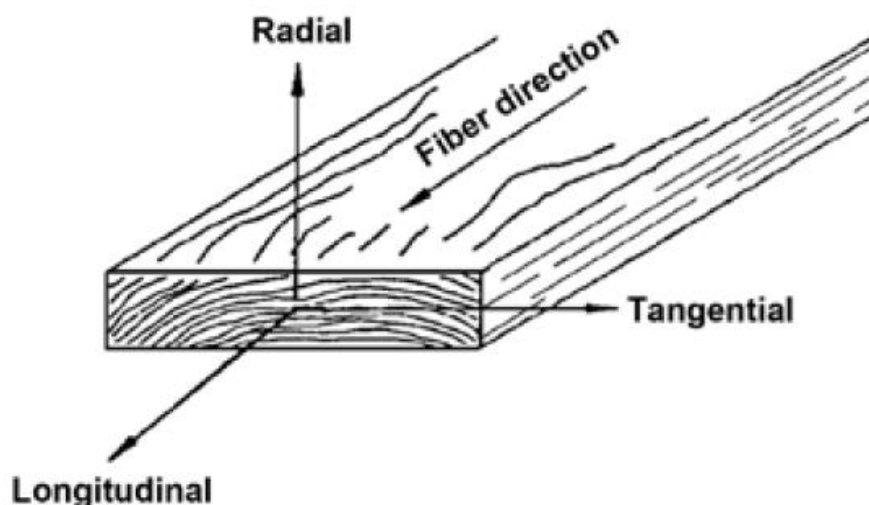


FIGURE 2.1: THREE PRINCIPAL AXES OF WOOD WITH RESPECT TO GRAIN DIRECTION AND GROWTH RINGS[8]

Munoz et al. . [9], added that this distinct directional dependence of mechanical properties originates from the wood's micro-structure. Also, in the study pointed that Oak wood were primarily chosen for furniture other decorative applications because of its attractive appearance, resistance to wear and other characteristics, strength calculations are required for its utilization in wood structures while quoting from the book by Mettem and Richens. But not much was said by source gotten on the use of Oak for structural application like bicycle.

To ascertain the mechanical properties of Oak [9], 42 Oaks samples from several areas of Galicia (NW Spain) were and the specimens were conditioned in the laboratory environment in order to achieve similar equilibrium moisture contents (EMC: 12% according to EN standard 408:2004, European Committee for Standardization 2004b). different standard tests were applied such as the hardness test (UNE standard 56534:1977 , AENOR 1977c), which quantifies the Moninn hardness on the radial face, applying a load of 200 kg during 5 s; uniaxial compression strength (UNE standard 56535:1977 , AENOR 1977d), and static bending strength parallel to grain (UNE standard 56537:1979 , AENOR 1979). The test specimen was arranged in a supported simply and loaded symmetrically at one point over a span of 240 mm. The piece was tested with the growth rings parallel to the direction of loading, i.e., loaded on the radial face. The bending strength was given by the equation for isotropic materials

with rectangular cross-section as shown in equation below.

$$S = \frac{3PL}{2th^2} \quad (2.1)$$

where S is the failure stress in axial bending at the wood moisture content at time of test, P is the maximum load registered, considered as the failure load, L is the span between supports, t is the thickness of the test piece and h is the depth.

While the The apparent MOE in bending was calculated by means of the increment in uniaxial load on the linear portion of the plots “load vs. deformation” using the equation.

$$MOE = \frac{\Delta PL^3}{4\Delta ft h^3} \quad (2.2)$$

Where:

MOE = modulus of elasticity in bending at the moisture content,

ΔP is the increment of load on the linear portion of the “load vs. deformation curve”,

Δf is the increment of deformation corresponding to ΔP and;

L, t, h was defined for equation 2.1.

The finding showed that the modulus of elasticity values were clearly lower than the reference values reported by Wagenfuhr (2007), and were lower than the lowest reference values for small clear oak specimens (Gonet 1971). In addition to the mechanical property correlations reported, where strong positive relationships were found between density, modulus of elasticity (MOE), and bending strength, the work by Díaz-Maroto et al. (2019) offers a complementary anatomical perspective. While the former focused on structural performance under mechanical loads, the latter emphasized wood porosity and void ratio as physical indicators of oak quality—primarily in the context of wine barrel manufacturing.

Interestingly, Díaz-Maroto et al. observed that *Quercus robur* L. exhibited the lowest porosity among the oak species tested, which implies a denser cellular structure. This aligns with the findings in the mechanical study, where higher density was positively correlated with greater stiffness and strength. The lower void ratio found in *Quercus robur* also supports its suitability for applications requiring dimensional stability and limited fluid transmission, such as in liquid storage barrels or structural members exposed to fluctuating humidity.

However, while both studies agree on the advantageous structural characteristics of *Quercus robur* L., the focus of analysis differs: the mechanical study emphasizes strength and stiffness relationships, while the porosity study highlights the anatomical basis for those mechanical advantages. Notably, Díaz-Maroto et al. did not measure strength or MOE directly but provided valuable supporting evidence by correlating anatomical structure (e.g., fewer vessels and lower porosity) with assumed mechanical stability [9].

Different research shows that while natural wood can pose many uncertainties in mechanical behaviour but it can also be predictive to a large degree when properly studied like the LVL which is more like a plywood. Oriented at 0 degree and 90 degree offers the unique mechanical behaviours required for possible load application direction including out of plane forces.

2.2. Failure mode of wooden material

If wood is to be used in structural applications, it is essential to understand its behaviour and, more importantly, its failure mechanisms. Various mechanical tests are conducted to gain this understanding. As a natural composite with pronounced orthotropic and anisotropic properties, wood presents unique challenges when it comes to evaluating its mechanical behaviour. This evaluation is crucial for ensuring the safe and reliable use of wood in construction. To understand and predict how wood behaves under different loads, researchers employ various tests and develop specific failure criteria.

The fundamental mechanical properties of wood, especially those that govern its structural performance, are most often evaluated using static bending tests. These tests provide essential insights into the material's stiffness and strength under flexural loading. According to the ČSN 490115 standard, static bending procedures determine the ultimate static end load at which the wood specimen undergoes permanent deformation or failure[10].

Specimens used in this test are typically prismatic in shape. They usually have a cross-section measuring 20.00 mm × 20.00 mm. They also measure 300.00 mm in length. The specimens are supported at both ends. A central point load is then applied to the midpoint of the specimen's span, inducing bending stress as shown in Figure 2.2. Some variations use a third-point loading configuration to distribute the applied force more uniformly, especially when characterizing larger samples or engineered wood products [10].

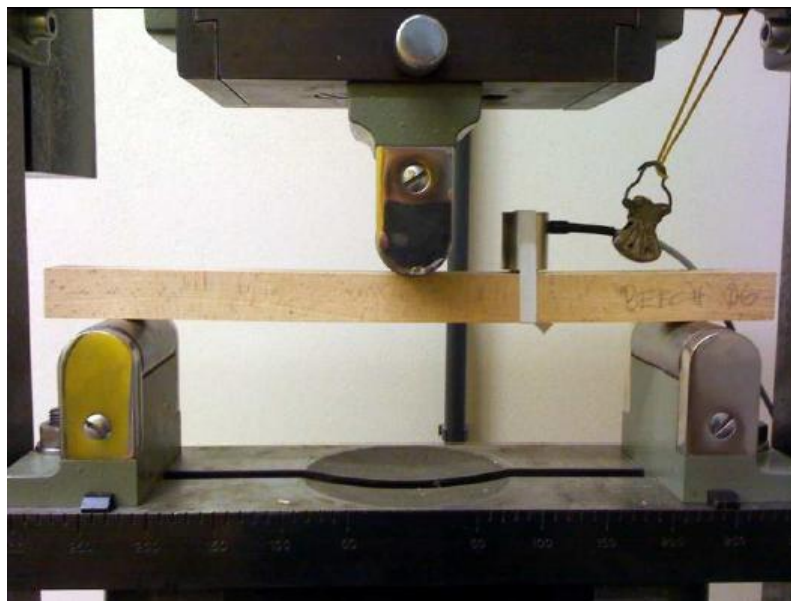


FIGURE 2.2: STATIC BENDING TEST SPECIMEN WITH ACOUSTIC EMISSION SENSOR ATTACHED[10]

Two of the most critical parameters obtained from static bending tests are the modulus of elasticity (MOE) and the modulus of rupture (MOR). MOE is a measure of a material's stiffness, defined as its resistance to elastic deformation when an external force is applied. This property is essential for predicting deflection behaviour in structural members. MOE values are sensitive to environmental conditions. These conditions include temperature and moisture content. This has been widely observed. Specifically, wood-based panels and solid woods exhibit a reduction in MOE at elevated temperatures due to softening of the lignin matrix and increased molecular mobility in the cellulose microstructure [10], [11]. Conversely, MOE values generally increase at lower temperatures due to the stiffening effect caused by ice crystal formation and tighter hydrogen bonding among cellulose fibrils. The Modulus of Rupture (MOR) is a measure of a wood specimen's maximum load. It represents the load before the specimen fails in bending. This ultimate strength parameter is crucial in structural design, especially for applications involving flexural stresses. During static bending tests, the moment of rupture is often marked by a significant increase in acoustic emission (AE) activity, corresponding to internal cracking, fibre breakage, and other failure mechanisms typical of orthotropic, fibrous materials like wood. AE monitoring is widely recognized as an effective, non-destructive method for tracking damage evolution and predicting failure in wooden specimens under flexural loading [10]. Similar to the modulus of elasticity (MOE), the MOR is influenced by environmental factors, such as temperature and moisture content. Studies have shown that, at elevated temperatures, the MOR decreases due to thermal softening of the lignin matrix and weakened microfibril cohesion within the cell walls [12].

In addition to MOE and MOR, significant parameters derived from static bending and related mechanical tests include time to specimen failure (TSF), maximum loading force ($F_{(max)}$), and wood density. These values provide a more comprehensive understanding of how wood responds mechanically under loading conditions [10].

Beyond flexural tests, a range of other mechanical tests are employed to further characterise wood performance. The compression strength of wood, both parallel and perpendicular to the grain, is crucial in evaluating its load-bearing capacity. Recent studies have shown that red and white oak in particular have compression strengths that exceed previously reported values, especially perpendicular to the grain. Janka hardness testing measures resistance to indentation, and oak species generally align with or slightly surpass historical benchmarks. Determining longitudinal shear modulus is something that can be achieved by using torsion testing, a method that involves the introduction of pure shear stress. This is an important feature, but one that is

not always possible with traditional shear tests. Similarly, tensile tests characterise elastic behaviour and identify shear strains, particularly in notched or 'dog-bone'-shaped specimens that focus deformation in a specific region[9].

Additionally, moisture content (MC) is a critical factor in all mechanical testing of wood because it significantly affects strength, stiffness and failure behaviour. Higher moisture levels typically reduce mechanical performance, so conditioning and environmental control are essential for comparative testing. [3].

Numerous studies, including those focused on solid wood species and engineered composites, have provided empirical findings that support these observations. For example, static bending tests that incorporated acoustic emission (AE) monitoring revealed that the final failure stage is characterized by distinct AE bursts. This validates the modulus of rupture (MOR) as a reliable indicator of structural failure [13]. These findings reinforce the importance of static bending in mechanical characterization and highlight the value of integrating non-destructive evaluation techniques to understand wood's complex behaviours under load.

Accurately characterizing deformation and failure mechanisms in wood is critical for reliably using it in structural and transport applications. Although conventional mechanical testing reveals essential material properties, advanced techniques such as acoustic emission (AE) and digital image correlation (DIC) provide deeper insight into damage evolution, internal stress redistribution, and progressive failure behaviours of wood under various loading conditions [13].

AE is a non-destructive testing technique that detects transient elastic waves generated by the sudden release of energy from localized sources within a stressed material. These acoustic signals result from internal events, such as microcrack initiation, fibre rupture, interfacial debonding, and cell wall collapse. AE monitoring is particularly valuable in wood during static bending tests because it enables real-time observation of the damage process. AE activity tends to accumulate significantly as the specimen approaches failure, and AE event intensity is often correlated with critical structural transitions, such as crack propagation or loss of stiffness. As noted in studies,[10], The utility of AE in identifying the different stages of failure in static bending tests on wood specimens was demonstrated. This research highlights the effectiveness of AE in capturing early damage signals non-destructively, before macroscopic failure becomes evident. These findings are particularly relevant when evaluating natural composites such as wood, which exhibit anisotropic mechanical behaviours and a variety of internal failure mechanisms due to their cellular structure.

Different wood species exhibit distinct acoustic emission (AE) response patterns under similar mechanical loading conditions. For instance, oak trees often generate powerful AE signals before they actually fail, which indicates that the main cause of the failure is tensile forces. In contrast, spruce and other softwoods tend to exhibit more gradual AE activity, characterised by numerous smaller events preceding final failure. These differences emphasise the variability in fibre orientation, density and moisture content among species, all of which significantly impact the mechanical response. [10], [12]. AE data are thus instrumental in revealing failure progression in wood, calibrating predictive failure models, and monitoring the structural integrity of wooden components in real-world applications.

AE is complemented by digital image correlation (DIC), which is a critical full-field optical technique for mapping surface deformation in anisotropic materials, such as wood. DIC, which involves capturing a series of digital images of a specimen's surface before and during mechanical loading, is a method of analysis. This enables a speckle pattern to be tracked in order to compute displacement and strain fields. This non-contact technique provides high-resolution insights into the heterogeneous deformation behaviour of wood, which is useful given the material's natural imperfections, including knots, grain deviation and transitions between earlywood and latewood [14].

In compression tests, digital image correlation (DIC) enables the detection of non-uniform strain distributions and the identification of premature buckling or localized collapse zones, particularly in the end regions of test specimens. In flexural testing, DIC facilitates the precise identification of the neutral axis and the detailed visualization of strain gradients across the depth of the beam. These observations are vital to understanding how and where failure initiates and propagates. DIC is also effective for determining the longitudinal shear moduli of both clear wood and wood-based composites, as it accurately captures full-field shear strains under torsional loading conditions. Similarly, under tensile loading, particularly in notched, dog-bone-shaped specimens. DIC has proven effective in quantifying axial and shear strains. This supports the validation of numerical models and the assessment of failure mechanisms[14].

Furthermore, DIC has been extensively used to characterize sandwich composites with wood cores and composite face-sheets. This technique provides critical information on strain localization, face-core interface behaviour, and debonding under combined flexural and shear loading scenarios. DIC also enables the extraction of material constants, such as Poisson's ratios, and facilitates a more accurate evaluation of anisotropic elastic behaviour. The study

demonstrate shows the reliability and precision of DIC in capturing elastic deformation and damage evolution in engineered wood structures [14].

The resolution and reliability of structural behaviour assessments are significantly enhanced by the integration of AE and DIC into experimental wood mechanics.

2.3. FEM Failure Criteria mode study of Wood

Traditional phenomenological failure models, such as the quadratic, Tsai-Hill, and von Mises criteria, often fail to distinguish between the tensile and compressive domains. This leads to inaccuracies when simulating real-world wooden structures. As pointed out in Blanco et al. (2015), there is an increasing demand for design-oriented models that more accurately reflect the natural mechanical anisotropy and damage mechanisms in wood.

Phenomenological models have typically treated wood in a simplified manner. They have assumed isotropic or basic orthotropic behaviour. For example, researchers widely adopt the Tsai-Wu criterion as a quadratic failure surface model. This model incorporates tensile and compressive strengths along with an interaction coefficient. While suitable for composite materials, it is inadequate for modelling the nonlinear and asymmetric tensile-compressive response of wood. The difficulty of accurately determining the interaction term, combined with the model's underlying assumption of a unified failure surface, reduces its effectiveness for orthotropic natural materials like wood [15].

Similarly, the von Mises and Norris failure criteria assume a symmetrical material response in tension and compression. However, this conflicts with the observed anisotropic and direction-dependent failure behaviour of wood. Specifically, these models do not account for the fundamental differences between the tensile rupture of wood fibres, which is brittle, and their compressive deformation, which is ductile. Under compressive stress, wood often fails through mechanisms such as buckling, crushing and kinking, involving progressive deformation and localised instability. In contrast, tensile failure in wood typically occurs abruptly as a result of fibre rupture, reflecting a more brittle failure mode [10]. As Eberhardsteiner emphasised, accurate constitutive modelling of wood must incorporate its multi-phase nature and distinguish between its tension–compression asymmetry in order to reliably simulate failure responses [14].

To address these challenges, Blanco et al. [15] proposed a novel ellipsoid-cylinder failure model that distinctly separates the tensile and compressive domains. This model is geometrically defined by an ellipsoid for the compressive region and a cylinder truncated by a plane for the

tensile domain. The model accurately captures the brittle fracture limit in longitudinal tension while accounting for interaction effects in compression, such as those arising from combined lateral and shear stress. Unlike phenomenological criteria, which require complex parameter identification, this model depends only on uniaxial strengths: longitudinal and transverse tension (X_t, Y_t), compression (X_c, Y_c), and shear (S). The reduction in required parameters makes the model particularly advantageous for early-stage structural design and implementation into finite element analysis workflows.

In assessing wood failure under complex stress states, Blanco’s comparative study of failure models showed that the ellipsoid-cylinder model was more effective than traditional criteria such as Tsai-Wu, von Mises and van der Put. When evaluated using characteristic strength values for blind predictions as shown in Table 1, the ellipsoid-cylinder model yielded the lowest total normalised sum of squared errors, compared to others considered. The superior performance of the ellipsoid-cylinder model was particularly evident in regions of biaxial stress involving a combination of tension and compression, where classical criteria struggled to accurately decouple these effects. Further validation using the best-fit method confirmed the robustness of the ellipsoid-cylinder model, which achieved an even lower SS value of 19.27 [15].

TABLE 1: COMPARISM OF FAILURE CRITERIA MODEL AND THE STANDARD ERROR[15]

Model	Sum of Squared errors (SS)
ellipsoid-cylinder	33.63
Tsai-Wu	53.00
von Mises	57.00
van der Put	53.80

When examining interaction effects, the ellipsoid-cylinder model aligns with findings from recent multiscale simulation studies that emphasize the importance of compressive-shear coupling in wood-like materials. For instance, Hartmann and Puch, demonstrated that the deformation behaviour of softwood tracheids under compressive loading is highly direction-dependent, with significant mechanical differences observed between earlywood and latewood. These differences result in localized deformation patterns, including shear collapse and cell wall buckling, particularly under combined loading conditions. In contrast, tensile rupture along the grain remains relatively isolated from lateral stresses, justifying its separate treatment in predictive modelling. These conclusions support the use of failure criteria that distinguish

between tensile and compressive envelopes, especially in anisotropic materials like wood–polymer composites [16].

Although the Tsai-Wu criterion is generally preferred in composite analysis due to its flexibility, the interaction term can produce unrealistic failure surfaces in wood, especially when the compressive and tensile domains behave disproportionately. The von Mises model is mathematically simple but assumes equal tensile and compressive yield strengths, so it performs poorly under the anisotropic stress states typical of wood applications.

Another established failure criterion is the van der Put model, which introduces a general tensor polynomial formulation that omits the interaction coefficient. While it performs reasonably well, especially in plane stress states, it does not provide the same clarity in distinguishing independent tensile failure mechanisms. The ellipsoid-cylinder model's ability to segment these domains geometrically and accurately represent failure progression makes it a favourable design tool[15].

From a sustainable design perspective, by Castanié et al., [3]. advocates, incorporating robust failure models is essential to validating the use of wood as an alternative to synthetic composites and metals in transportation. These applications involve complex stress environments, such as bending, torsion, and impact, where model precision can directly influence material selection and safety margins. Predictive models, such as the ellipsoid-cylinder criterion, improve simulation accuracy and support the regulatory validation and performance certification of wood-based structural components.

2.4. Bicycle Frame: Materials, Loading, stiffness and test setup

Bicycle frames as shown in Figure 2.3 are fundamental to the overall performance and integrity of a bicycle. Their design, material composition, and structural configuration dictate their stability, stiffness, weight, and ride comfort. The materials and load-bearing capacity of bicycle frames must be optimized to meet performance requirements while remaining durable under dynamic loads.

2.4.1. Evolution and Selection of Frame Materials

Historically, bamboo and wood were two of the first materials used to make bicycle frames. Consisting of cellulose fibres embedded in a lignin matrix, bamboo is a natural composite

material that is lightweight and has a high tensile strength of up to 350 MPa. It also provides good vibration damping and is sustainable [17]. However, it is difficult to connect and structurally optimise due to its hollow nature and thin walls. Although the tensile strength of bamboo and aluminium can be similar, studies show that bamboo has a favourable strength-to-weight ratio due to its significantly lower density (0.4 g/cm^3 vs. 2.7 g/cm^3) [17].

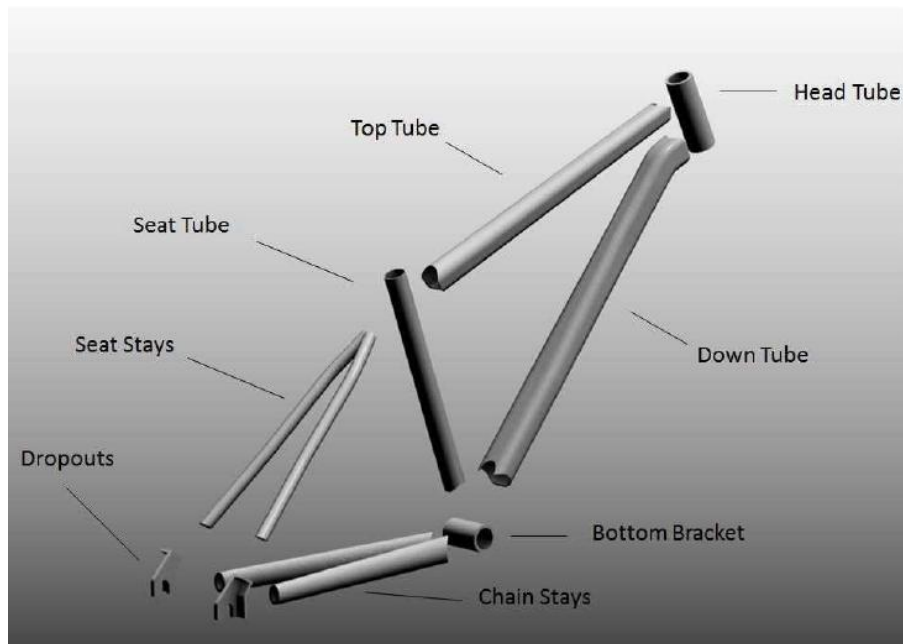


FIGURE 2.3:TYPICAL BICYCLE FRAMES PART LABEL [1]

Modern bicycle frames are predominantly made from metal and composite materials. Steel is renowned for its toughness and fatigue strength, with certain alloys offering tensile strengths of up to 1350 MPa. Aluminium alloys such as 6061-T6 and 7005-T6 are widely used due to their light weight and corrosion resistance, but they lack a fatigue limit and therefore require safety factors in the design process [18]. Although expensive, titanium combines light weight, shock absorption and corrosion resistance, making it ideal for high-end frames. Meanwhile, carbon fibre is the material of choice for performance frames thanks to its high stiffness-to-weight ratio, although it remains brittle and expensive[19].

More recently, sustainable options such as hemp fibre-reinforced composites have emerged. When wound over aluminium cores, these hybrid tubes demonstrate structural adequacy under static loading whilst reducing environmental impact. Finite element simulations have validated their stiffness and stress-handling capacity [20].

2.4.2. *Load Conditions and Structural Demands*

Bicycle frames are subjected to a combination of static and dynamic loads during normal use. These include pedalling-induced cyclic forces, braking-induced impact loads, and body weight distribution during seated riding. For fatigue evaluations, pedal loads typically reach 1100 N and are applied cyclically at 2.5 Hz [21]. Braking can cause in-plane peak stresses of up to 257 MPa in the top and down tubes, and up to 189 MPa in the fork [22]. Vertical loads on the seat tube can exceed 1200 N during seated riding, which contributes to compressive stress and potential buckling. Horizontal fork loads of around 600 N replicate frontal impacts or terrain-induced shocks [21]. Torsional stresses at the bottom bracket simulate twisting during pedalling and are relevant for lateral stiffness assessments [22].

Standardised testing protocols such as ISO 4210 and ASTM F2711 incorporate these loading conditions to evaluate frame durability and rider safety [23].

2.4.3. *Stiffness Evaluation, Frame Performance and Test Rig Design*

Frame stiffness is important for efficient energy transfer and stable handling. Researchers often evaluate it in multiple directions: in-plane (vertical and longitudinal), transverse (lateral) and eccentric (combined load and torque).

Despite the numerous test setups used in research, there is currently no universally accepted standardised test rig design for evaluating bicycle frame stiffness. Consequently, it is challenging to compare results across different studies, since frame support conditions, loading methods and sensor placements can vary significantly. Similarly, stiffness assessment protocols differ in terms of loading points, directions and measurement systems, contributing to variability in reported stiffness values[24].

In the study by[25], [26], both introduced innovative test rigs incorporating load actuators and sensors (e.g. strain gauges and LVDTs) in an attempt to standardise stiffness assessment. These experiments also revealed that bearing types, mounting methods and preload conditions can significantly influence results [24].

Recent test rig developments emphasize multi-directional loading capabilities to replicate real-world conditions. For example, the use of pneumatic or hydraulic actuators allows controlled application of vertical, horizontal, and torsional loads simultaneously, enabling better assessment of combined stress responses. Findings show that vertical stiffness values can

exceed 2000 N/mm in high-performance aluminium frames, while torsional stiffness often varies depending on frame geometry and joint construction [24]. These experiments provide crucial data for calibrating numerical models and validating frame design improvements.

Despite numerous test setups in research, there is currently no universally accepted standardized test rig design for bicycle frame stiffness evaluation. As a result, comparing results across different studies is challenging, since frame support conditions, loading methods, and sensor placements vary significantly. Similarly, stiffness assessment protocols differ in terms of loading points, directions, and measurement systems, which contributes to variability in reported stiffness values[24].

2.4.4. Numerical and Experimental Correlation

Finite element analysis (FEA) has become an essential tool for designing bicycle frames. Simulations enable engineers to evaluate stress concentration zones, stiffness and potential failure modes under complex loading conditions [27][15]. Key modelling considerations include mesh density at weld joints, accurate geometry and heat-affected zones (HAZs) in aluminium or steel frames. FEA results are typically validated using experimental methods such as digital image correlation (DIC), acoustic emission sensors and strain gauges [21].

DIC provides non-contact, full-field strain measurements and is particularly useful for detecting strain localisation near joints. Embedded fibre Bragg grating (FBG) sensors within composite frames also facilitate internal stress monitoring. Simulated and measured responses tend to align closely when test fixture constraints and loading profiles are accurately replicated [27].

2.5. Sandwich Panel Design and Marine Applications

Sandwich structures are well-known in engineering because of their excellent stiffness-to-weight and strength-to-weight ratios. This makes them a good choice in industries where it is important to reduce weight without reducing mechanical performance [28], [29]. Structurally, they consist of two strong, thin outer faces, often referred to as 'face-sheets', bonded to a comparatively thick, lightweight core. This arrangement functions much like an I-beam: the face-sheets carry most of the in-plane tensile and compressive stresses induced by bending, while the core maintains separation between the face-sheets, resists transverse shear forces and stabilises the faces against local buckling. Separating the load-bearing faces increases the

section modulus, enabling high bending rigidity without a proportional increase in weight. In addition to their structural role, cores can contribute to energy absorption, vibration damping and, in some cases, thermal or acoustic insulation. This has further extended the use of sandwich configurations in multifunctional applications. [28], [29].

The performance of a sandwich panel is intrinsically linked to the properties of its core and face-sheets. Core materials have evolved to meet the diverse requirements of specific industries. Foams such as PVC, PMI and polyurethane offer closed- or open-cell structures that combine low density with reasonable shear properties and ease of shaping. This makes them common in marine and wind turbine components [28], [29]. Honeycomb cores, which are manufactured from aluminium, Nomex®, or thermoplastics, provide exceptional stiffness and strength, which is why they are used so extensively in the aerospace industry. Natural cores, such as end-grain balsa wood, offer high compressive and shear strength, particularly in grain-aligned directions. They have long been favoured in boatbuilding due to their combination of performance and sustainability. However, anisotropy and moisture sensitivity require careful consideration [28], [29]. Various configurations of cores are as shown in Figure 2.4

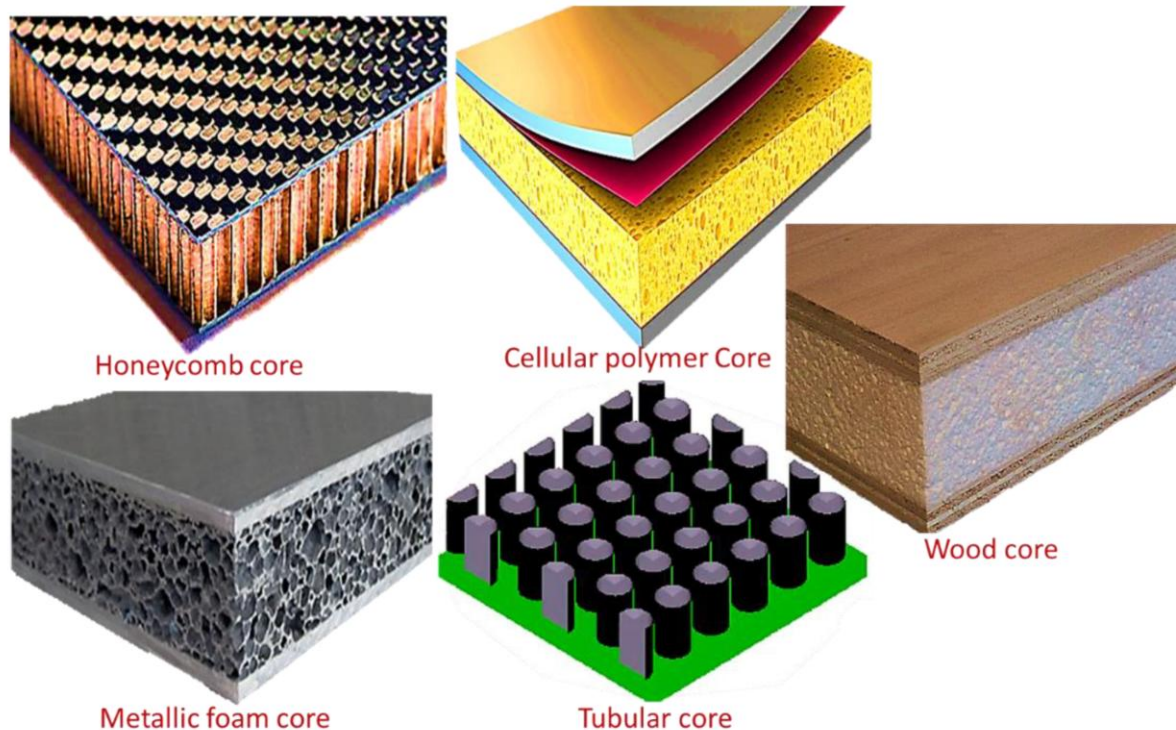


FIGURE 2.4: DIFFERENT CORE STRUCTURES IN SANDWICH COMPOSITES[28]

Similarly, the choice of face-sheet material affects how effectively the sandwich can utilise the mechanical leverage offered by the core. Metallic face-sheets, commonly made of aluminium, titanium or steel, provide durability, toughness and impact resistance, all of which are highly valued in aerospace, transport and architectural applications. Fibre-reinforced polymer (FRP) face-sheets, which are based on glass, carbon, or aramid fibres in thermoset or thermoplastic matrices, offer high specific strength and corrosion resistance. They also allow mechanical properties to be tailored through laminate design and have become prevalent in marine and aerospace structures [28], [29].

In recent years, wood-based cores, particularly plywood and laminated veneer lumber (LVL), have attracted renewed attention in the design of marine sandwich structures. The cross-laminated structure of plywood provides higher in-plane isotropy than solid timber, coupled with high shear strength and excellent fastener retention. Modern fabrication techniques such as vacuum-assisted resin infusion (VARI) combined with resin-rich sealing layers address the traditional concerns of biological degradation and water ingress. Due to its consistent quality and predictable mechanical properties, LVL demonstrates superior fatigue shear performance under cyclic loading, making it particularly well-suited to high-cycle stress scenarios, such as slamming in high-speed craft [30].

2.5.1. Plywood based core Sandwich Panel Mechanical Performance

The manufacturing of laminated veneer lumber (LVL) and plywood allows for the selection of veneers that are free from visible defects. This results in static mechanical characteristics that are comparable to, and sometimes even better than, those of solid wood [31], [32]. With this engineered lay-up, these products can be tailored to specific structural requirements, making them ideal for lightweight yet high-performance applications in transport and marine structures.

In the study by Susainathan et al., [30], it was demonstrated that plywood-core/glass-epoxy panels fabricated via VARI (Vacuum-Assisted Resin Infusion) achieved bending stiffness values exceeding $35 \text{ kN}\cdot\text{mm}^2$ and displayed progressive failure modes under four-point bending. In Experimental investigation of compression and compression after impact of wood-based sandwich structures, it was found out that panels retained over 80% of their undamaged compressive capacity after low-velocity impact, with dominant failure modes including core rolling-shear failure, face-sheet wrinkling, and face-sheet-core debonding. Digital Image Correlation (DIC) which has been extensively discussed under the oak wood section was also

used in the study to provide full-field strain maps to track initiation and propagation of these failures.

The flexural performance of wood-based sandwich structures incorporating plywood or LVL cores has been widely investigated. Xie et al. in their study [29] developed composite sandwich panels with paulownia wood cores and glass fibre-reinforced polymer (GFRP) face-sheets. These were evaluated through four-point bending tests in accordance with established flexural testing standards, such as ASTM D6272 and ASTM D790 [18]. Their results demonstrated good structural integrity under transverse loading and the presence of a large plateau region in the load–displacement response after initial failure. This behaviour is beneficial in preventing catastrophic collapse and was attributed to compressive yielding of the upper face-sheet as the dominant failure mode. Paulownia cores with a thickness of 120 mm achieved peak loads of 217.0 kN, representing a 36% higher ultimate load than specimens with a thickness of 80 mm, while also exhibiting significant energy absorption (14.6 kJ). Compared to poplar, paulownia offered a favourable balance between load-carrying capacity and reduced weight, highlighting the importance of selecting the appropriate core density for optimising stiffness-to-weight.

2.5.2. Wood Based Sandwich structure in Marine Application

Sandwich structures are widely used in the marine industry mainly due to their high strength-to-weight ratio, corrosion resistance and ability to meet strict performance requirements in challenging conditions [28], [33]. The adoption of sandwich structures in naval architecture is driven by the need to create lightweight designs without compromising structural integrity — a critical balance for high-performance vessels [30], [34].

Modern racing yachts and other fast marine craft often use honeycomb core sandwich panels for components such as decks and sails, where enhanced stiffness and reduced weight are crucial for speed and handling [33]. Similarly, balsa wood core sandwich structures have been widely adopted in marine and civil engineering applications due to their cost-effectiveness, renewable sourcing and high thermal insulation capacity [28]. These properties make balsa cores an attractive option for large-area structural elements that are exposed to variable environmental conditions.

Manufacturing methods for marine sandwich structures vary according to performance requirements and production scale. The pultrusion process, for instance, has been effectively utilised in the production of civil and marine sandwich composites, providing high throughput

and consistency in the fabrication of long, prismatic elements [28]. Recently, innovative core–face-sheet configurations have broadened the scope of wood-based sandwich applications. Xie et al. [29] demonstrated the use of paulownia wood cores with glass fibre-reinforced polymer (GFRP) face face-sheets and lattice webs to produce composite sandwich matting that can be rapidly deployed for military engineering, emergency rescue and large-scale infrastructure projects in challenging environments, such as soft clay subgrades. This resilience to challenging service conditions makes it well suited to the operational requirements of marine transport and offshore support structures.

Based on past research papers and the findings as at the time of this study, it can be seen that, within the marine sector, GFRP remains one of the most widely used face-sheet materials due to its favourable balance of mechanical performance, corrosion resistance, low maintenance and cost [30]. Its compatibility with various core materials, including wood and foam, enables designers to customise stiffness, strength, and durability according to specific functional requirements. Together, these developments demonstrate the adaptability and versatility of sandwich composites in marine engineering, and support their ongoing evolution towards lightweight, sustainable, high-performance structural solutions.

2.6. Failure Modes and Testing Relevance

Several characteristic failure modes affect sandwich panels, including those with plywood cores. The most common of these are face-sheet yielding, core shear and face-sheet wrinkling [29]. Bending tests on plywood-core sandwich configurations have revealed a sequence of progressive and interacting failure mechanisms. Fibre fracture often begins at the bottom longitudinal ply, where the tensile stresses are greatest, especially in plies oriented parallel to the load direction. Transverse shear failures propagate through adjacent transverse plies, while decohesion may occur within the middle transverse ply or develop as peeling cracks, particularly in panels with bonded face-sheets. Face-sheet–core debonding or delamination is another concern, particularly when adhesion is compromised. Vacuum moulding with carbon composite face-sheets, for example, has been shown to result in weaker face-sheet–core bonds, whereas glass and flax face-sheets fabricated via thermo-compression generally exhibit stronger adhesion, mitigating severe debonding [30]. Crushing of the plywood cell walls, often detected as an extended inelastic plateau in the force–displacement curve, indicates progressive radial compression within the core. Ultimately, reductions in stiffness caused by fibre fracture,

transverse shear or debonding lead to a drop in peak force and typically result in brittle final failure.

Studies of fracture toughness, particularly those focusing on delamination behaviour, have identified additional mechanisms that are relevant to plywood-core sandwich structures. Crack migration occurs when a propagating crack deviates from its initial interface into neighbouring plies; for example, from the interface into the 90° ply in a $[0^\circ/90^\circ]$ configuration. This migration may be driven by out-of-plane fibre deviation, variations between earlywood and latewood regions, or instances where the glue joint is stronger than the surrounding wood [34]. Fibre bridging, whereby intact fibres span across the crack front, has been found to significantly impact the measured fracture toughness, particularly at $[0^\circ/0^\circ]$ interfaces, though its effect is less pronounced at $[0^\circ/90^\circ]$ interfaces. Fracture surfaces often reveal whether failure was adhesive, occurring between the wood and glue, or cohesive, occurring within the wood adjacent to the glue line. Notably, cohesive failure within the glue itself is rare, indicating that the adhesive strength typically exceeds that of the wood substrate [34].

Collectively, these observations underscore that the mechanical performance of plywood-core sandwich structures is governed by a combination of material anisotropy, ply orientation, face-sheet–core interface quality, and manufacturing process parameters. Understanding the interaction between these factors is critical for designing panels with improved resistance to bending-induced damage and delamination under operational loads.

3. METHODOLOGY

3.1. Overview

This study employs an integrated experimental–numerical methodology to evaluate the mechanical performance of wood-based structures in two transport applications:

1. Cycling application – A full-scale solid oak bicycle frame.
2. Marine application – IMOCA-inspired sandwich panels with plywood cores and fibre-reinforced polymer (FRP) face-sheets.

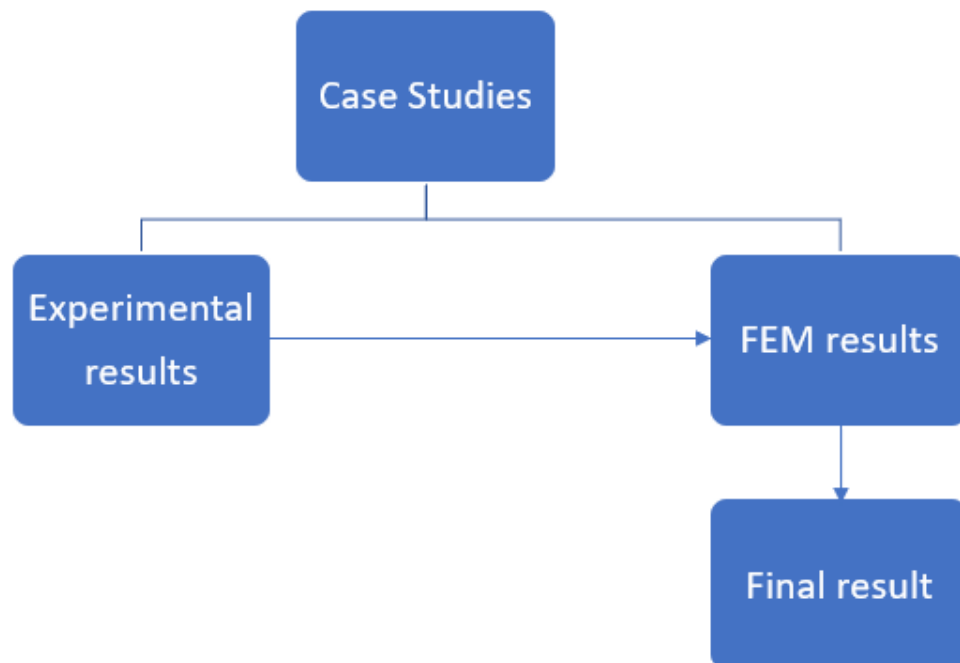


FIGURE 3.1: METHODOLOGY PROCESS FOR BOTH STUDY CASES

Both case studies were tested under representative loading conditions and modelled in Abaqus to simulate structural behaviour, the data gotten from the experimental result were used to validate the FEM model as shown in Figure 3.1. For the bicycle frame, a custom test bench was designed in CATIA V5[35] to enable stiffness testing. The solid oak frame provided by the client was reverse engineered from a 3D scan to create accurate solid geometry in CATIA V5. This geometry was then exported to Abaqus/CAE[36] for finite element modelling. Post-processing in Python was implemented to perform custom failure checks, since direct

application of the Tsai–Wu criterion was not possible with the 3D solid elements used in the model.

For the IMOCA sandwich specimens, the client provided a total of 234 samples for testing. For each set of specimens with the same face-sheet orientation and fibre type, magnified scan images were taken to determine the thickness of each ply in the plywood core and fibre-reinforced face-sheets. These measured thickness values were then used in Abaqus to accurately define the material layups and thickness parameters for the simulation models.

3.2. Case Study 1: Bicycle Frame

3.2.1. Materials and Construction

The bicycle frame was fabricated from solid oak (*Quercus robur*), selected by the client for both its high stiffness, strength, and workability, as well as its aesthetic appeal. Oak's orthotropic mechanical properties is as shown in Table 2 [37], with missing parameters supplemented from the study by Gambarelli et al. [38].

The frame as shown in Figure 3.2 consisted of approximately fifteen individual oak elements, which were joined using Resoltech 8050 epoxy adhesive. This adhesive was selected for its exceptional adhesion to wood, high mechanical strength, and durability in demanding environmental conditions, as detailed in the manufacturer's specifications[39].

The bicycle featured a modified diamond/triangle geometry, with hollow sections designed for the top tube, bottom tube and seat tube. Within these sections, two layers of 0.3mm thick dry E-glass roving fabric, oriented at $[\pm 45^\circ]$, were laid and impregnated with stratified epoxy resin as specified by the client. The E-glass roving specification was obtained from Mack Kayak ('Roving 300 grams')[40], while the detailed mechanical properties of the E-glass fibres were taken from AZOM[41]: 'Properties of E-Glass Fibre'[41] with a value of $E_f = 73,000\text{MPa}$, $G_f = 30,000\text{MPa}$ and $\nu_f = 0.22$. For the purpose of finite element modelling in Abaqus, the epoxy resin in the internal laminate was represented using the mechanical properties of EPON™ 828 epoxy resin[42] with the values of $E_m = 3,250\text{MPa}$, $G_m = 1203.70\text{MPa}$ (using Eq. 3.1-3.5) and $\nu_m = 0.35$, since its datasheet provided the detailed engineering constants required for simulation.

The fibre volume fraction used was set at 55%, and the laminate's homogenised engineering properties, calculated using the rule of mixtures and micromechanics equations, are presented in equation 3.1-3.5 and the mechanical property is as shown in Table 3.

TABLE 2: OAK, RED BLACK WOOD MECHANICAL PROPERTIES[8], [38]

Common species names	Moisture content	Specific gravity^b	Modulus of rupture (kPa)	Modulus of elasticity (MPa)(E₁₁)	ET (0.082* E₁₁)
Oak, red Black	12%	0.61	96,000	11,300	927
	ER (0.154*E₁₁)	GLR (0.089* E₁₁)	GLT (0.081* E₁₁)	GRT	μLR
	1740.2	1005.7	915.3	448.5	0.292
	μLT	μRT	Work to maximum load (kJ m⁻³)	Impact bending (mm)	Compression parallel to grain (kPa)
	0.064	0.033	94	1040	45000
	Tension parallel to grain (kPa)	Compression perpendicular to grain (kPa)	Shear parallel to grain (kPa)	Tension perpendicular to grain (kPa)	Side hardness (N)
	80000	6400	13200	4900	5400



FIGURE 3.2: WOODEN BIKE FRAME FOR TEST

$$E_{11} = V_f E_f + V_m E_m \quad (3.1)$$

$$\frac{1}{E_{22}} = \frac{V_f}{E_f} + \frac{V_m}{E_m} \quad (3.2)$$

$$\frac{1}{G_{12}} = \frac{V_f}{G_f} + \frac{V_m}{G_m} \quad (3.3)$$

$$v_{12} = V_f v_f + V_m v_m \quad (3.4)$$

$$G_{23} = \frac{E_2}{2(1 + v_{23})} \quad (3.5)$$

TABLE 3: MECHANICAL PROPERTY OF INTERNAL UD- GLASS LAMINATE

E_{11}	E_{22}	E_{33}	v_{12}	v_{13}	v_{23}	G_{12}	G_{13}	G_{23}
41612.5	6849.5	6849.5	0.2785	0.2785	0.35	2549.9	2549.9	1203.7

3.2.2. Reverse Engineering and Numerical Modelling of Bicycles Frame

The finished frame was scanned using a 3D optical scanner to generate the STL file shown in Figure 3.3. This file was then imported into CATIA V5. The mesh was cleaned to produce a topologically closed surface model, and then the model was reconstructed in CATIA V5 to correct defects and ensure dimensional accuracy. This resulted in the solid geometry shown in Figure 3.4. The final CAD model was then exported to Abaqus/CAE with the material

orientations defined as orthotropic. The oak frame was meshed using ten-node quadratic tetrahedral solid elements (C3D10) to accurately capture the complex curved geometry and wooden joinery. The internal laminate reinforcement was modelled with 4-node reduced-integration shell elements (S4R), capable of representing either thin or thick shells with finite membrane strains and suitable for defining ply orientations in curved surfaces.

For both the oak frame and the laminate, orthotropic elastic properties were defined using engineering constants (E_1 , E_2 , E_3 , ν_{12} , ν_{13} , ν_{23} , G_{12} , G_{13} , G_{23}) based on experimental data and literature sources as discussed in section 3.2.1. This ensured that anisotropic behaviour was properly captured in the FE analysis.

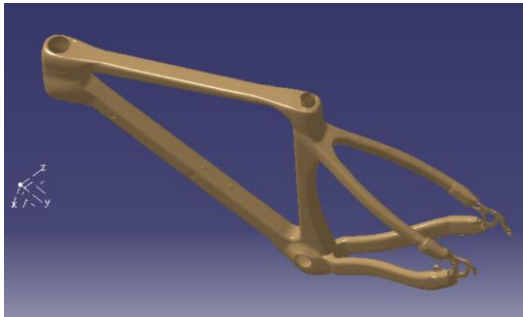


FIGURE 3.3: SCANNED IMAGE OF TEST BIKE
FRAME STL FILE

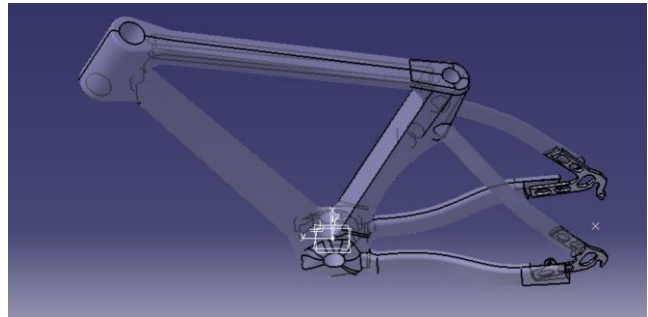


FIGURE 3.4: REVERSED ENGINEERING OF TEST BIKE
FRAME STP FILE

3.2.3. Finite Element Model (FEM) Boundary condition and Load Application

The Finite Element (FE) model replicated the experimental stiffness test configurations for the head tube, bottom bracket, and rear triangle.

- Head tube stiffness: Loads were applied at a reference point positioned at the same offset distance as the dummy fork in the physical test. This reference point was coupled to the nodes on the internal cylindrical surface of the head tube, as shown in Figure 3.4(a & d).
- Bottom bracket stiffness: The load was applied directly to the nodes on the inner cylindrical surface of the bottom bracket shell, as shown in Figure 3.4(b & e).

- Rear triangle stiffness: A reference point was created midway between the rear dropouts, and a lateral concentrated load was applied to this point to simulate the experimental loading condition, as shown in Figure 3.4(c & f).

For all three configurations, supports were defined to replicate the clamping and boundary constraints of the physical rig. This approach ensured that the simulated load paths, support conditions, and resulting deformation patterns matched those observed in the experiments.

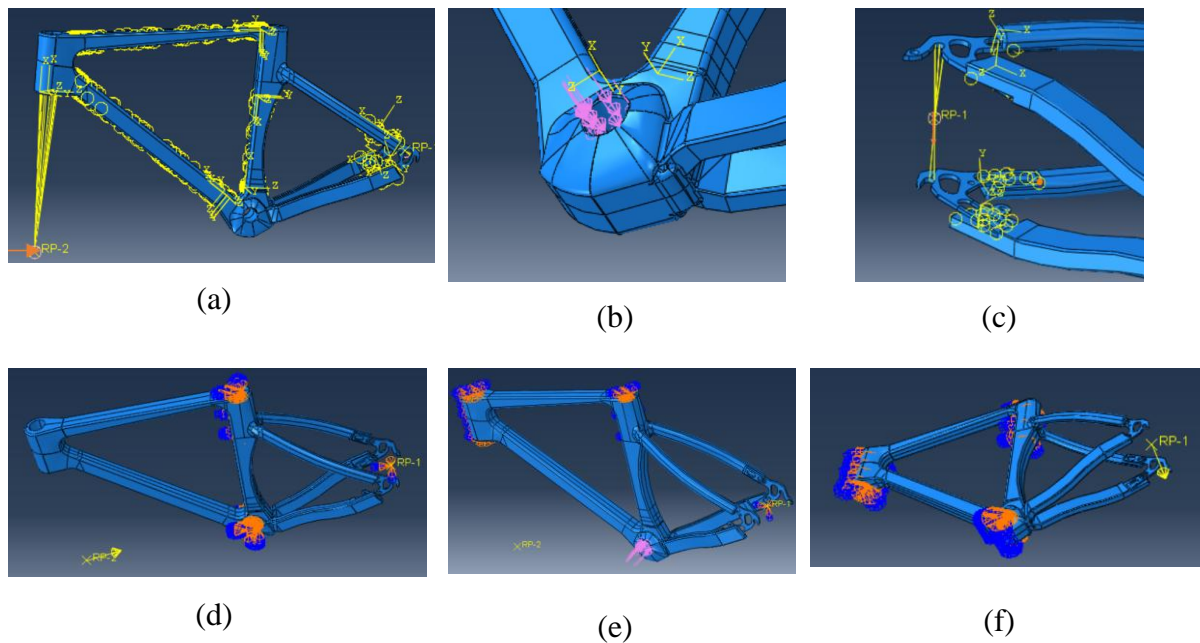


FIGURE 3.5: LOAD APPLICATION AND BOUNDARY CONDITIONS FOR THE BICYCLE FRAME STIFFNESS TESTS: (A) HEAD TUBE – LOAD APPLICATION, (B) BOTTOM BRACKET – LOAD APPLICATION, (C) REAR TRIANGLE – LOAD APPLICATION, (D) HEAD TUBE – BOUNDARY CONDITIONS, (E) BOTTOM BRACKET – BOUNDARY CONDITIONS, (F) REAR TRIANGLE – BOUNDARY CONDITIONS

3.2.4. Post-Processing and Failure Evaluation

For the C3D10 oak elements, Abaqus does not natively allow direct Tsai–Wu evaluation for 3D solids. Instead, the stress results in all three material directions were exported from the Abaqus output database (ODB) into a text file. A custom Python script (see annex C) then read these stress values and applied the Tsai–Wu failure criterion to compute the failure index for each element. Elements exceeding the failure threshold were identified and grouped into a new “failed elements” set, which was written back into the ODB. This allowed the failed regions to be visualised directly in Abaqus/Viewer as an overlay on the FE model.

3.2.5. *Experimental Testing of the Bicycle Frame*

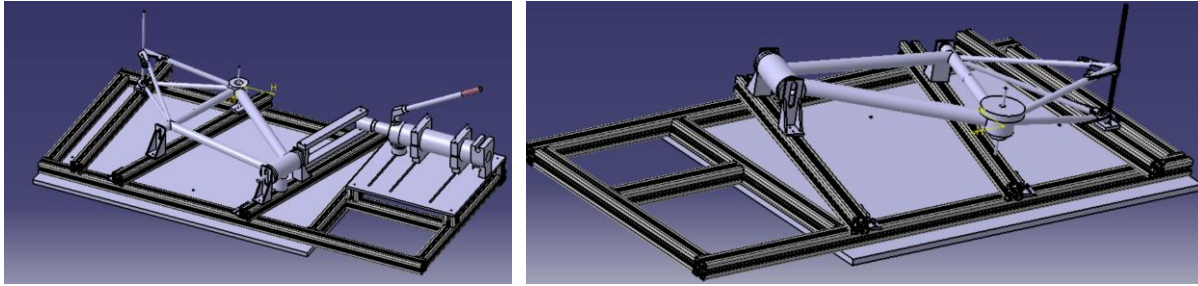
The stiffness of the oak bicycle frame was experimentally determined using a custom test rig designed in CATIA V5 as shown in Figure 3.6 and fabricated in-house. The design concept was adapted and further developed from the low-cost frame jig approach described by Magnani[43]. The rig was modified to allow accurate load application and deflection measurement for stiffness testing in three configurations: head tube, bottom bracket, and rear triangle.

The fabricated rig consisted of aluminium profile members of 40.00x40.00mm and 50.00x50.00mm securely bolted to a rigid wooden table top, providing a stable base for all test configurations (see Figure 3.8-3.9). Adjustable clamping fixtures allowed the bicycle frame to be secured at the required points depending on the stiffness test being performed. Incremental loads were applied statically, by manually operating the mechanical actuator in a smooth, controlled motion (for the head tube stiffness) and by placing an increasing calibrated known weight approximately 5.00kg(50N) at the loading points for the bottom bracket and rear dropout tests. For each load case, the load was held for approximately 10-20 seconds to allow displacement readings to stabilise before recording. Displacements were measured using dial-gauge with a resolution of 0.01 mm.

The test protocol was as follows:

1. Head tube stiffness: vertical load applied at the fork position with seat tube, bottom bracket and rear dropouts fixed (see Figure 3.7).
2. Bottom bracket lateral stiffness: lateral load applied to the crank axis with the frame clamped at the head tube, seat tube and rear axle (see Figure 3.8).
3. Rear triangle lateral stiffness: lateral load applied to the rear axle with the Head tube, seat tube and bottom bracket fixed (see Figure 3.9).

Stiffness values ($k = \frac{P}{\delta}$) were calculated from the slope of the load–displacement curves for each configuration.



(a)

(b)

FIGURE 3.6: DETAILED DESIGN OF TEST RIG FOR BICYCLE STIFFNESS ASSESSMENT

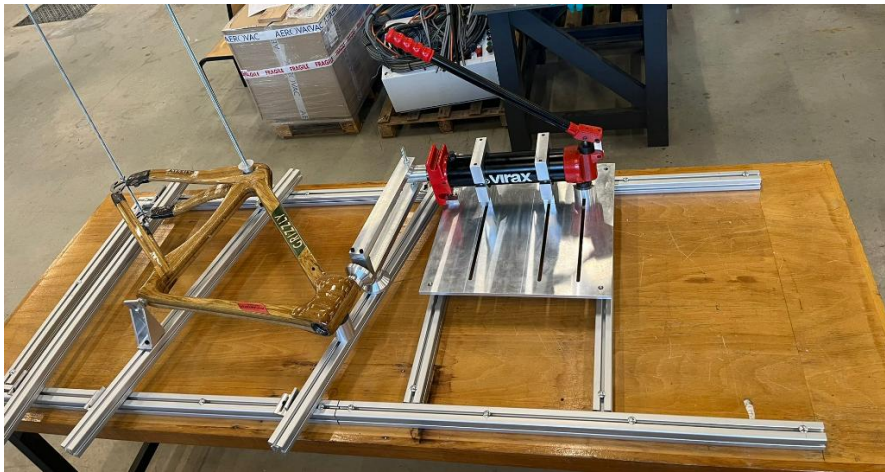


FIGURE 3.7: LABORATORY SET-UP OF BICYCLE TEST RIG FOR HEAD TUBE STIFFNESS CHECK

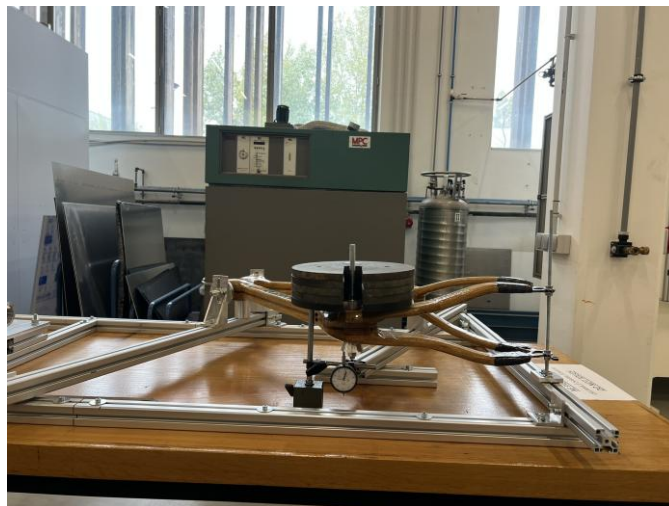


FIGURE 3.8: LABORATORY SET-UP OF BICYCLE TEST RIG FOR BOTTOM BRACKET STIFFNESS CHECK



FIGURE 3.9: LABORATORY SET-UP OF BICYCLE TEST RIG FOR REAR TRIANGLE STIFFNESS CHECK

3.3. Case Study 2: IMOCA Sandwich Specimens

The IMOCA test specimens were marine plywood cores with face-sheets made from carbon, basalt or glass fibre fabrics, as provided by the client. The control specimens were made of plywood without any face-sheets. As stated in Section 3.1, a total of 234.

The thickness of the plywood and FRP face-sheets was measured using magnified scanning for each group of specimens with the same face-sheet type and orientation. These thicknesses were used directly in Abaqus models.

3.3.1. *Experimental Procedures and Equations*

Quasi-static bending experiments were carried out using a universal testing machine equipped with a 100 KN load cell, as illustrated in Figure 3.10. Both three-point and four-point bending tests were performed in accordance with the relevant ASTM standards as shown Table 5 for wood and sandwich structures, with the aim of evaluating flexural properties under controlled loading. The inclusion of four-point bending allowed the shear deformation component to be considered in the determination of bending modulus by comparing results from the two configurations.

For each material configuration, a minimum of six specimens was tested. The samples were supported on two cylindrical rollers (10.00 mm diameter). For the 3-point, the samples were positioned at a span length of 250.00 mm, with the total span length of 350.00mm while for the

4-point, the samples were positioned at a span length of 300.00 mm, with the total span length of 450.00 mm. Loading was applied at a constant crosshead displacement rate of 5.50 mm/min. The applied load and actuator displacement were recorded directly from the testing machine. Two of the samples for each configuration were preserved to be tested using the Digital image correlation (DIC) system to properly capture the displacement values and its failure mode.



FIGURE 3.10: UNIVERSAL TESTING MACHINE WITH 3-POINT FLEXURAL TEST CONFIGURATION

Each test was conducted in accordance with required ASTM and the stresses computed based on the required ASTM as shown in Table 5. A complete summary of the tested configurations, orientations, and face-sheet types is provided in Table 4 with the specimen arrangement as shown in Figure 3.11.

TABLE 4: TEST MATRIX OF PLYWOOD CORE BASED SANDWICH STRUCTURES FOR QUASI-STATIC BENDING TEST (3P-3 POINTS, 4P-4 POINTS) WITH DIFFERENT FACE-SHEET AND CONTROL SPECIMEN

Material Type	Orientation (°)	3-point Flexural Test	4-point Flexural Test	Tensile Test	Sub-Total
Control Plywood without Face-sheet		10	10	10	30
Plywood core with Glass Face-sheet	0	10	10	10	30
	45	-	-	9	9
	90	10	10	10	30
Plywood core with Basalt Face-sheet	0	10	10	10	30
	45	-	-	10	10
	90	10	10	10	30
Plywood core with Carbon Face-sheet	0	10	9	10	29
	45	-	-	9	9
	90	9	9	9	27
TOTAL SAMPLES					234

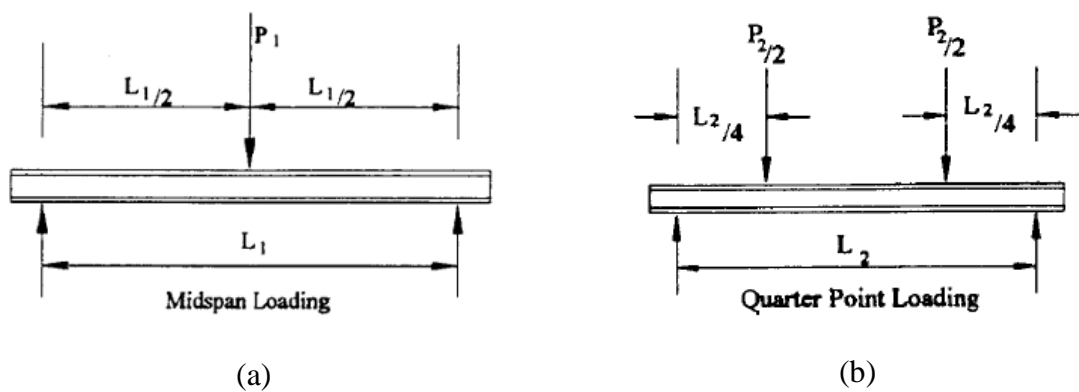


FIGURE 3.11: FLEXURE TEST CONFIGURATION (A) 3-POINT CONFIGURATION (B) 4-POINT CONFIGURATION

TABLE 5: FLEXURAL AND TENSILE TEST EQUATIONS

Specimen-Type	Test	Formula	Reference Code
Plywood only	3-point	$\sigma_f = \frac{3PL}{2bd^2} \left[1 + 6 \left(\frac{D}{L} \right)^2 - 4 \left(\frac{d}{L} \right) \left(\frac{D}{L} \right) \right]$	ASTM D790[44]
	4-point	$\sigma_f = \frac{3PL}{4bd^2} \left[1 - \left(\frac{10.91Dd}{L^2} \right) \right]$	ASTM D6272[18]
	Tensile	$\sigma_t = \frac{P}{A}$	ASTM D3039/D3039M[45]
Sandwich (with Plywood core)	3-point	$\sigma_f = \frac{PL}{2t(d+c)b}$	ASTM C393[46]
	4-point	$\sigma_f = \frac{PL}{4t(d+c)b}$	ASTM C393[46]
	Tensile	$\sigma_t = \frac{P}{A}$	ASTM D3039/D3039M[45]
	3-Point & 4-Point	$\tau_{core} = \frac{P}{(d+c)b}$	ASTM C393

In the above formulas the following parameters are used:

σ_f = stress in the outer fibres at midpoint, MPa,

τ_{Core} = core shear stress

P = load at a given point on the load-deflection curve, N,

L = support span, mm,

t = facing thickness, mm,

c = core thickness, mm,

σ_t = tensile stress at ith data point, MPa,

A = average cross-sectional area, mm²,

b = width of beam tested, mm, and

d = depth of beam tested (total sandwich thickness for 4-point), mm.

3.3.2. Numerical Model Setup

The numerical simulation of the IMOCA-sandwich panels was carried out in Abaqus/CAE. Each specimen was modelled as a layered composite with explicit definition of the plywood core and FRP face-sheets. The thickness was assessed using microscope and the average of each ply thickness is as shown in Figure 3.12 while a complete image can be seen in Annex I. The core was assigned same Engineering elastic properties of Oak wood as indicated in Table 2 of section 3.2.1 due to lack of feedback from the client on the type of wood as at the time of this study.

Face-sheets were defined using orthotropic properties for carbon, glass, or basalt FRP laminates as obtained from manufacturers' datasheets[47], [48], [49], [50] as shown in Table 6.

For the meshing, the plywood core was discretised using C3D8R hexahedral elements to represent 3D stress states and avoid shear locking. Face-sheets were modelled using S4R shell elements tied to the core's outer surfaces via surface-based tie constraints, enabling distinct property definitions while ensuring displacement compatibility. The boundary conditions and loading, were modelled as analytical rigid cylinders of 10.00mm as well as the supports at the specified span lengths (250.00 mm and 300.00 mm) in the 3-point and 4-point bending respectively. A central rigid loading roller applied a prescribed load derived from the experimental results as shown in Figure 3.13. Additionally, For the 4-point bending, two loading rollers were positioned symmetrically about midspan. In both cases, contact between rollers and panel was defined as surface-to-surface with hard normal behaviour and friction tangential behaviour of 0.3.

For both tests, the damage initiation in the FRP face-sheets was estimated using the Tsai–Wu criterion with focus on the face-sheets. The Finite element model failure criteria was used to identify damage initiation sites for comparison with experimental failure modes.

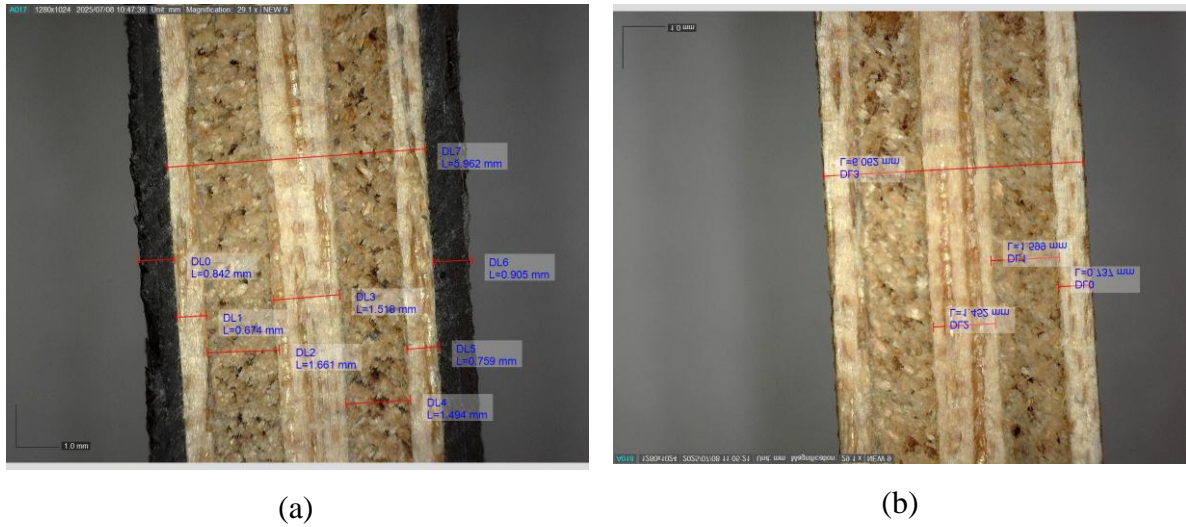


FIGURE 3.12: MICROSCOPIC IMAGE OF IMOCA SPECIMEN SHOWING EACH PLY THICKNESS (A) SANDWICH WITH PLYWOOD CORE AND BASALT FACE-SHEET (B) CONTROL SPECIMEN OF PLYWOOD ONLY ORIENTATED AT 0° AND 90°

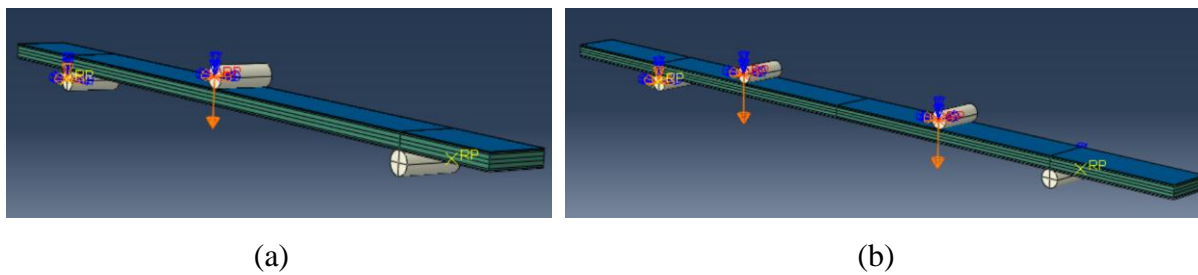


FIGURE 3.13: BENDING TEST MODEL SET-UP (A) 3-POINT FLEXURAL TEST (B) 4-POINT FLEXURAL TEST

TABLE 6: SANDWICH FACE-SHEET MECHANICAL PROPERTY

Face-sheet Material	E_{11}	E_{22}	E_{33}	U_{12}	U_{13}	U_{23}	G_{12}	G_{13}	G_{23}
Carbon (CarbonT300/5208)	181000	10300	10300	0.24	0.24	0.4	7170	7170	3678.6
Glass (E-glass/epoxy)	40510	13960	13960	0.22	0.22	0.4	3100	3630	4985.7
Basalt (Basalt_UD/ResinEpoxy)	44300	11900	11900	0.27	0.27	0.3	3730	3730	4577

4. RESULTS AND DISCUSSIONS

This chapter presents the results of the experimental tests and numerical simulations of the oak bicycle frame and the IMOCA-inspired sandwich specimens. The findings are organised into two main sections, which correspond to the two case studies. For each case, the experimental data, including stiffness measurements, flexural strength and observed failure modes, are reported first. These results are then compared with the predictions from the finite element simulations in order to assess the accuracy and reliability of the model. The discussion section highlights key trends, validates modelling approaches and explains any discrepancies between the experimental and numerical outcomes. Finally, the broader implications of the results are considered, particularly with regard to the feasibility of wooden structures in sustainable transport applications.

4.1. Case Study 1: Wooden Bicycle Frame

4.1.1. Bicycle Experimental Stiffness Results

The oak bicycle frame was tested in three configurations: bottom bracket (Figure 4.1), and rear triangle (Figure 4.2).

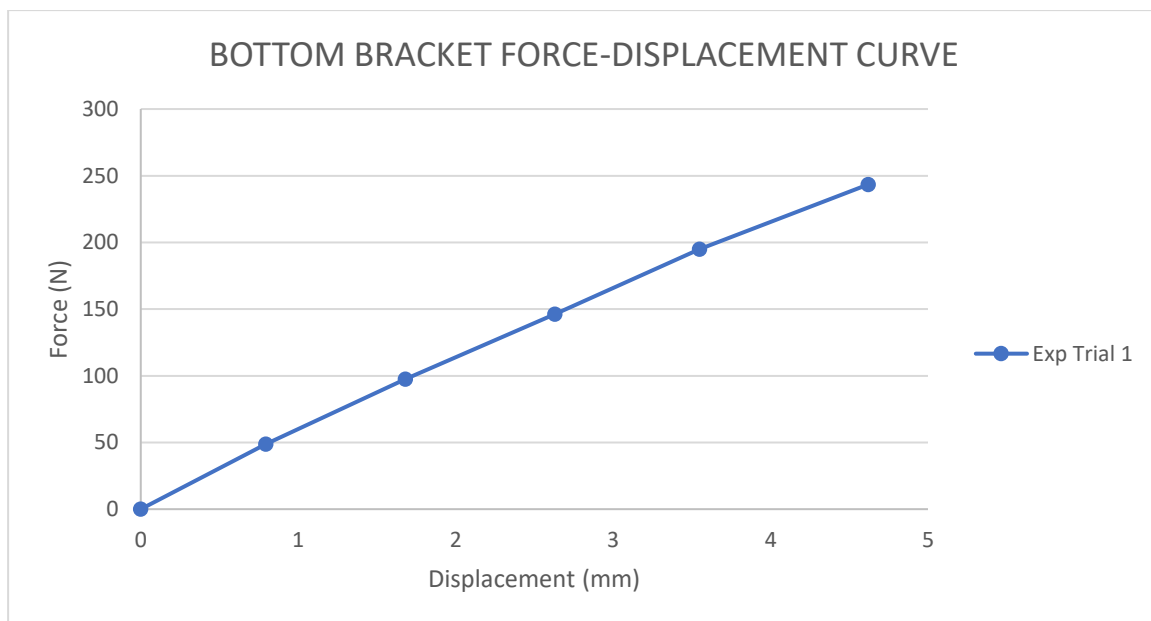


FIGURE 4.1: BOTTOM BRACKET STIFFNESS EXPERIMENTAL LOAD-DISPLACEMENT CURVE

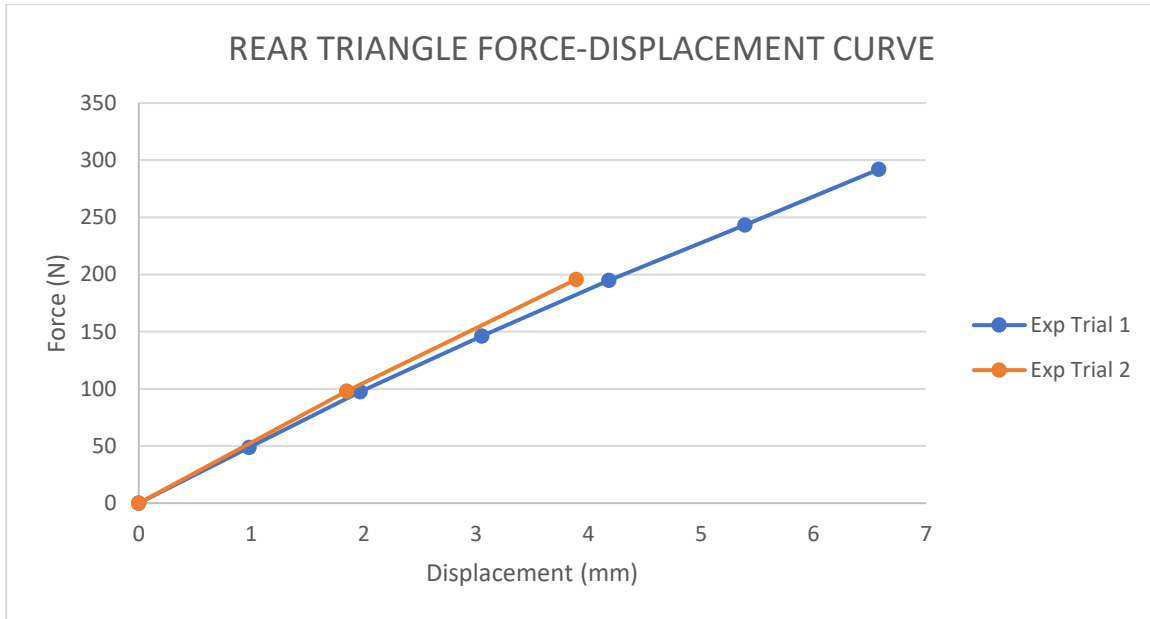
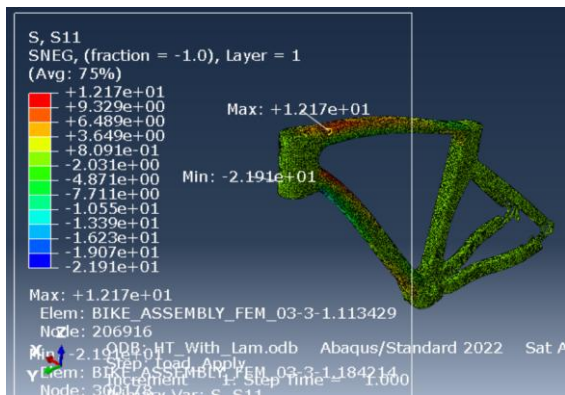


FIGURE 4.2:REAR TRIANGLE STIFFNESS EXPERIMENTAL LOAD-DISPLACEMENT CURVE

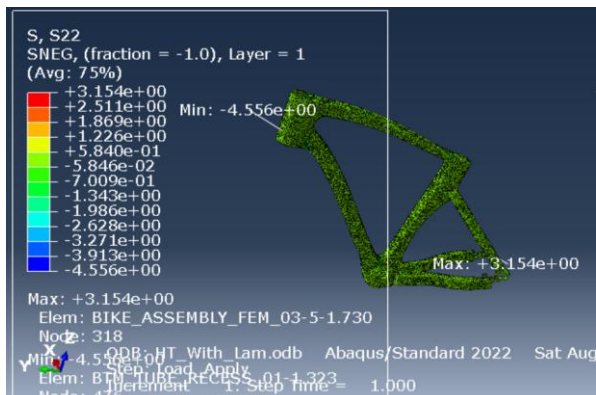
4.1.2. FEM Stiffness Predictions and Correlation

The finite element model replicated the experimental test setups with appropriate boundary conditions.

First of for the head tube a load of 500N was applied which is slightly higher than the value of 449N proposed by Soden et al.,[51]. The stresses and deflection in response to the load applied was investigated against the ultimate strength of the frame. This is shown in the Figure 4.3(a-d) below.



(a)



(b)

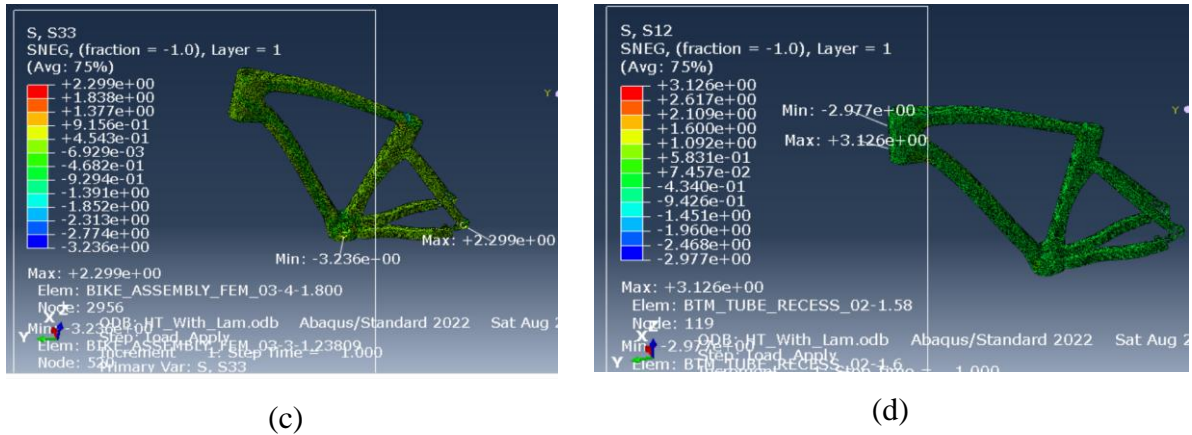


FIGURE 4.3: HEAD TUBE LOAD RESPONSE STRESS DISTRIBUTION DIAGRAM: (A) NORMAL STRESS DISTRIBUTION IN S11 DIRECTION, (B) NORMAL STRESS DISTRIBUTION IN S22 DIRECTION, (C) NORMAL STRESS DISTRIBUTION IN S33 DIRECTION, (D) SHEAR STRESS DISTRIBUTION IN S12 DIRECTION

TABLE 7: HEAD TUBE SUMMARY TABLE OF THE MAXIMUM STRESS DISTRIBUTION AND DIRECTION OF STRESSES

Parameter	S11	S22	S33	S12
Assessed(stresses)				
Max. Values(Mpa)	12.17	4.55	2.30	3.13

The above shows the stresses based on the applied load at a specific distance to imitate the dummy fork position. Firstly, the bike deformation behaviour is as expected, and can be said from the FEM point of view that the model is valid, but would however need to be validated with the experimental data.

The Stress distribution plots showed that the largest stresses occurred along the fibre (S11) direction of oak, with a peak value of approximately 12 Mpa as further show in the summary Table 7. This is substantially below the longitudinal compressive strength of oak, reported to be about 45 Mpa [8], confirming that the material remains in the elastic range. In addition to the normal stresses along the fibre direction, the FEM simulations also revealed the distribution of shear stresses (S12, S13, S23) with the S12 being the highest and shown in Figure 4.3 (d) across the frame. The maximum shear stress recorded under the applied load was approximately 3.13 MPa, which is well below the in-plane shear strength of oak (≈ 13.2 Mpa). This indicates that shear forces induced at the joints and tube intersections are negligible compared to the material capacity. Consequently, shear stress does not represent a governing failure mode under the present loading conditions and poses no significant structural concern within the elastic range.

Subsequently, Figure 4.4 (a-d) shows the deflection response in various direction.

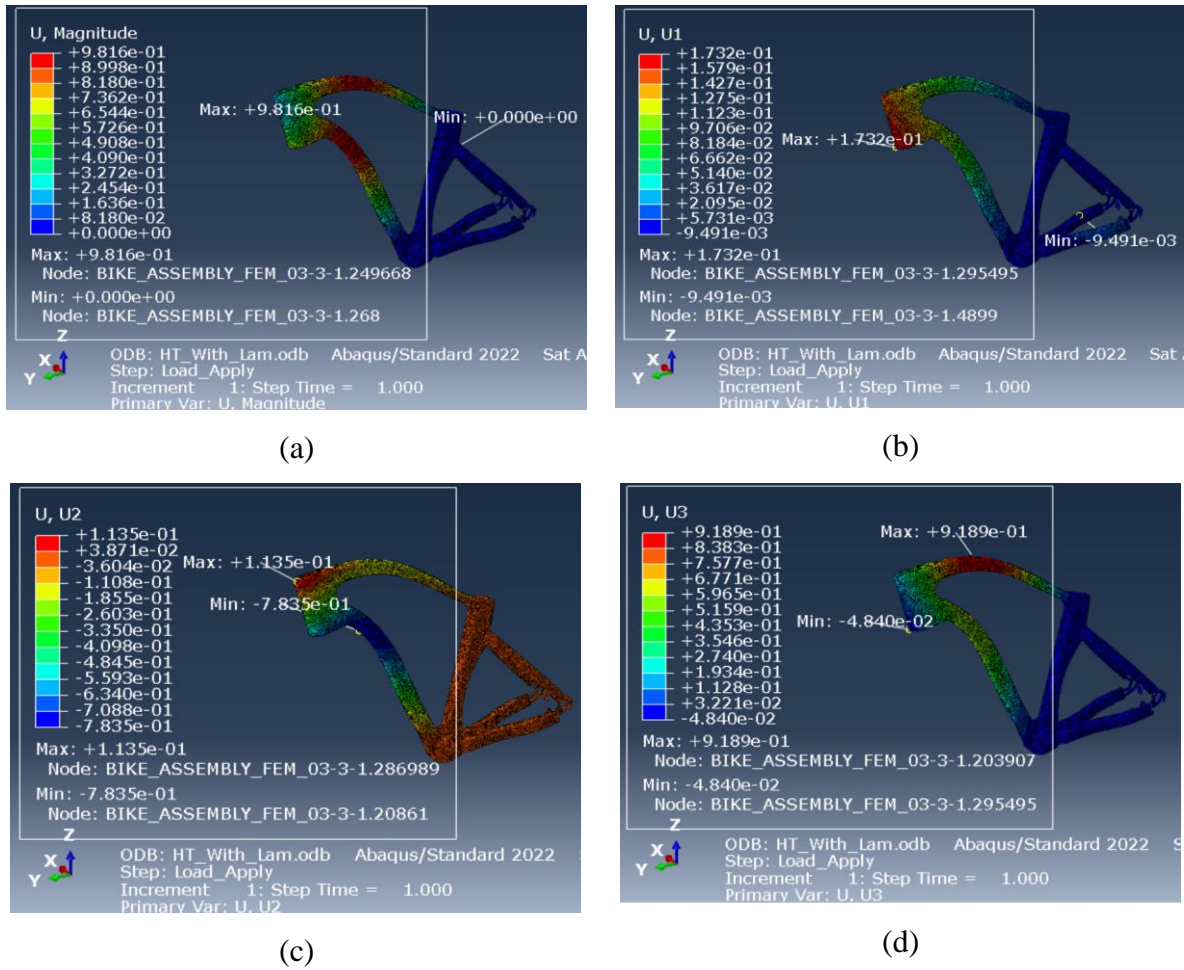


FIGURE 4.4: HEAD TUBE LOAD RESPONSE DISPLACEMENT DIAGRAM: (A) GLOBAL MAXIMUM DEFLECTION, (B) DEFLECTION RESPONSE IN THE U1 DIRECTION, (C) DEFLECTION RESPONSE IN THE U2 DIRECTION, (D) DEFLECTION RESPONSE IN THE U3 DIRECTION

TABLE 8: HEAD TUBE SUMMARY TABLE OF THE MAXIMUM DEFLECTIONS IN VARIOUS DIRECT

Parameter	U_{max}	U_1	U_2	U_3
Assessed(deflection)				
Max. Values(mm)	0.98	0.17	0.11	0.92

From the Figure 4.4 (a-d) above, it can be seen that the Frame experienced an overall maximum deformation of 0.98mm. This shows that the bike is quite stiff and resistant to deformation that may arise due to application of horizontal braking load. Further investigation shows that the U3 was the main direction that experience the signifant deflection with a value of 0.92mm and for better understanding of the general behaviour, deflection in other direction was examined and it can be seen that the values are relatively low compared to the deflection in the U3 direction.

Similarly, the bottom bracket (BB) was loaded to represent out-of-plane pedalling forces and chain pull. The frame was constrained at the rear contact points of the dropouts, the seat tube and at the head-tube support locations used in the rig, while a lateral force of 600N was applied to check the localized lateral stiffness which was in accordance to Dvořák et al. [52], was applied at the BB region as explained in the methodology section. This produces a primarily sagging deformation mode about the BB shell, with secondary torsion carried by the chainstays and seat-tube. both the stresses and the deflection was also checked and are as shown the Figure 4.5(a-d) below.

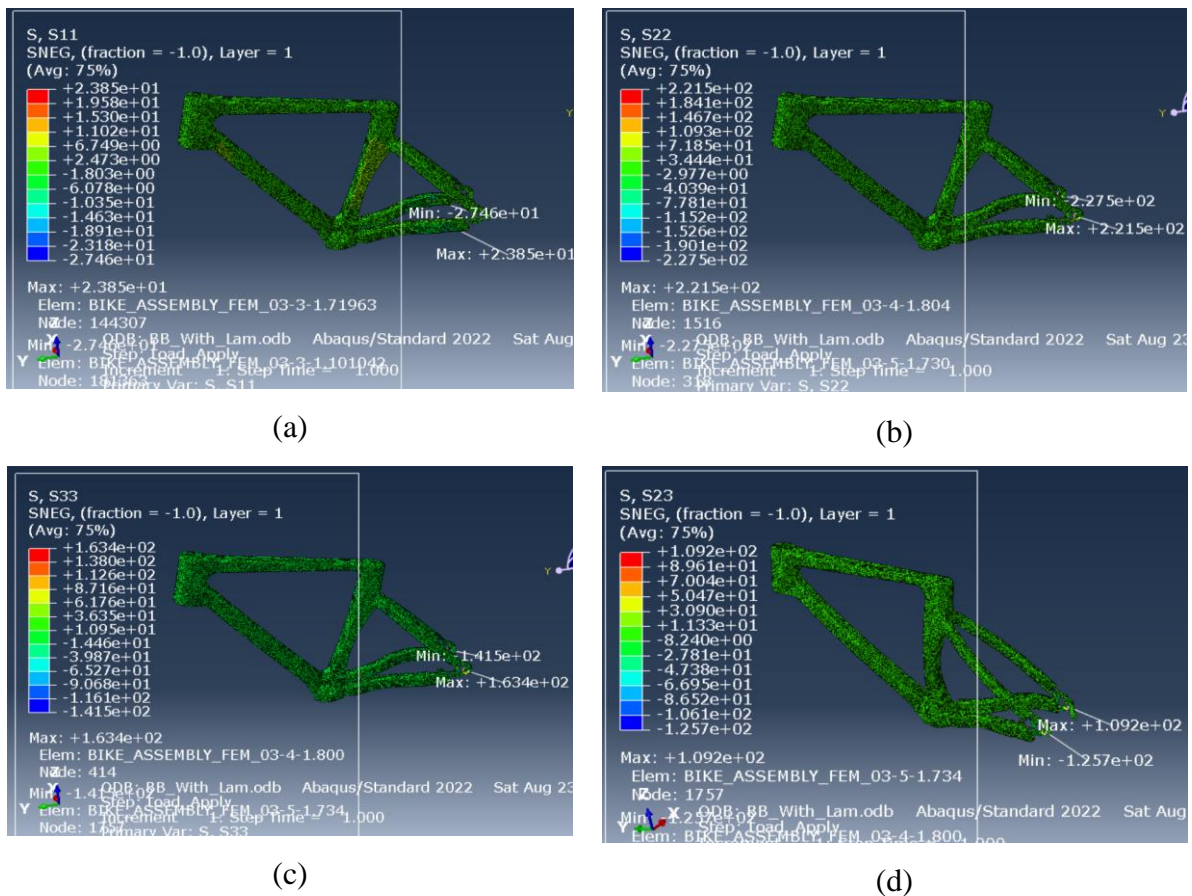


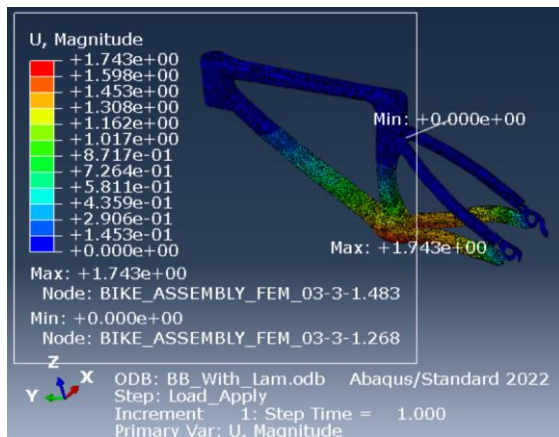
FIGURE 4.5: BOTTOM BRACKET LOAD RESPONSE STRESS DISTRIBUTION DIAGRAM: (A) NORMAL STRESS DISTRIBUTION IN S11 DIRECTION, (B) NORMAL STRESS DISTRIBUTION IN S22 DIRECTION, (C) NORMAL STRESS DISTRIBUTION IN S33 DIRECTION, (D) SHEAR STRESS DISTRIBUTION IN S23 DIRECTION

TABLE 9: BOTTOM BRACKET SUMMARY TABLE OF THE MAXIMUM STRESS DISTRIBUTION AND DIRECTION OF STRESSES

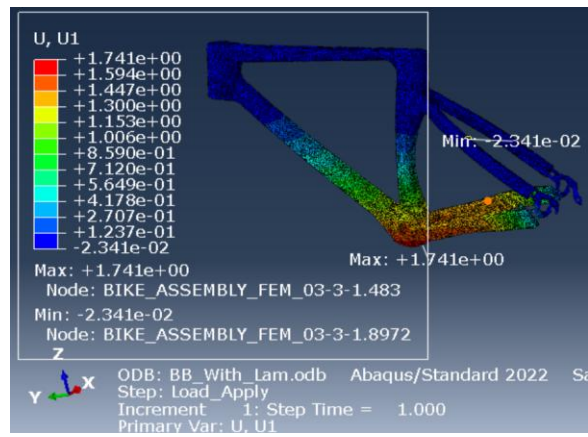
Parameter	S11	S22	S33	S23
Assessed(stresses)				
Max. Values(Mpa)	27.46	227.50	163.4	125.7

the Figure 4.5 (a-d) above shows that while the stress, S11 which is 27.46 MPa, it remains comfortably below the longitudinal capacity of oak, indicating an elastic response for the governing fibre direction. By contrast, the very high transverse (S22, S33) and out-of-plane shear (S23) peaks are highly localised hot-spots at geometric transitions and constraint/contact regions; in orthotropic wood FE these are notably sensitive to mesh density, local fillet radius, and contact stiffness. They should be interpreted as local numerical concentrations rather than section-averaged design stresses. These are substantially higher than the compressive strength of oak, reported to be about 45 Mpa [8]. This suggest the need to further investigate this to know the regions that may be prone to this excessive stresses.

Subsequently, the Deflection behaviour was investigated and are as shown in Figure 4.6 (a-d) below.



(a)



(b)

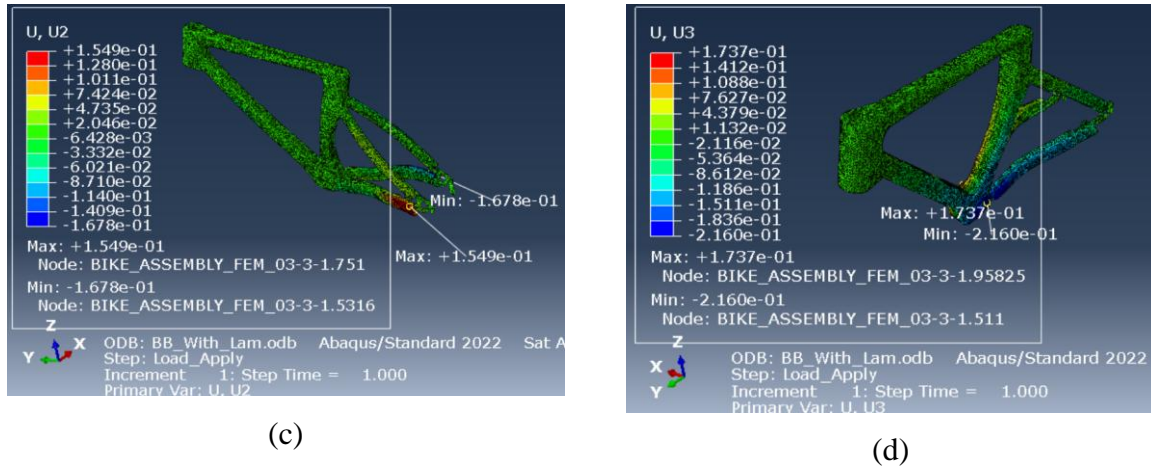


FIGURE 4.6: BOTTOM BRACKET LOAD RESPONSE DISPLACEMENT DIAGRAM: (A) GLOBAL MAXIMUM DEFLECTION, (B) DEFLECTION RESPONSE IN THE U1 DIRECTION, (C) DEFLECTION RESPONSE IN THE U2 DIRECTION, (D) DEFLECTION RESPONSE IN THE U3 DIRECTION

TABLE 10: BOTTOM BRACKET SUMMARY TABLE OF THE MAXIMUM DEFLECTIONS IN VARIOUS DIRECTION

Parameter	U_{max}	U_1	U_2	U_3
Assessed(deflection)				
Max. Values(mm)	1.94	1.74	0.15	0.22

Figure 4.6 presents the deformation field for the bottom-bracket load case: (a) the global displacement magnitude U , and the component displacements in the model axes (b) U_1 , (c) U_2 , and (d) U_3 . Consistent with the color maps, Table 10 reports a global maximum deflection of 1.94mm, with component peaks $U_1 = 1.74$ mm, $U_2 = 0.15$ mm, and $U_3 = 0.22$ mm. The dominance of U_1 ($\approx 90\%$ of U_{max}) shows that the deformation is governed primarily by bending/translation along the model’s 1-axis, while vertical (U_2) and lateral (U_3) components remain small. This pattern indicates that the load path from the bottom bracket into the nearby members is efficient and that the frame does not exhibit appreciable out-of-plane twisting under the present load of study.

Also the Stiffness for the rear-triangle was checked under a conservative load case of 300N with a lateral force applied at the rear axle; the model reproduces the rig boundary conditions defined earlier (rear axle load with head tube, seat tube and BB constrained). Both the stress and displacement responses were assessed and are as shown in the Figure 4.7 (a-d) below.

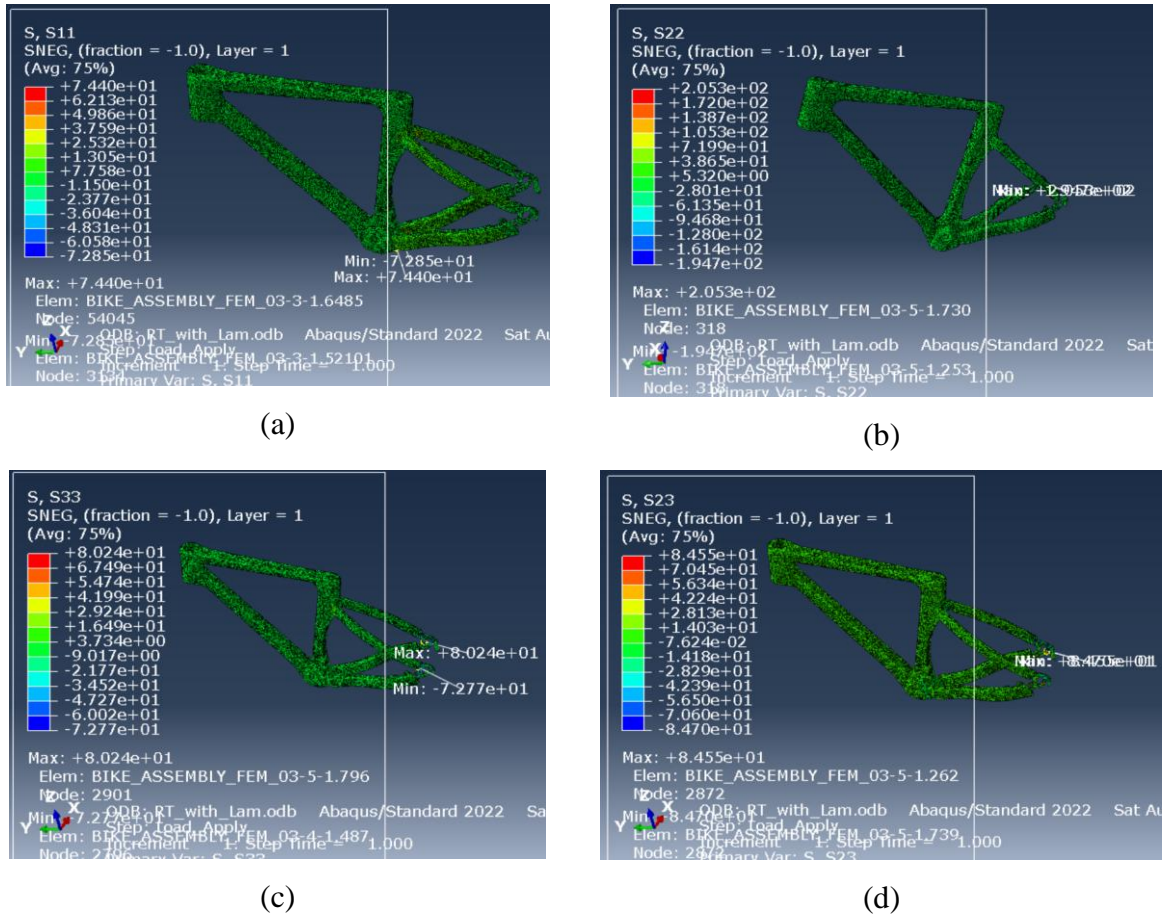


FIGURE 4.7: REAR TRIANGLE LOAD RESPONSE STRESS DISTRIBUTION DIAGRAM: (A) NORMAL STRESS DISTRIBUTION IN S11 DIRECTION, (B) NORMAL STRESS DISTRIBUTION IN S22 DIRECTION, (C) NORMAL STRESS DISTRIBUTION IN S33 DIRECTION, (D) SHEAR STRESS DISTRIBUTION IN S23 DIRECTION

TABLE 11: REAR TRIANGLE SUMMARY TABLE OF THE MAXIMUM STRESS DISTRIBUTION AND DIRECTION OF STRESSES

Parameter	S11	S22	S33	S12
Assessed(stresses)				
Max. Values(Mpa)	74.40	205.3	80.24	84.55

The Figure 4.7 illustrates the stress maps includes the normal shears and the dominant shear component. The corresponding peaks from Table 11 are S11=74.40 MPa, S22=205.3 MPa, S33 =80.24 MPa, and shear S12 =84.55 MPa. The pattern is mechanically consistent with a lateral axle force: the chainstays/seatstays act as a couple, generating tension–compression lobes in the fibre direction (governing S11) and a shear ridge that propagates from the dropout into the stay roots. Because oak is strongly orthotropic, this along-grain component is the most relevant for assessing utilisation; the present value indicates that the rear triangle is the most highly

stressed of the three frame checks and would be the first region to approach a tensile-parallel-to-grain limit if the lateral axle load were increased. This identifies the dropout–stay junctions as the primary locations for strain measurement and, if required, local reinforcement in the experimental phase.

The very high transverse (S22,S33) and shear peaks are confined to small regions near constraints and sharp transitions which would be further investigated. In orthotropic wood FE models, these components are particularly sensitive to many reasons such as (i) the way axle loads are transferred, (ii) local mesh density and contact stiffness etc. For this reason, they should be treated as local hot-spots rather than section-level design stresses.

Subsequently, the deflection response was assessed. Figure 4.8 illustrates the displacement field of the rear triangle under the prescribed load at the rear axle/dropout, with Table 12 summarising the maxima.

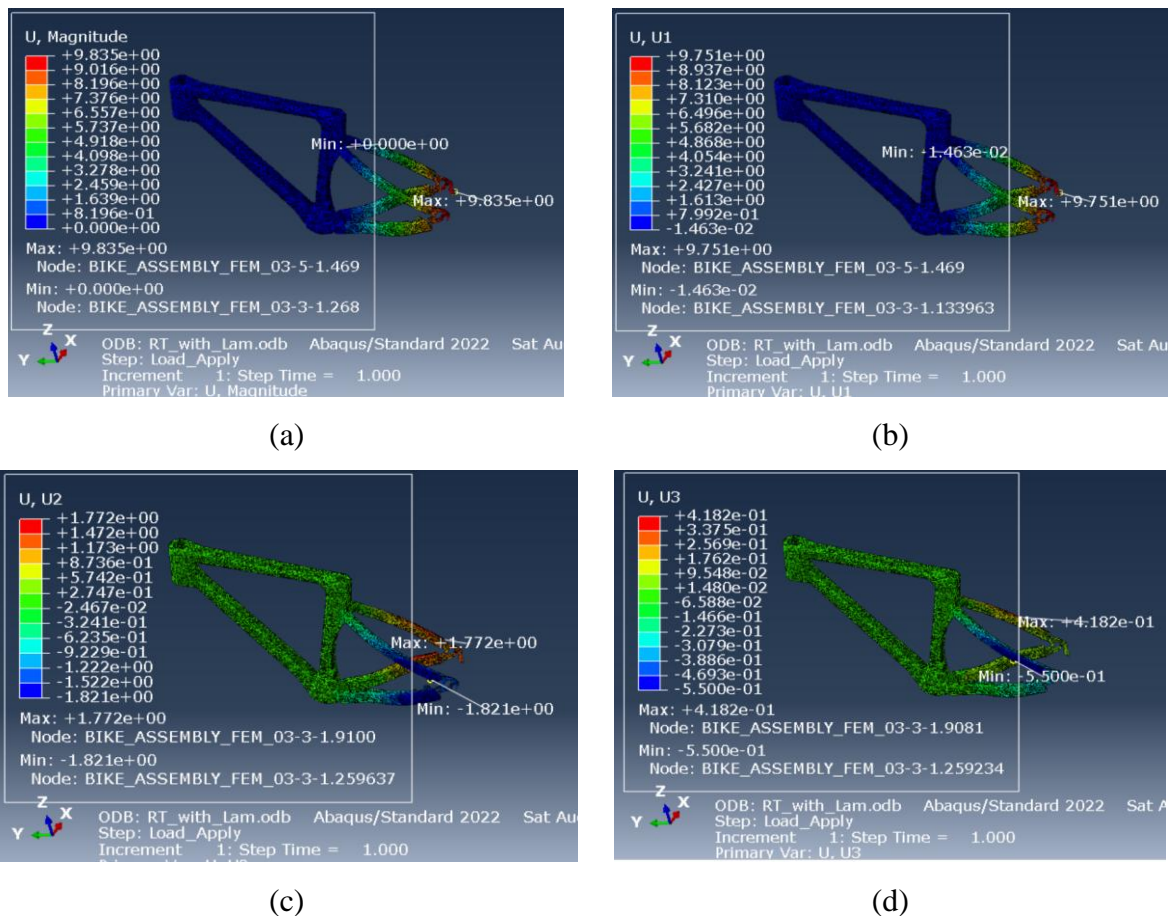


FIGURE 4.8: REAR TRIANGLE LOAD RESPONSE DISPLACEMENT DIAGRAM: (A) GLOBAL MAXIMUM DEFLECTION, (B) DEFLECTION RESPONSE IN THE U1 DIRECTION, (C) DEFLECTION RESPONSE IN THE U2 DIRECTION, (D) DEFLECTION RESPONSE IN THE U3 DIRECTION

TABLE 12: REAR TRIANGLE SUMMARY TABLE OF THE MAXIMUM DEFLECTIONS IN VARIOUS DIRECTION

Parameter Assessed(deflection)	U_{\max}	U_1	U_2	U_3
Max. Values(mm)	9.84	9.75	1.77	0.42

From Table 12, the global maximum displacement is 9.84 mm, with component peaks $U_1 = 9.75$ mm, $U_2 = 1.77$ mm, and $U_3 = 0.42$ mm. The response is therefore strongly dominated by U_1 , the in-plane direction of the applied lateral load: U_1 is about $5.5 \times U_2$ and $\approx 23 \times U_3$, indicating little vertical compliance and minimal out-of-plane twisting.

4.1.3. Post Processing for failure assessment

The results of the finite element simulations were post-processed to evaluate failure in the wooden bicycle frame using the Tsai–Wu failure criterion in a full 3D stress state. Since the frame was modelled with 3D solid elements (C3D10), Abaqus does not provide a built-in option to apply the Tsai–Wu criterion directly to these elements. This limitation necessitated the development of a custom Python script for post-processing (see Figure 4.9a-c). The script extracted the relevant stress tensor components (S_{11} , S_{22} , S_{33} , S_{12} , S_{13} , S_{23}) from the Abaqus output database and calculated the Tsai–Wu failure index for every element.

First of all, the wooden part of the frame was separated from the metallic rear dropout components. The Tsai–Wu criterion was applied exclusively to the wooden elements, given their orthotropic and anisotropic nature, while the Von Mises stress criterion was employed for the steel dropout. This distinction ensured that the two different material behaviours were appropriately captured: Tsai–Wu accounts for the combined action of longitudinal, transverse, and shear stresses in orthotropic wood, while Von Mises provides a reliable measure of yielding in ductile, isotropic steel.

Through this approach, failure assessment was carried out independently of Abaqus’ standard material model framework. Elements exceeding a Tsai–Wu index of unity (for wood) or the Von Mises yield strength (for steel) were automatically identified as failed and grouped into new element sets (see Figure 4.10-4.13). These sets were then imported back into Abaqus, enabling direct visualization of where failure was predicted to occur. The procedure allowed

the integration of two different failure theories into the same simulation framework, reflecting the hybrid nature of the frame.

The custom Python script which was used is attached in the Annex II for reference.

```

✓ Tsai-Wu evaluation complete.
→ Total elements evaluated: 1524032
→ Failed elements: 0
→ Failed element IDs saved to:
C:\temp\My thesis\Bike Frame Project\Head Tube Stiffness\Head Tube with Laminate\HT_2 Post_Proce
ssing\HTfailed_elements_comma.txt
PS C:\Users\HP\Downloads\my Python practice>
    
```

(a)

```

✓ Tsai-Wu evaluation complete.
→ Total elements evaluated: 1524032
→ Failed elements: 0
→ Failed element IDs saved to:
C:\temp\My thesis\Bike Frame Project\BB Stiffness\BB with Laminate\BB_2 Post_Processing\failed_e
lements_comma.txt
    
```

(b)

```

✓ Tsai-Wu evaluation complete.
→ Total elements evaluated: 1524032
→ Failed elements: 128
→ Failed element IDs saved to:
C:\temp\My thesis\Bike Frame Project\Rear Triangle stiffness\Rear Triangle with Laminate\RT_2 Po
st_Processing\RTfailed_elements_comma.txt
PS C:\Users\HP\Downloads\my Python practice>
    
```

(c)

FIGURE 4.9: PYTHON CUSTOM TSAI-WU FAILURE CHECK OUTPUT: (A) HEAD TUBE FAILED ELEMENT RESULTS (B) BOTTOM BRACKET TUBE FAILED ELEMENT RESULTS (C) REAR TRIANGLE FAILED ELEMENT RESULTS

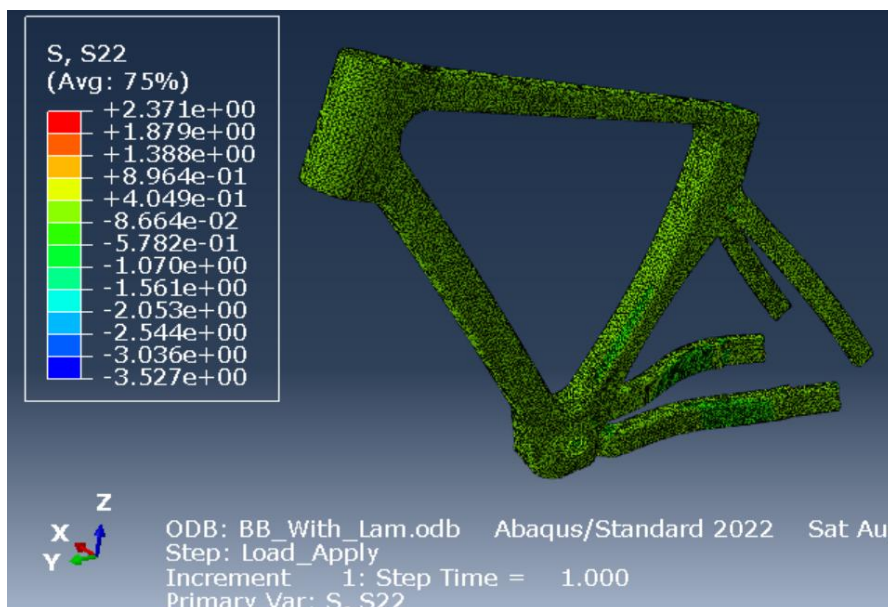


FIGURE 4.10: STRESS CONTOUR OF WOODEN SECTION OF FRAME ONLY BASED ON STIFFNESS CHECK

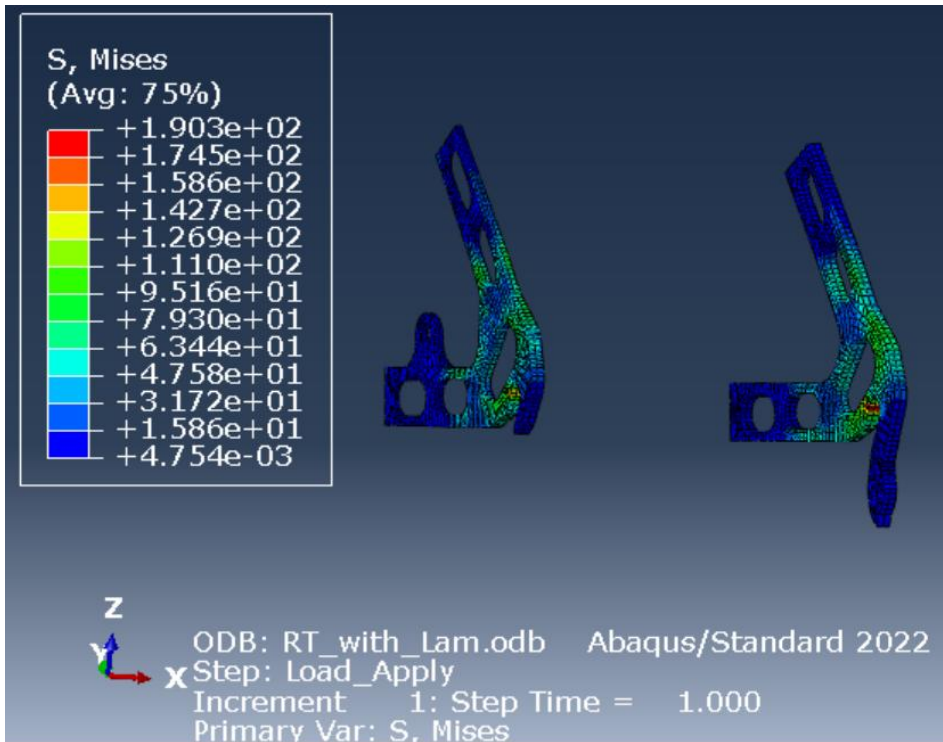


FIGURE 4.11: STRESS CONTOUR OF REAR DROPOUT

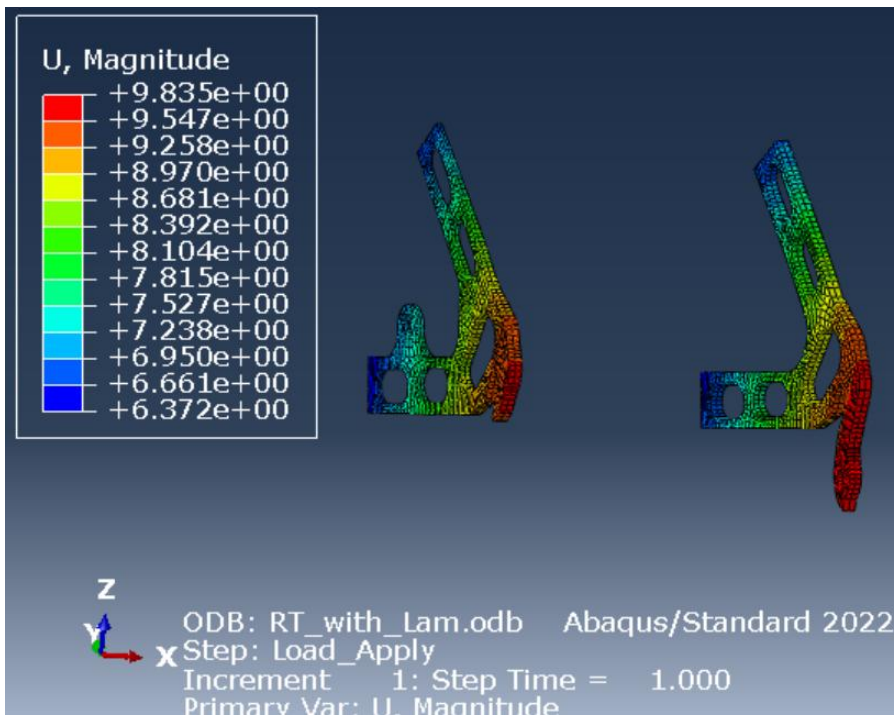


FIGURE 4.12: DEFLECTION CONTOUR OF REAR DROPOUT

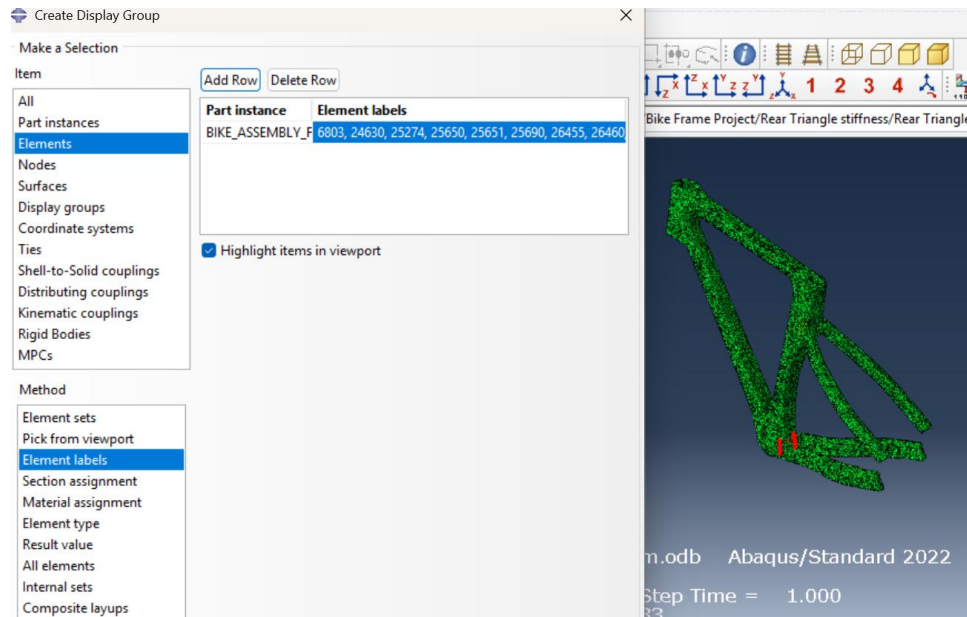


FIGURE 4.13: VISUALIZATION OF STRESS CONCENTRATION OF FAILED ELEMENTS FROM REAR TRIANGLE STIFFNESS CHECK

Figure 4.9 presents the output of the custom Python script developed for Tsai–Wu failure evaluation. As shown in Figures 4.9(a) and 4.9(b), no elements failed in either the head tube or the bottom bracket stiffness checks. Although high stresses were recorded during these simulations, the post-processing confirmed that all elements within the wooden sections of the frame remained below the Tsai–Wu failure envelope. For a clearer understanding Figure 4.10, shows the transverse stress component S_{22} was 2.37MPa, in contrast to the initial value of 227.50 MPa. To further investigate the source of the initially high stress values, attention was directed to the rear dropout assembly, which is made of steel. The stress contour in Figure 4.11 indicates that the rear dropout experienced a maximum Von Mises stress of approximately 190.30 MPa. This value is well below the ultimate strength of the steel, and therefore does not raise concern for yielding or plastic deformation. The finding reinforces that, under the applied loading conditions, the head tube and bottom bracket regions of the wooden frame are structurally safe, while the stresses observed in the dropout remain within acceptable limits for the metallic component.

In contrast, Figure 4.9(c) reveals that a total of 128 elements failed according to the Tsai–Wu criterion out of the 1,524,032 elements analysed during the rear triangle stiffness evaluation. These failed elements were subsequently imported back into Abaqus as a separate element set to enable clear visualization of their spatial distribution. As illustrated in Figure 4.13, the failed elements are concentrated at the joint region connecting the bottom bracket to the chain stay

tubes. This concentration of failure indices suggests a localized weakness in the transition region, which may arise due to the combined bending and shear stresses acting in this area. The interpretation of these results must, however, consider potential numerical sensitivities. The failed elements occur at a geometric transition where fillets are present, and stress singularities can sometimes exaggerate local values. Nonetheless, if this response reflects a true structural weakness rather than a numerical artefact, it highlights the need for design reinforcement at the chain stay–bottom bracket connection. Potential mitigation strategies could include enlarging the contact area at the joint or refining the geometry to reduce stress concentrations.

Additionally, the assessment of the rear dropout raises a secondary consideration. Although the stresses within the steel itself remain below critical levels, Figure 4.12 shows local deformation of 9.84mm on the rear dropout, close to the region where the wood and steel components are bonded. This observation suggests the possibility of debonding or stress transfer issues at the interface, which was not evaluated within the scope of this study. For future work, detailed analysis of the wood–steel bond strength and interface behaviour is recommended, as it may prove to be a limiting factor in the long-term performance of the hybrid frame.

4.1.4. Experimental and FEM Validation

The force displacement diagram for both the experimental and Finite element model was superimposed and can be seen as shown in Figure 4.14 and 4.15.

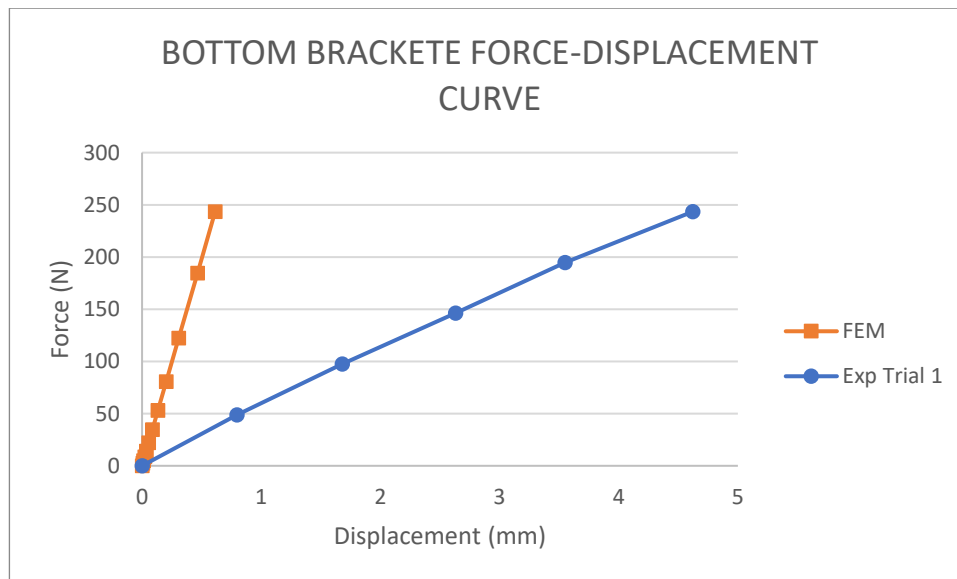


FIGURE 4.14: BOTTOM BRACKET EXPERIMENTAL AND FEM FORCE-DISPLACEMENT COMPARISM

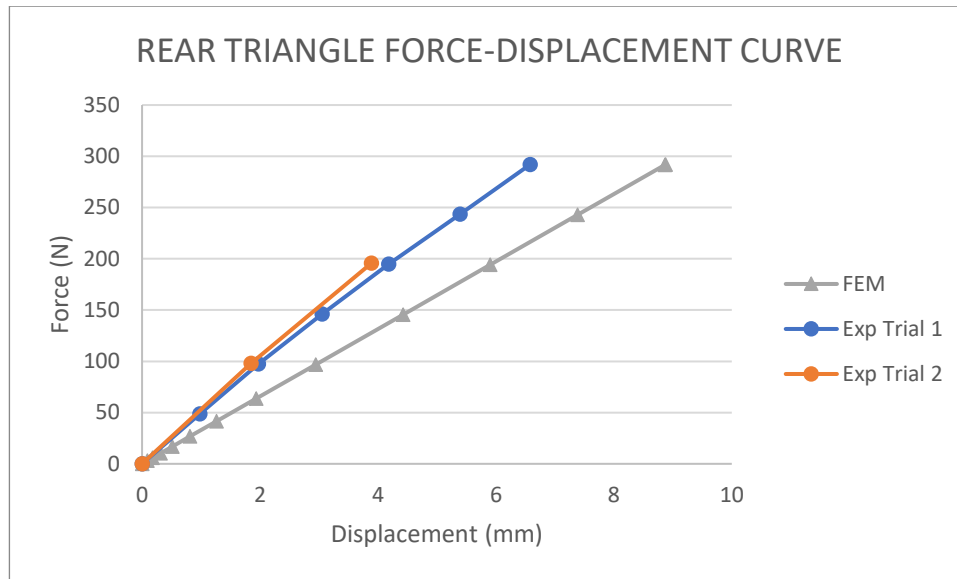


FIGURE 4.15: REAR TRIANGLE EXPERIMENTAL AND FEM FORCE-DISPLACEMENT COMPARISM

The FEM accurately captured linear elastic trends, but stiffness ranking diverged by location: at the bottom bracket, the FEM was stiffer than the experimental results ($\approx 4\text{--}5$ times), whereas at the rear triangle it was softer. This location-dependent bias can be said to be consistent with test–model boundary-condition differences and contact idealizations rather than bulk material error. The bottom-bracket simulation employed perfectly bonded contacts and rigid supports, eliminating possible clamp and bedding compliance that may be observed in the rig; conversely, the rear-triangle setup in FEM allowed more rotational freedom at the axle/seat interfaces than the physical fixture. Additional contributors include sensitivity to wood orthotropy orientation and the absence of local crushing/plasticity in clamped regions. This model can be further developed to better capture the reality of the experimental set-up.

4.2. Case Study 2: IMOCA Sandwich Specimens

4.2.1. Experimental Flexural Test (3-point and 4-Point) Results

Quasi-static three-point and four-point bending tests were carried out on plywood-core sandwich panels with carbon, basalt, and glass fibre skins, alongside unskinned plywood controls for reference. For each skin orientation (0° , 45° , and 90°), between six and eight specimens were tested to ensure statistical relevance. Due to time limitations, complementary tensile tests and full-field strain mapping with Digital Image Correlation (DIC) were not performed, and consequently no data were obtained for 45° sandwich specimens. The results

obtained are summarized in Figure 4.16-4.19, with the corresponding values presented in Table 13 also the post failure outcome of the specimen can be seen in Figure 4.20. The coefficient of variation (COV) is also reported for each case, expressed in percentage and enclosed in parentheses.

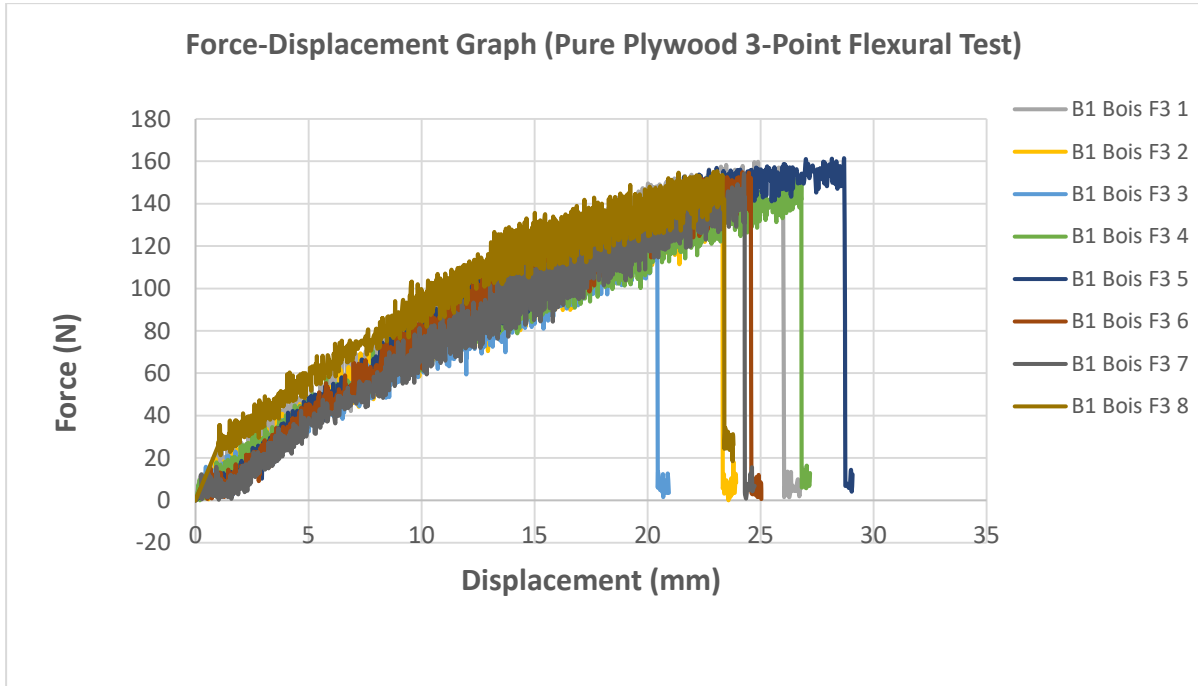


FIGURE 4.16: FORCE-DISPLACEMENT GRAPH FOR PURE PLYWOOD UNDER A 3-POINT FLEXURAL TEST

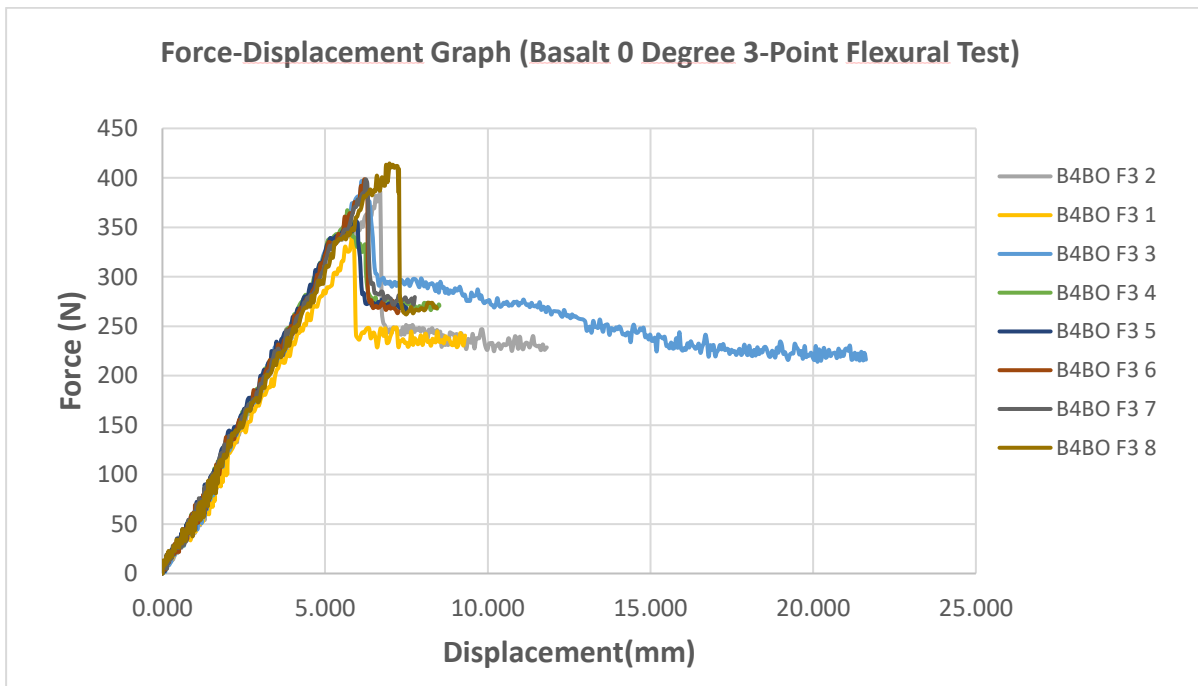


FIGURE 4.17: FORCE-DISPLACEMENT GRAPH FOR BASALT 0 DEGREE UNDER A 3-POINT FLEXURAL TEST

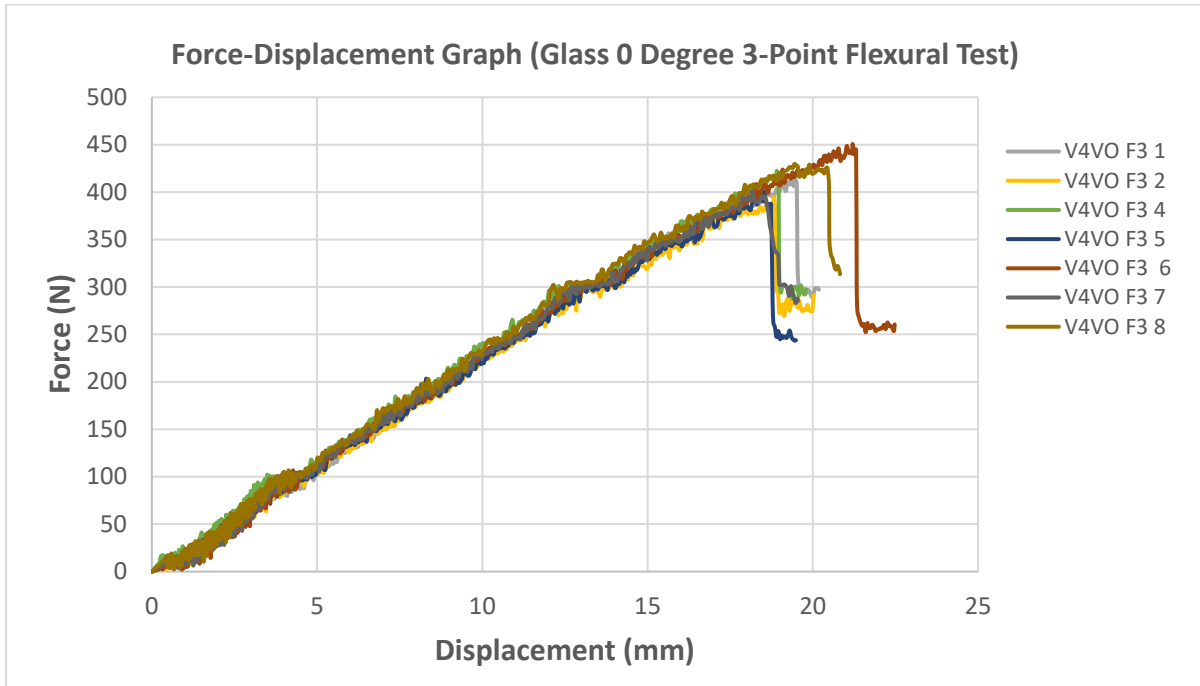


FIGURE 4.18: FORCE-DISPLACEMENT GRAPH FOR GLASS 0 DEGREE UNDER A 3-POINT FLEXURAL TEST

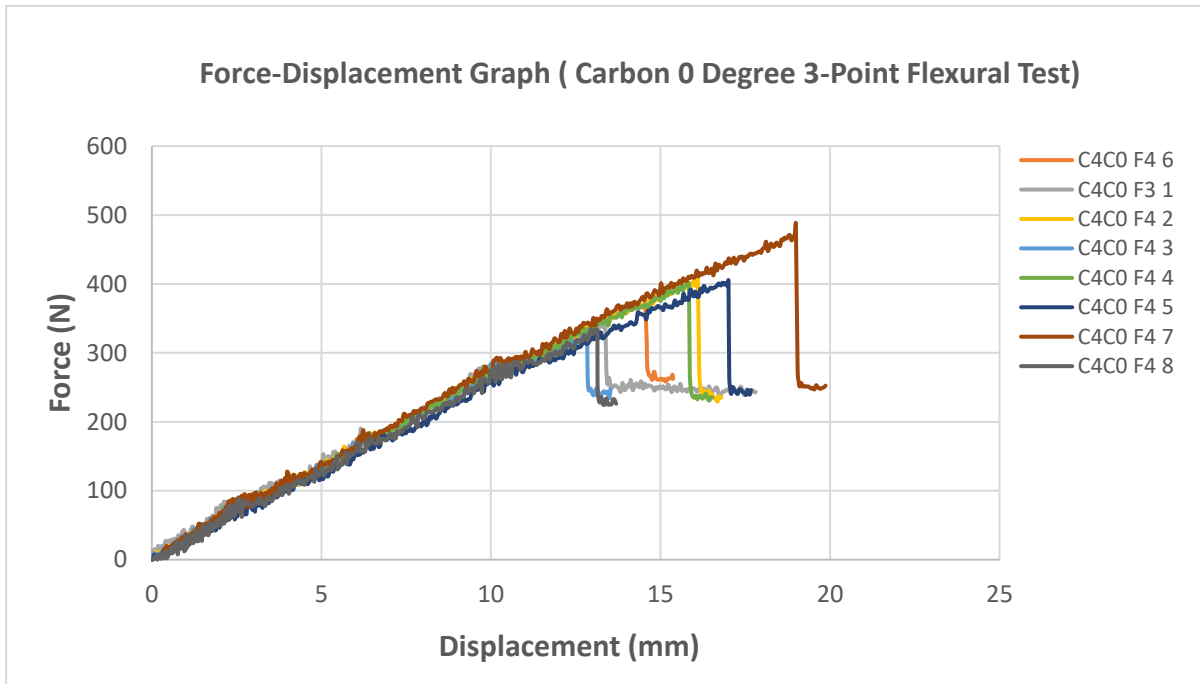


FIGURE 4.19: FORCE-DISPLACEMENT GRAPH FOR CARBON 0 DEGREE UNDER A 3-POINT FLEXURAL TEST

TABLE 13: SUMMARY OF STRESSES COMPUTATION RESULTS FOR SPECIMEN GROUP OF 0 DEGREE, 3-POINT AND THE COV(IN %)

	Control Plywood	Basalt Face-Sheet	Glass Face-Sheet	Carbon Face-Sheet
$P_{max(avg)}(N)$	151.77 (7%)	382.26 (7%)	416.13 (5%)	386.46 (13%)
$\delta_{max(avg)}$ (mm)	24.20 (10%)	6.21 (7%)	19.22 (5%)	15.20 (14%)
$\sigma_{max}(MPa)$	63.95	355.60	378.82	375.66
$\tau_{Core}(MPa)$	-	1.14	1.21	1.20

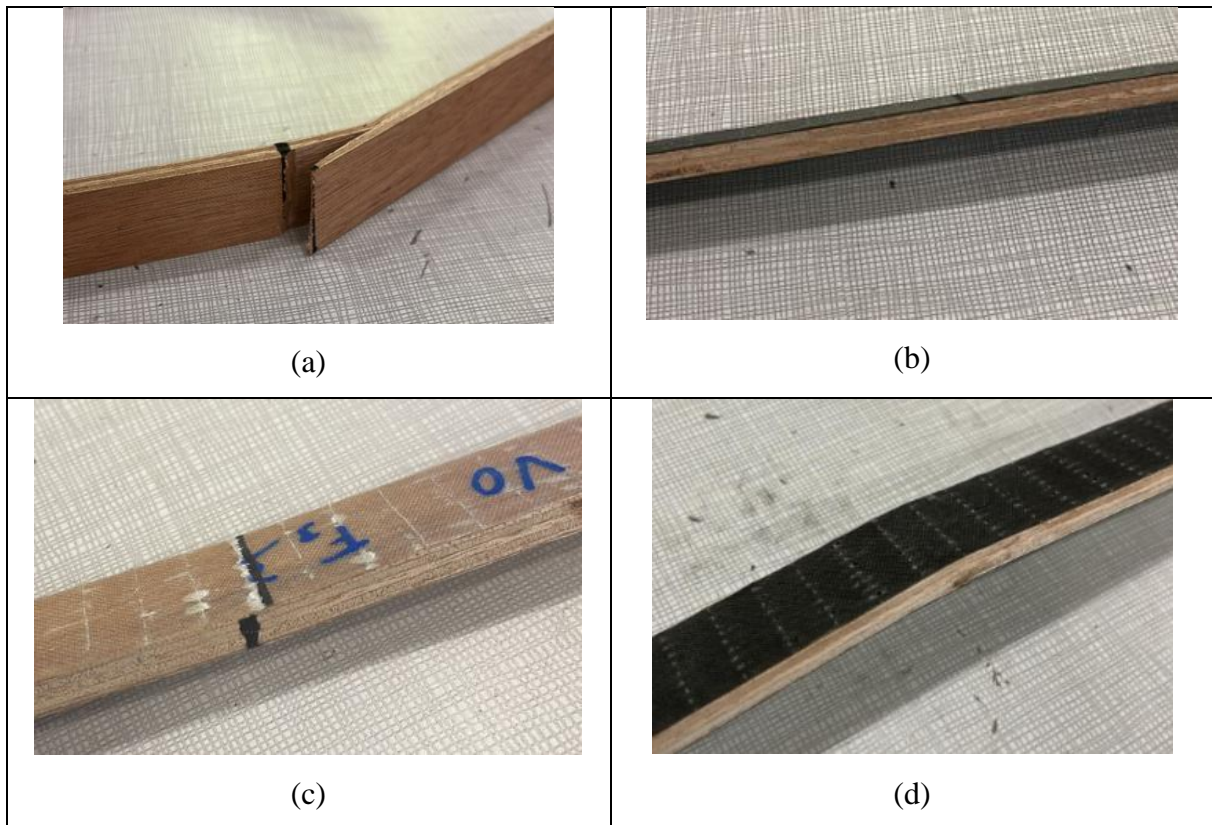


FIGURE 4.20: 3-POINT FLEXURAL AFTER TEST IMAGE OF SPECIMENS : (A) PURE PLYWOOD (B) BASALT FACE-SHEET 0 DEGREE (C) GLASS FACE-SHEET 0 DEGREE (D) CARBON FACE-SHEET 0 DEGREE

The quasi-static bending results presented in Table 13 highlight clear improvements in load-bearing capacity and stress resistance when plywood is reinforced with fibre skins compared to the unskinned control. The maximum load (P_{max}) carried by the control plywood averaged 151.77 N, whereas the skinned sandwiches achieved values between 382.26 N and 416.13 N. This represents more than a twofold increase in load capacity, confirming the significant

contribution of the fibre face-sheets to global bending resistance. Among the skins, glass fibre achieved the highest average load capacity (416.13 N, COV = 5%), slightly outperforming basalt (382.26 N, COV = 7%) and carbon (386.46 N, COV = 13%). The higher variability observed for carbon suggests a less consistent bonding or defect sensitivity in the tested series. Deflection values (δ_{max}) further distinguish the face-sheet types. The control plywood reached a much higher deflection of 24.20 mm, reflecting its lower stiffness and greater ductility. In contrast, basalt-faced specimens were markedly stiffer, failing at only 6.21 mm deflection. Glass and carbon specimens displayed intermediate behaviours, failing at 19.22 mm and 15.20 mm respectively. These trends reveal a trade-off between stiffness and deformability: basalt face-sheets maximized stiffness but failed in a more brittle manner, while glass and carbon allowed higher deformation before failure, potentially absorbing more energy under service loading.

In terms of calculated stresses, the maximum bending stress (σ_{max}) followed a similar trend, with glass (378.82 MPa) slightly outperforming carbon (375.66 MPa) and basalt (355.60 MPa). All reinforced specimens greatly exceeded the control plywood (63.95 MPa), confirming the decisive strengthening effect of the composite skins. Core shear stresses (τ_{core}) were broadly similar across the three reinforced cases (1.14–1.21 MPa), indicating that the plywood core was consistently engaged in shear transfer regardless of the outer face-sheet type.

Figure 4.20 presents the post-failure condition of the sandwich specimens after quasi-static bending. The control plywood, which lacked fibre face-sheets, failed in a typical manner within the tension zone, consistent with its lower strength and ductility. In contrast, the reinforced specimens with basalt, glass, and carbon skins exhibited no significant macroscopic deformation, indicating that the skins effectively constrained bending failure. Notably, the specimen with glass face-sheets displayed a distinct white patch along the radius of the applied load. This feature suggests the development of localized stress concentrations within the compression zone, which may be linked to incipient core crushing beneath the loading nose. Such behaviour is characteristic of sandwich structures where the stiff face-sheets protect against tensile rupture, but load transfer into the plywood core introduces a secondary failure mode through localized compressive damage.

Next is the 4-point flexural testing and the images is as shown in Figure 4.21-4.24.

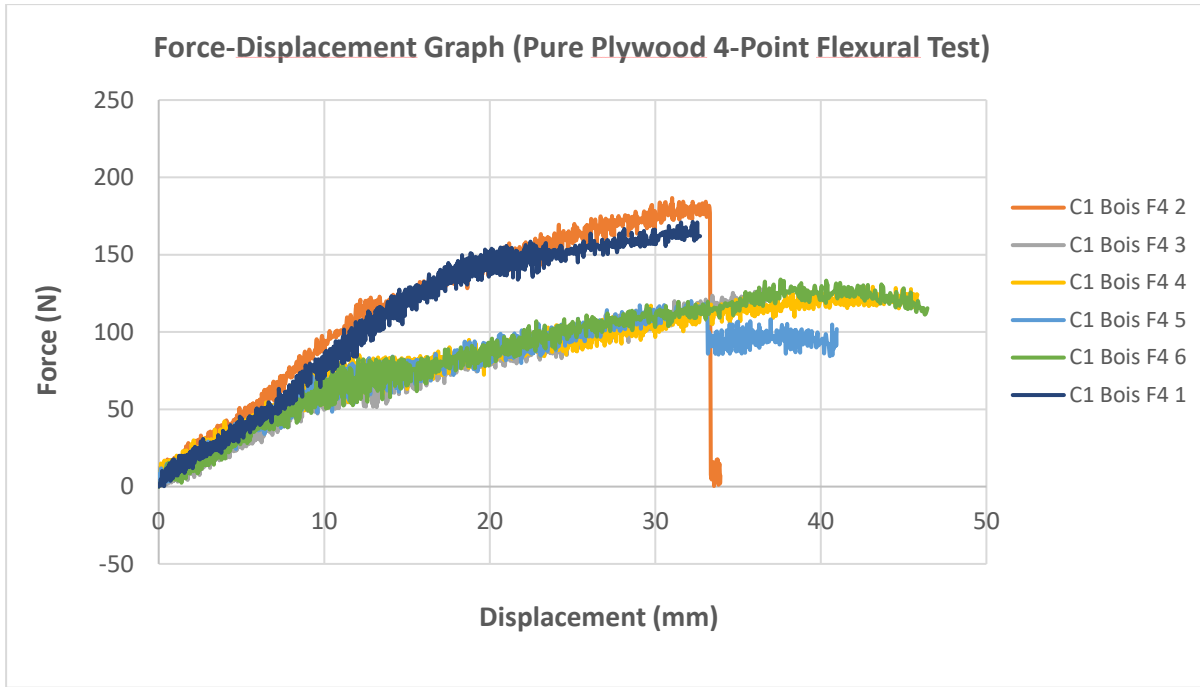


FIGURE 4.21: FORCE-DISPLACEMENT GRAPH FOR PURE PLYWOOD UNDER A 4-POINT FLEXURAL TEST

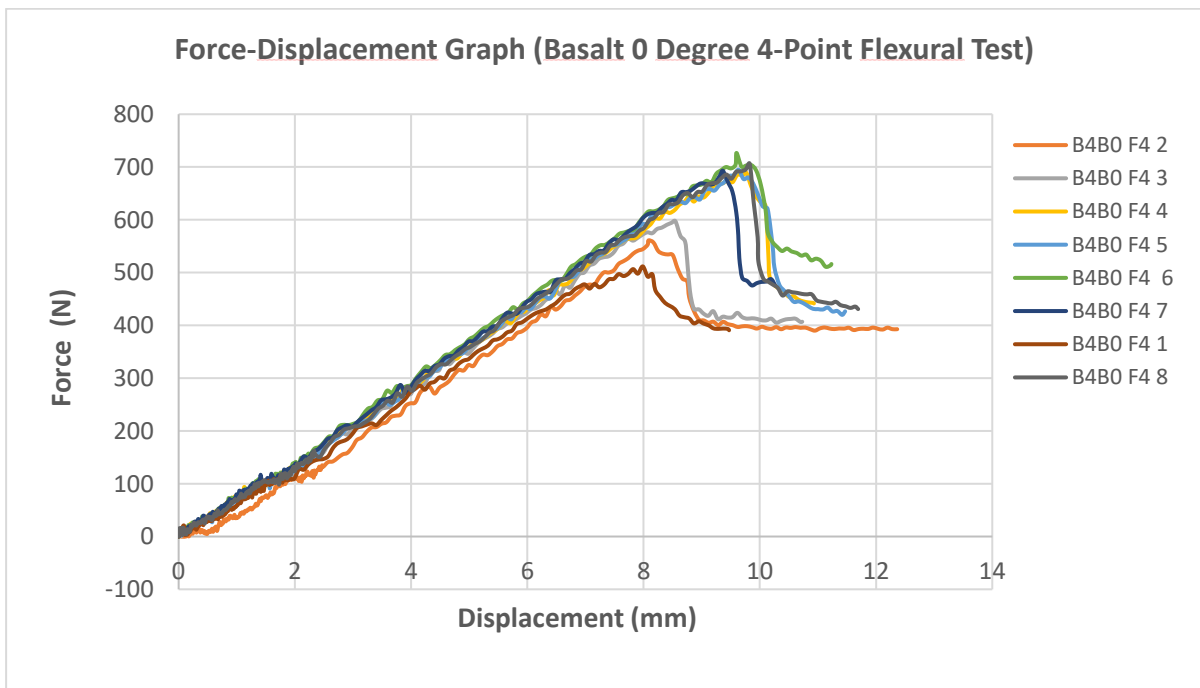


FIGURE 4.22: FORCE-DISPLACEMENT GRAPH FOR BASALT 0 DEGREE UNDER A 4-POINT FLEXURAL TEST

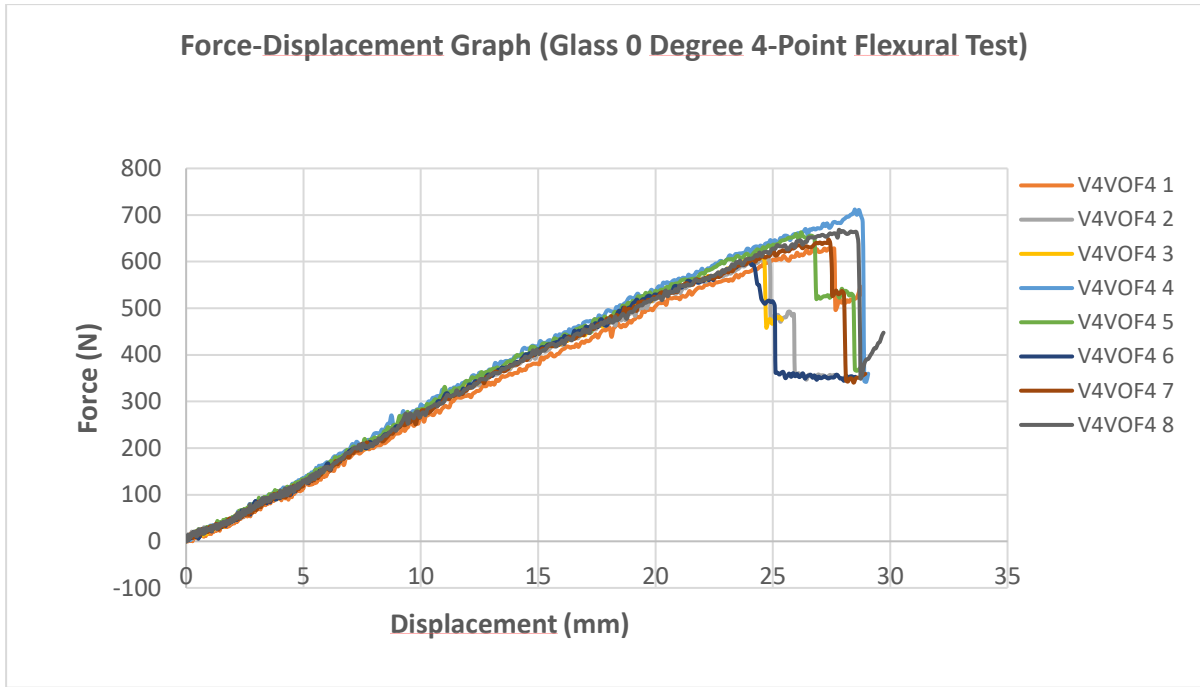


FIGURE 4.23: FORCE-DISPLACEMENT GRAPH FOR GLASS 0 DEGREE UNDER A 4-POINT FLEXURAL TEST

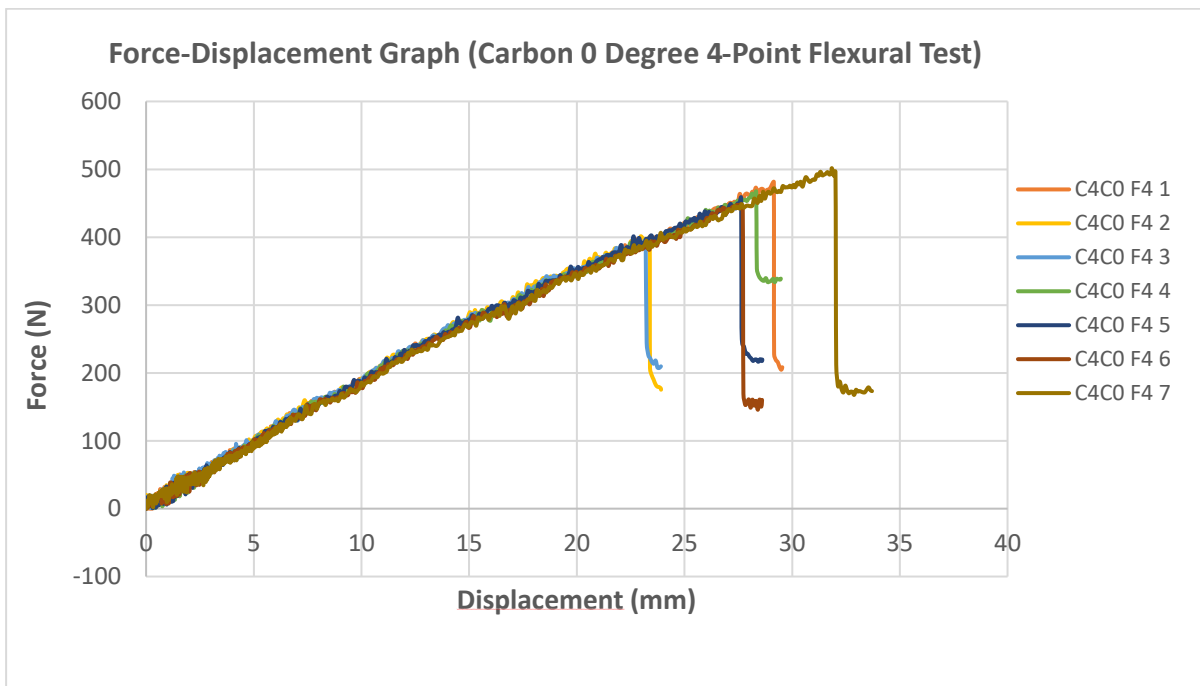


FIGURE 4.24: FORCE-DISPLACEMENT GRAPH FOR CARBON 0 DEGREE UNDER A 4-POINT FLEXURAL TEST

TABLE 14: SUMMARY OF STRESSES COMPUTATION RESULTS FOR SPECIMEN GROUP OF 0 DEGREE, 4-POINT AND THE COV(IN %)

	Control Plywood	Basalt Face-Sheet	Glass Face-Sheet	Carbon Face-Sheet
$P_{max}(avg)(N)$	144.88 (19%)	647.47 (12%)	644.20 (6%)	450.82 (6%)
$\delta_{max}(avg)$ (mm)	35.40 (13%)	8.00 (39%)	26.30 (7%)	27.25 (12%)
$\sigma_{max}(MPa)$	34.71	359.76	345.57	269.28
$\tau_{Core}(MPa)$	-	1.92	1.84	1.44



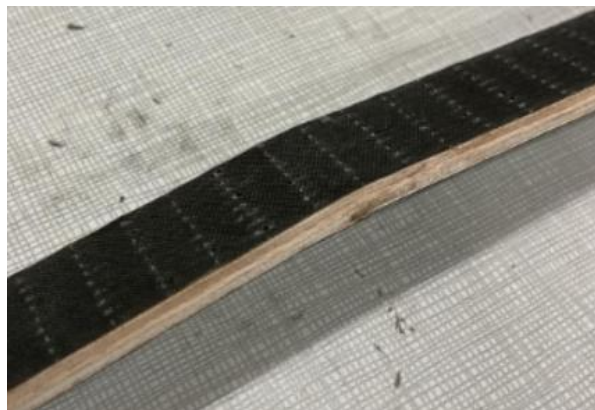
(a)



(b)



(c)



(d)

FIGURE 4.25: 4-POINT FLEXURAL AFTER TEST IMAGE OF SPECIMENS : (A) PURE PLYWOOD (B) BASALT FACE-SHEET 0 DEGREE (C) GLASS FACE-SHEET 0 DEGREE (D) CARBON FACE-SHEET 0 DEGREE

The four-point bending results presented in Figure 4.21-4.24 and Table 14 reinforce the performance trends already identified under three-point loading. As with the earlier tests, the addition of fibre face-sheets produced a substantial increase in the maximum load capacity compared to the control plywood, which reached only 144.88 N. Both basalt and glass face-

sheeted specimens carried more than four times this load, achieving 647.47 N and 644.20 N, respectively. The carbon-skinned sandwiches also showed a notable improvement at 450.82 N, although their performance remained below that of basalt and glass.

While the ranking of face-sheet materials is similar to the three-point case, the absolute deflection patterns reveal some distinctions. The control plywood again exhibited the largest deformation (35.40 mm), reflecting its lower stiffness. The basalt specimens, consistent with their stiff behaviour in three-point bending, failed at a much lower deflection of 8.00 mm, indicating a brittle mode of failure under distributed loading. By contrast, the glass and carbon skins allowed larger deflections of 26.30 mm and 27.25 mm, respectively, which suggests a greater capacity for energy absorption prior to failure compared to basalt.

Stress calculations further underline these observations. The highest maximum stresses were recorded for basalt (359.76 MPa) and glass (345.57 MPa), both an order of magnitude greater than the control (34.71 MPa). The carbon face-sheets followed at 269.28 MPa, maintaining the same relative ranking observed under three-point loading. The shear stress within the plywood core remained relatively consistent across reinforced specimens, with values between 1.44 and 1.92 MPa, again confirming that the core response is less sensitive to the skin type than the bending strength.

The post-failure images of the four-point bending specimens, shown in Figure 4.25, confirm observations made during the three-point bending tests. The control plywood Figure 4.25 (a) exhibited visible deformation and cracking along the tension zone, characteristic of its lower resistance and lack of skin reinforcement. In contrast, both the basalt 4.25 (b) and carbon 4.25 (d) face-sheeted sandwiches displayed no significant observable external damage, reflecting the ability of the fibre skins to constrain failure and prevent macroscopic bending deformations. The only reinforced specimen to exhibit a visible response was the glass face-sheet sandwich 4.25 (c), where a localized patch beneath the load line suggested stress concentration and possible onset of core crushing in the compression zone.

Overall, the after-failure images from both three-point and four-point tests of specimens with 0-degree reinforced laminate consistently demonstrate that plywood controls fail visibly in tension, while basalt, glass and carbon face-sheeted sandwiches maintain structural integrity without clear surface indications of failure aside the glass. Glass face-sheets provide high strength but show localized compression-related markings, which may represent a critical mode of damage initiation.

Subsequently, the experimental results for specimens with laminate face-sheets oriented at 90° were also obtained. These outcomes are presented for the three-point bending tests in Figures 4.26 to 4.28.

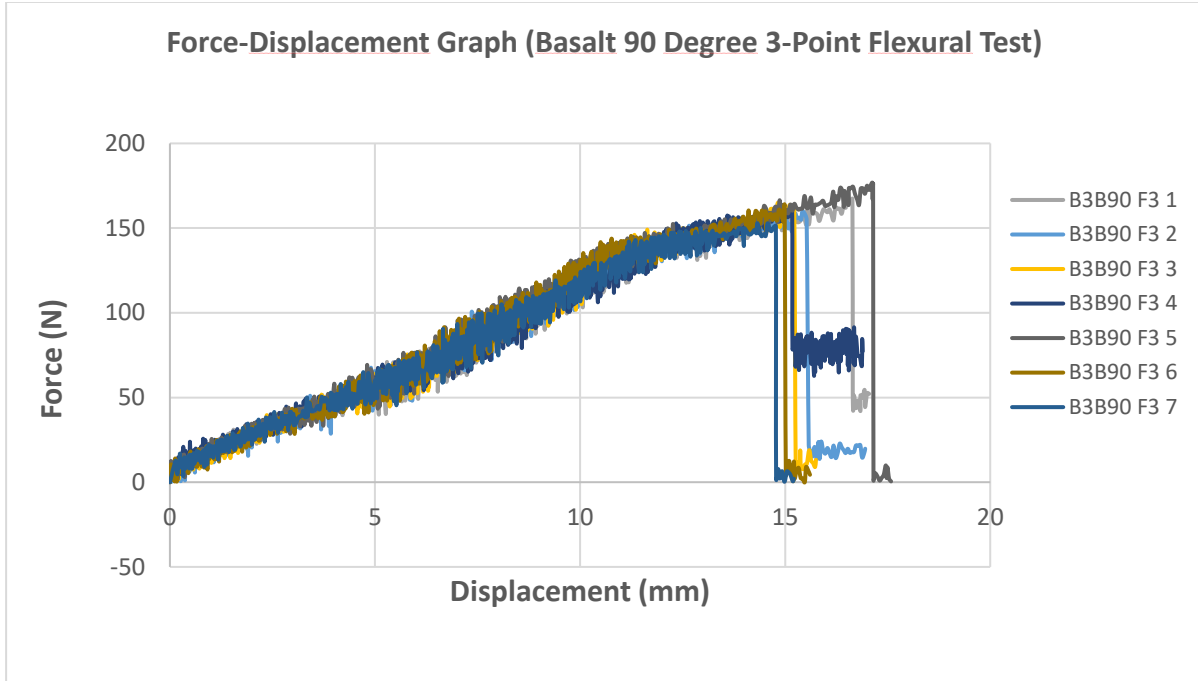


FIGURE 4.26: FORCE-DISPLACEMENT GRAPH FOR BASALT 90 DEGREE UNDER A 3-POINT FLEXURAL TEST

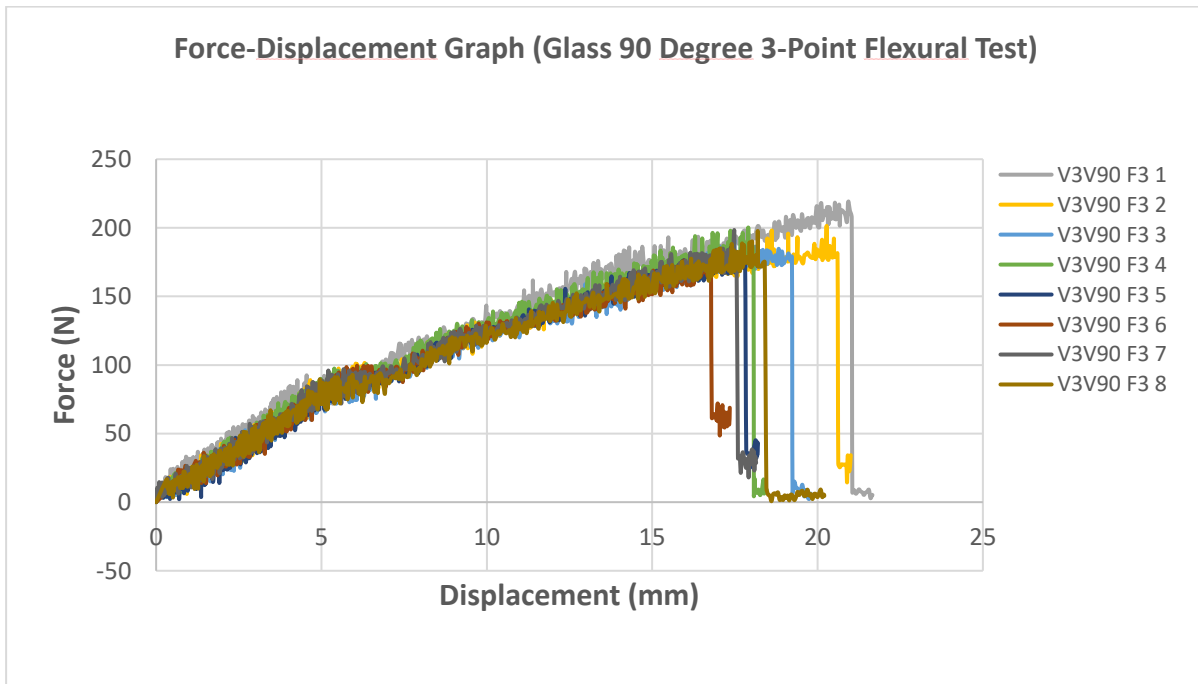


FIGURE 4.27: FORCE-DISPLACEMENT GRAPH FOR GLASS 90 DEGREE UNDER A 3-POINT FLEXURAL TEST

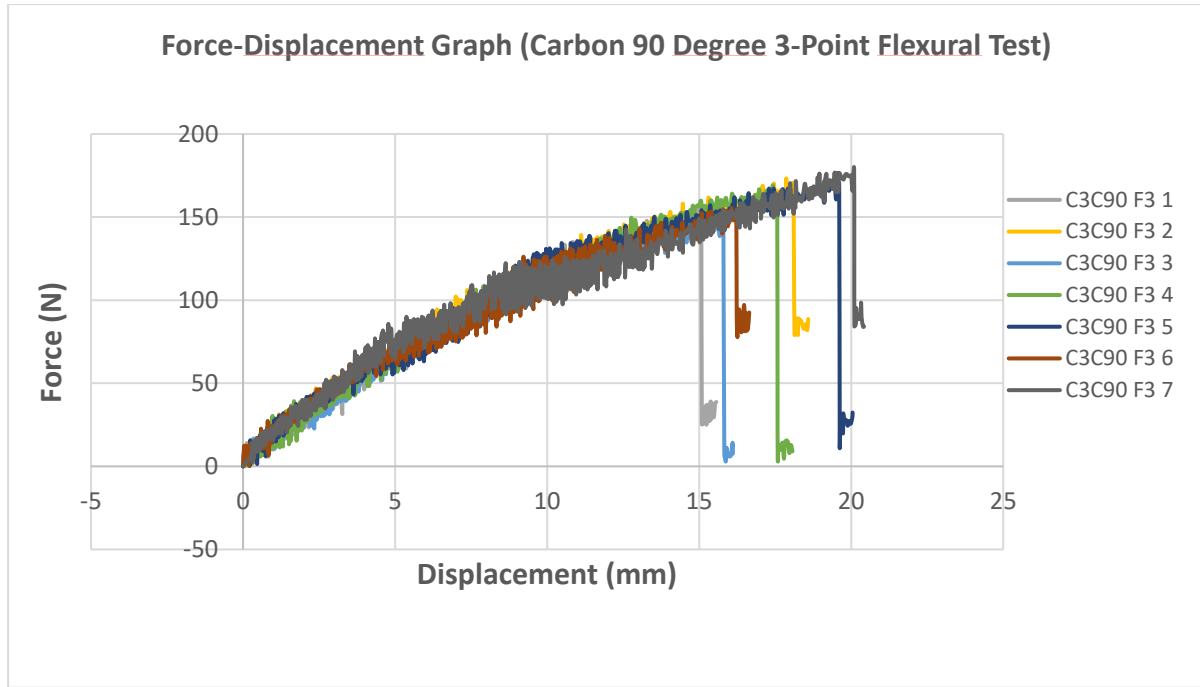


FIGURE 4.28: FORCE-DISPLACEMENT GRAPH FOR CARBON 90 DEGREE UNDER A 3-POINT FLEXURAL TEST

TABLE 15: SUMMARY OF STRESSES COMPUTATION RESULTS FOR SPECIMEN GROUP OF 90 DEGREE, 3-POINT AND THE COV(IN %)

	Control Plywood	Basalt Face-Sheet	Glass Face-Sheet	Carbon Face-Sheet
$P_{\max(\text{avg})}$ (N)	151.77 (7%)	164.17 (5%)	197.12 (7%)	166.93 (6%)
$\delta_{\max(\text{avg})}$ (mm)	24.20 (10%)	15.47 (6%)	18.36 (9%)	17.37 (11%)
σ_{\max} (MPa)	63.95	148.42	179.62	161.43
τ_{Core} (MPa)	-	0.47	0.57	0.52

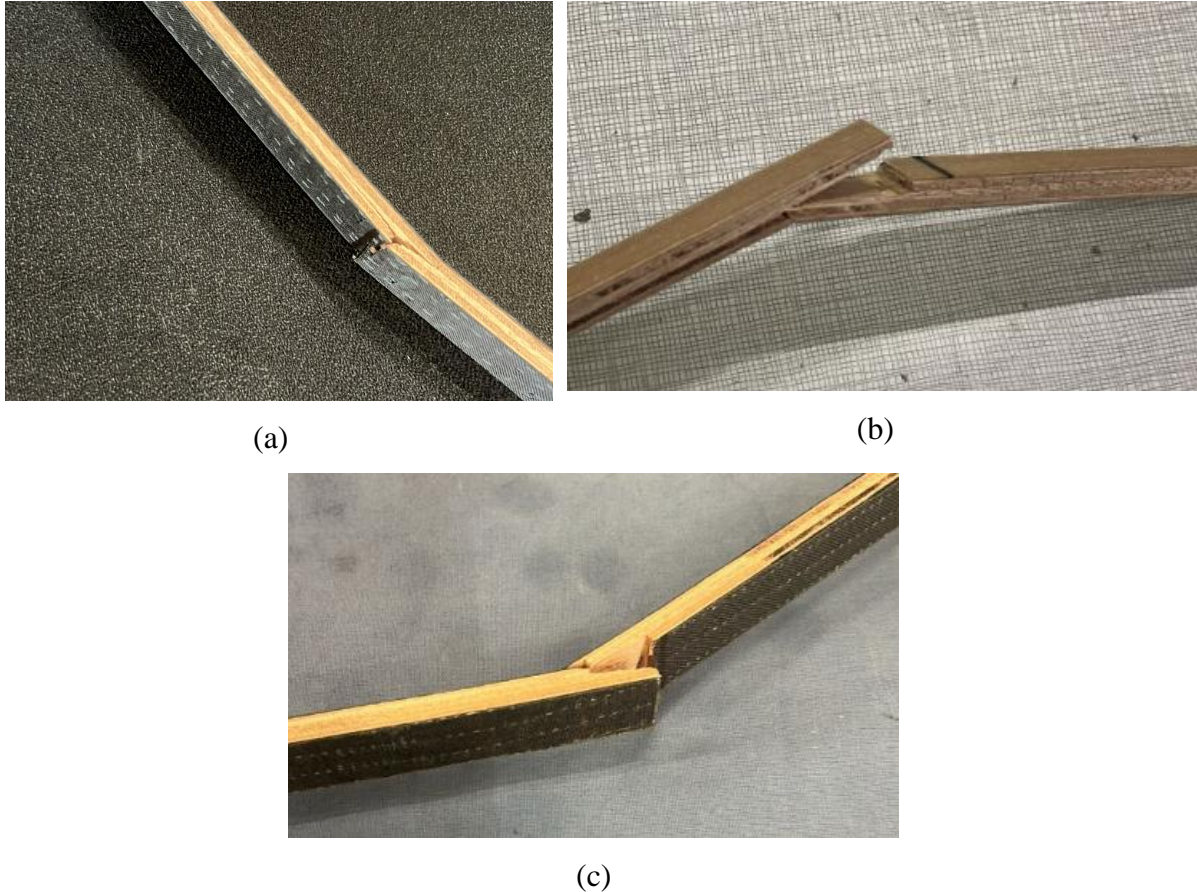


FIGURE 4.29: 3-POINT FLEXURAL AFTER TEST IMAGE OF SPECIMENS : (A) BASALT FACE-SHEET 90 DEGREE (B) GLASS FACE-SHEET 90 DEGREE (C) CARBON FACE-SHEET 90 DEGREE

Compared with the 0° three-point bending series, the 90° orientation retained the same control plywood baseline ($P_{max} = 151.77 \text{ N}$; $\delta_{max} = 24.20 \text{ mm}$), meaning that the observed differences can be attributed solely to the effect of the laminate face-sheets at this orientation. All of the reinforced laminates improved load capacity and reduced deflection compared with the control, although to varying extents as shown in Figures 4.26 to 4.28 also Table 15. In terms of maximum load, the basalt face-sheets carried 164.17 N , representing only a modest 8.0% increase relative to the control, whereas glass and carbon provided more substantial gains of 29.9% and 10.0% , respectively. The ranking of the materials therefore mirrored the trend already observed at 0° , with glass emerging as the strongest performer, though the absolute improvements were generally smaller at 90° , which is expected when fibres are aligned transversely to the span.

Deflection at failure (Table 15) also reflected these distinctions. The control plywood exhibited the largest deformation at 24.20 mm , while basalt, consistent with its stiff behaviour at 0° , showed the lowest deflection at 15.47 mm , corresponding to a 36% reduction. Carbon and glass followed with reductions of 28% and 24% , respectively. The calculated bending stresses

confirmed these findings. Glass achieved the highest stress capacity of 179.62 MPa, followed by carbon at 161.43 MPa and basalt at 148.42 MPa . Once again, the material ranking was consistent with the earlier 0° tests, with glass providing the greatest improvement in load capacity and carbon performing at an intermediate level. Basalt, although trailing in strength, offered the stiffest response. The shear stresses within the plywood core ranged between 0.45 and 0.57 MPa across the laminates, comparable to values from the 0° series, confirming that the core’s contribution in shear remained largely unaffected by face-sheet type and that the skins primarily governed bending behaviour.

From a cost–performance standpoint, the glass laminates delivered the most favourable outcome at 90°, combining the largest strength increase (+30%) with a moderate reduction in deflection (−24%) and low scatter, all at the lowest material cost. Basalt offered the advantage of maximum stiffness with a significant reduction in deflection (−36%), but the strength gain was marginal and accompanied by higher variability; it is therefore more suitable where deflection control is a priority, such as in regions prone to local buckling or dimensional tolerance issues. Carbon provided moderate gains in both capacity and stiffness. This makes the use of this different laminate difficult to justify at 90° unless dictated by weight constraints or material compatibility within a larger system.

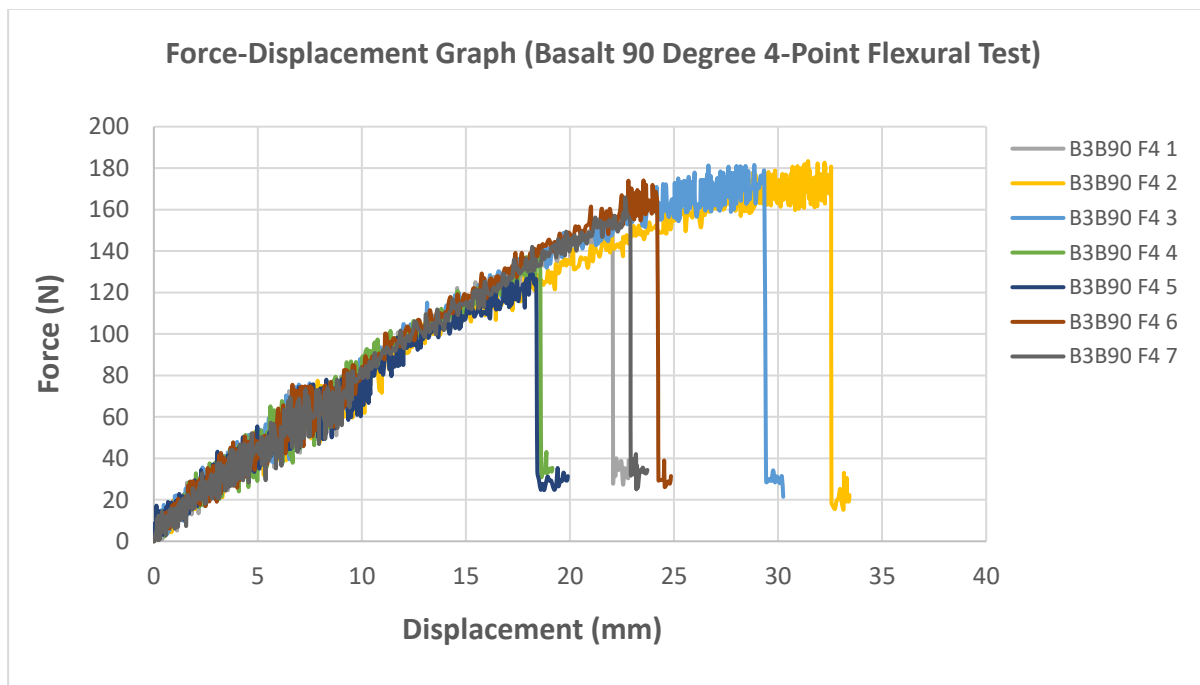


FIGURE 4.30: FORCE-DISPLACEMENT GRAPH FOR BASALT 90 DEGREE UNDER A 4-POINT FLEXURAL TEST

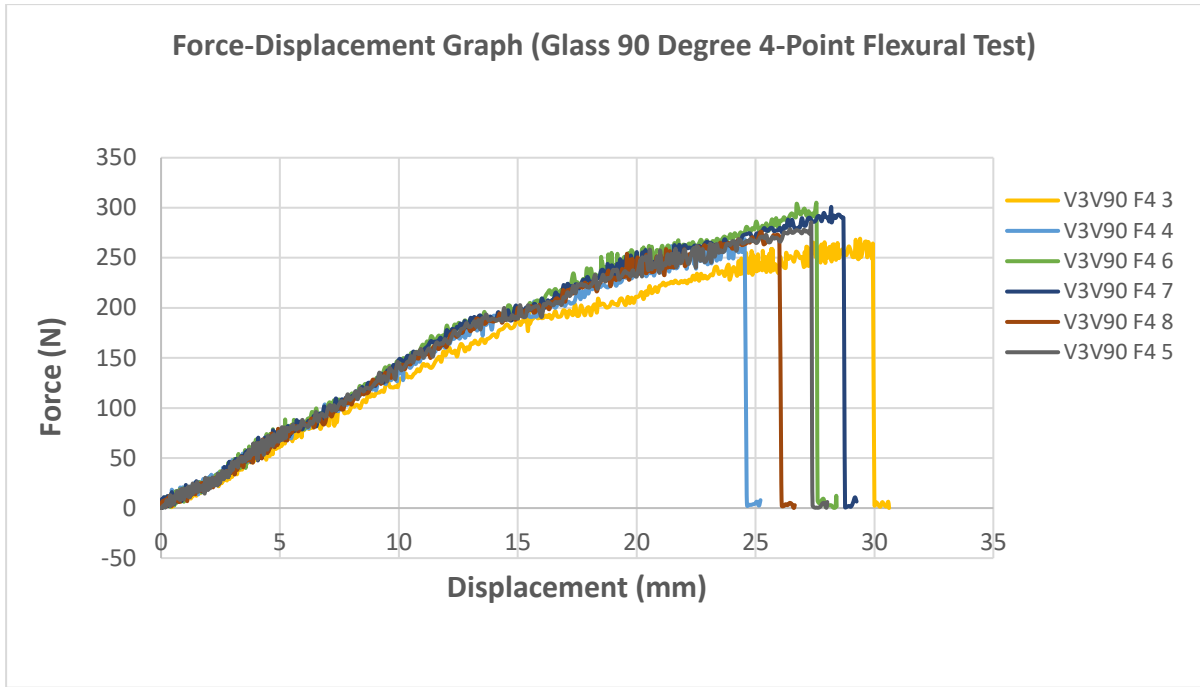


FIGURE 4.31: FORCE-DISPLACEMENT GRAPH FOR GLASS 90 DEGREE UNDER A 4-POINT FLEXURAL TEST

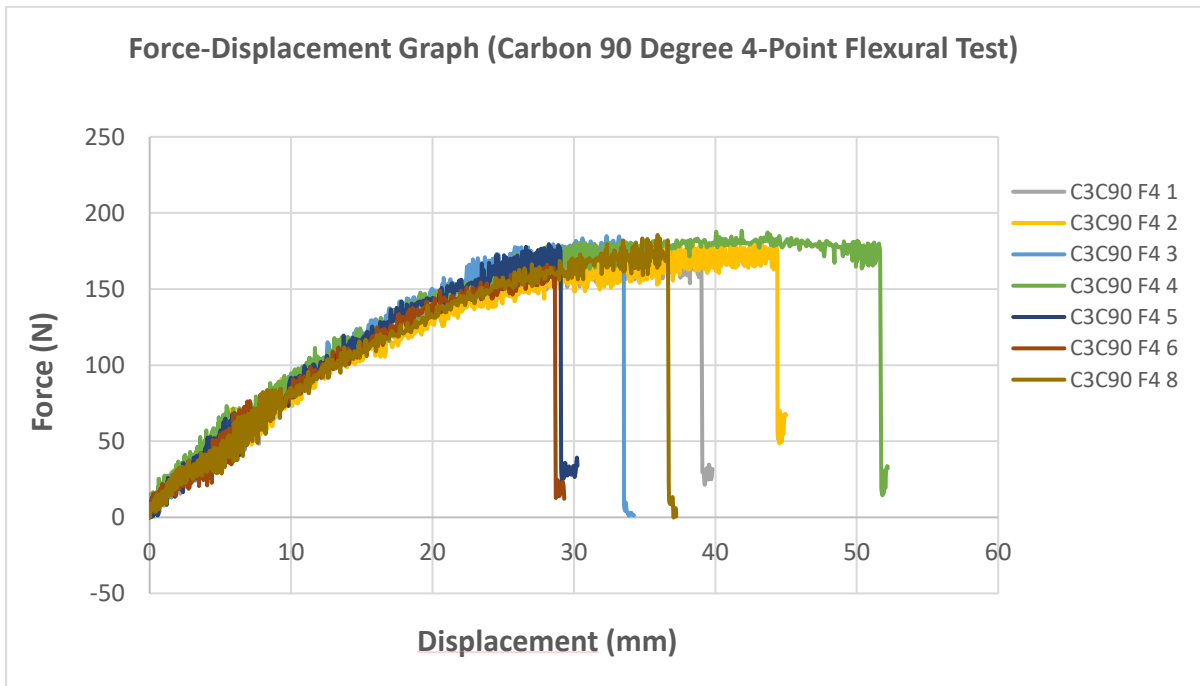


FIGURE 4.32: FORCE-DISPLACEMENT GRAPH FOR CARBON 90 DEGREE UNDER A 4-POINT FLEXURAL TEST

TABLE 16: SUMMARY OF STRESSES COMPUTATION RESULTS FOR SPECIMEN GROUP OF 90 DEGREE, 4-POINT AND THE COV(IN %)

	Control Plywood	Basalt Face-Sheet	Glass Face-Sheet	Carbon Face-Sheet
$P_{\max(\text{avg})}(\text{N})$	144.88 (19%)	166.37 (11%)	283.86 (5%)	180.64 (4%)
$\delta_{\max(\text{avg})}(\text{mm})$	35.40 (13%)	23.61 (21%)	26.91 (7%)	35.13 (17%)
$\sigma_{\max}(\text{MPa})$	34.71	80.28	150.85	104.61
$\tau_{\text{Core}}(\text{MPa})$	-	0.43	0.80	0.56

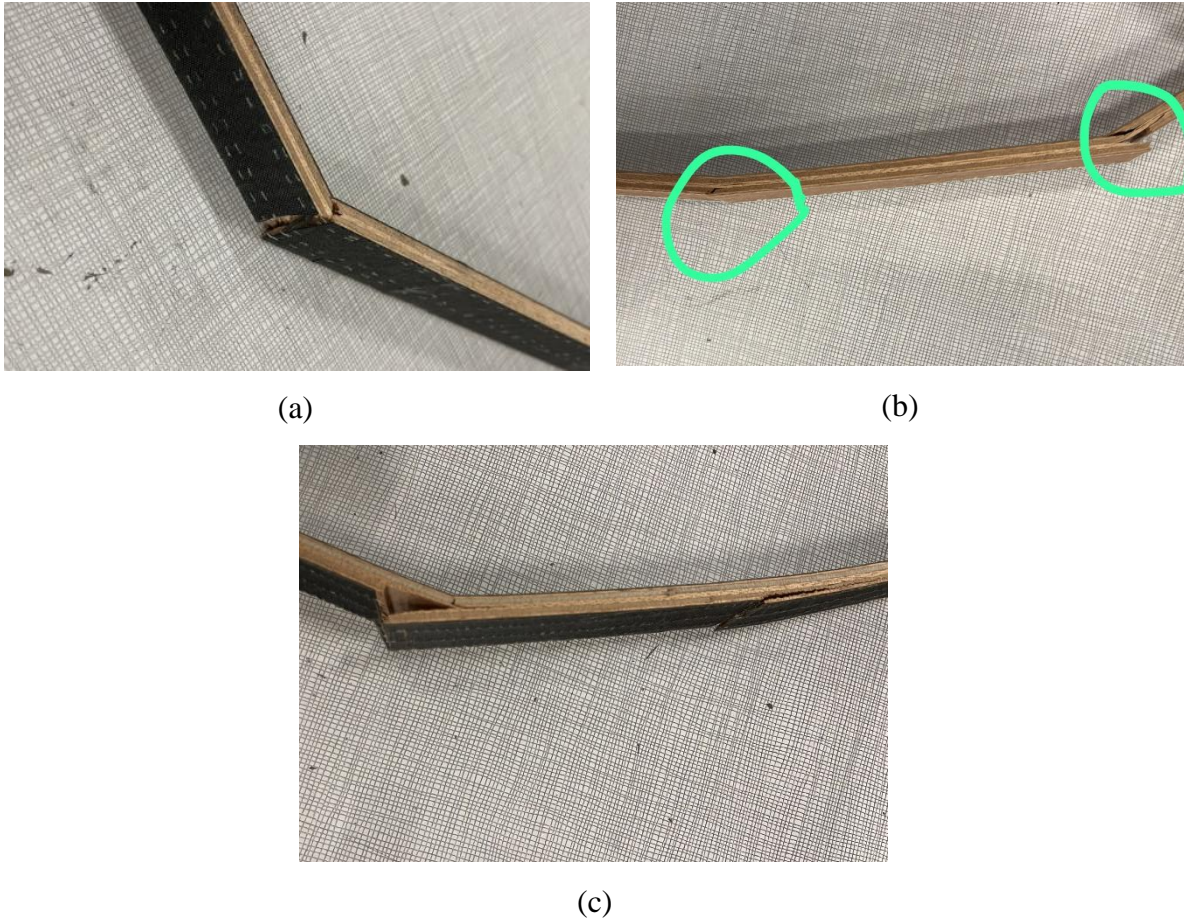


FIGURE 4.33: 4-POINT FLEXURAL AFTER TEST IMAGE OF SPECIMENS : (A) BASALT FACE-SHEET 90 DEGREE (B) GLASS FACE-SHEET 90 DEGREE (C) CARBON FACE-SHEET 90 DEGREE

The results of the 90° four-point bending tests, summarized in Figure 4.30-4.32 and Table 16, further demonstrate the influence of laminate face-sheets under transverse orientation.

As in the three-point tests, the control plywood baseline remained unchanged ($P_{max} = 144.88$ N; $\delta_{max} = 35.40$ mm), allowing a direct comparison of the effects of the face-sheets at 90° . The reinforced specimens clearly improved load capacity, although the relative magnitude of these improvements varied significantly with material choice. Glass fibre provided the largest increase in maximum load, reaching 283.86 N, which represents a 96% gain over the control. Carbon face-sheets followed with 180.64 N (+25%), while basalt laminates showed only a modest rise to 166.37 N (+15%). This ranking is consistent with the three-point 90° results, where glass also offered the highest relative strength enhancement, carbon was intermediate, and basalt showed the least pronounced benefit.

In terms of deflection, the control plywood again deformed most substantially (35.40 mm), confirming its low stiffness and ductility. Basalt reinforcement reduced this value to 23.61 mm (−33% vs control), indicating its role in providing a stiffer structural response. Glass and carbon, however, displayed higher deflections of 26.91 mm (−24%) and 35.13 mm (−1%), respectively. While glass offered the greatest strength increase, its deflection remained relatively close to the control, suggesting a more balanced but less stiff response compared to basalt. Carbon, despite increasing load capacity, essentially mirrored the ductile behaviour of the control, which may limit its suitability when stiffness is a primary design criterion.

The calculated bending stresses (σ_{max}) followed similar trends. Glass achieved the highest stress capacity at 150.85 MPa, more than four times the control (34.71 MPa), while carbon reached 104.61 MPa (+200%) and basalt 80.28 MPa (+131%). These results confirm that glass face-sheets deliver the greatest structural benefit under transverse loading, whereas basalt contributes more modestly to strength but remains valuable for controlling deformation. The measured core shear stresses were 0.43 MPa for basalt, 0.80 MPa for glass, and 0.56 MPa for carbon. These values are broadly comparable to those seen in the three-point series, reinforcing the conclusion that the plywood core carries a consistent shear contribution, largely independent of skin material.

Overall, the four-point 90° tests support and extend the conclusions drawn from the three-point experiments. The consistency in ranking across both methods—glass as the most effective reinforcement, carbon intermediate, and basalt the least effective in strength but stiffest, adds confidence to these trends. Importantly, the larger constant moment region of the four-point setup highlights more clearly the trade-off between strength and stiffness. Glass emerges as the most efficient choice when strength enhancement is prioritised, delivering nearly double the capacity of the control with acceptable variability (COV = 5%). Basalt remains valuable for stiffness-driven applications, reducing deflection by one-third even if the strength gains are

modest. Carbon, while effective in increasing capacity, shows limited stiffness improvement at 90° and comes with higher cost, making it less competitive in this orientation unless specific weight or compatibility constraints justify its use.

4.2.2. FEM Predictions and Comparison

A preliminary FEM model was developed to compare with the experimental response; however, due to limited information on the exact material composition and properties of the sandwich panels, the model could not fully capture the measured force–displacement behaviour (see Figure 4.34).

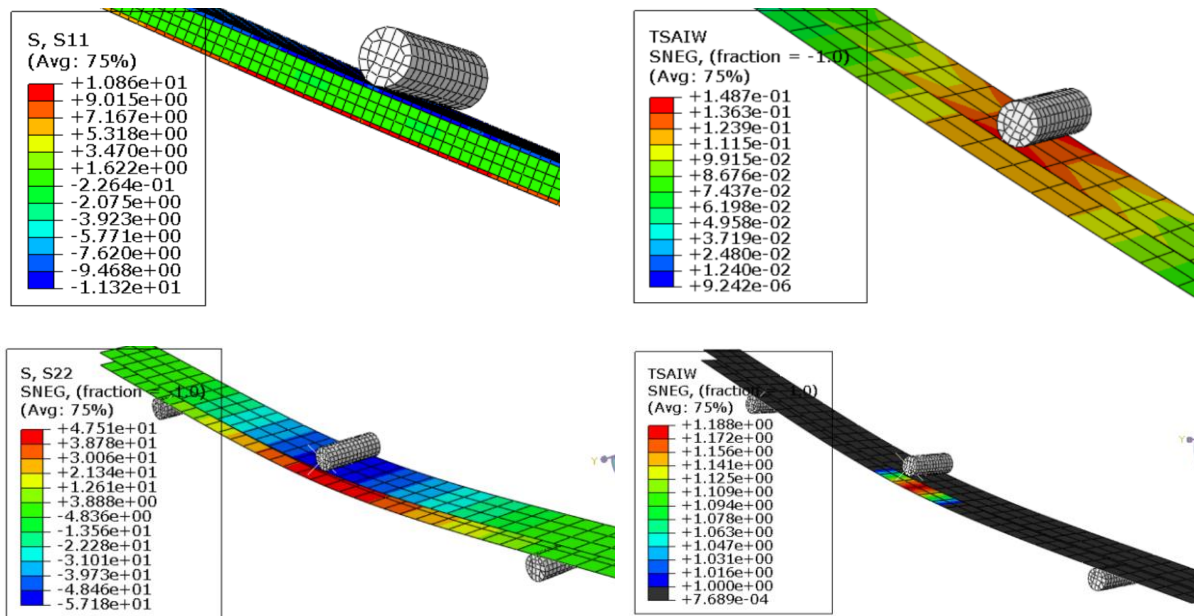


FIGURE 4.34: FEM SIMULATION FOR SANDWICH SPECIMEN (A) 0-DEGREE (B) 90-DEGREE

THIS PAGE WAS INTENTIONALLY LEFT BLANK

5. CONCLUSIONS AND FURTHER DEVELOPMENTS

5.1. Main conclusions

This thesis investigated the structural performance of wooden systems for sustainable means of transport. Two case studies were examined in detail: a full-scale solid oak bicycle frame and plywood-core sandwich specimens inspired by IMOCA hull structures. Both experimental testing and finite element modelling were employed, supported by custom failure evaluation methods. The key conclusions are summarised below.

5.1.1. Wooden bicycle frame

Experimental stiffness tests on the oak bicycle frame showed that wood can be used as a structural material for bicycles with adequate stiffness and safety margins under static loading. The load–displacement responses for bottom bracket and rear triangle were linear and remained within the elastic range of oak, with small global deflections. Finite element modelling, enhanced with a Python-based Tsai–Wu failure post-processor, confirmed the absence of global failure in the wooden components. It also identified localised stress concentrations at the transitions between the rear triangle and the steel–wood dropout interfaces. While these findings establish the feasibility of using oak for bicycle frames, they also highlight the importance of careful detailing at joints and hybrid interfaces to mitigate localised weaknesses.

5.1.2. IMOCA sandwich specimens

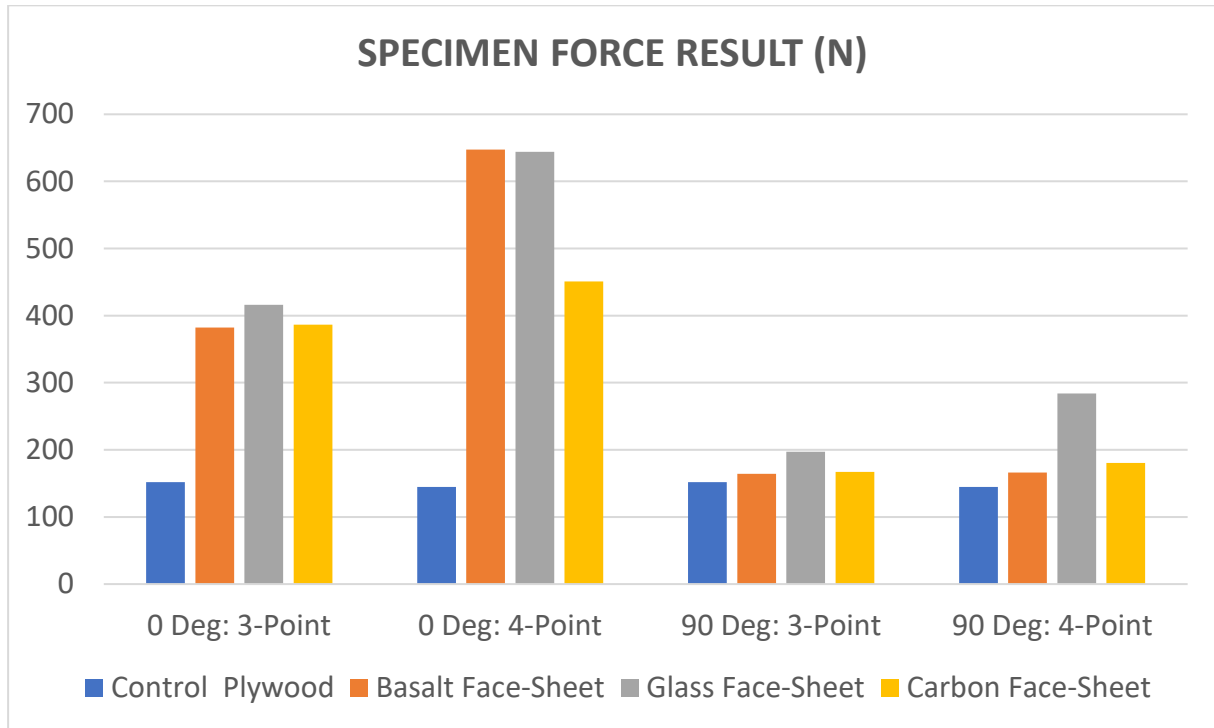


FIGURE 5.1: SUMMARY OF MAXIMUM FORCE CAPACITY FOR EACH SANDWICH SPECIMEN

Quasi-static bending tests on plywood-core sandwich panels reinforced with carbon, basalt and glass face sheets confirmed significant performance improvements relative to the unreinforced control panels. At a 0° orientation (see Figure 5.1), both basalt and carbon enhanced strength and stiffness; however, basalt consistently outperformed carbon in terms of stiffness and strength under four-point bending. At 90°, the absolute gains were smaller, but glass fibre provided the greatest increase in strength with low variability. Basalt again delivered superior stiffness. Carbon remained an intermediate performer, but became less attractive when cost was considered. Overall, glass fibre emerged as the most advantageous reinforcement strategy; basalt proved ideal for stiffness-critical zones; and carbon was suitable only for niche applications where weight or compatibility considerations dominated.

5.1.3. General outcomes

Combining the results of both studies shows that wood can be effectively engineered as a solid frame material or the core of a sandwich system for high-performance applications in sustainable transport. The bicycle frame study confirmed that solid oak is a viable structural option, and the IMOCA sandwich study showed the benefits of hybrid wood-composite

designs. Together, the studies confirm the potential of wooden structures as a credible alternative to metals and synthetic composites for lightweight, sustainable mobility.

5.2. Further developments

Future work on the wooden bicycle frame should concentrate on several key areas. Particular attention is required at the junctions between the wooden and steel components, as these hybrid connection points influence both load transfer and long-term durability. Additionally, extended fatigue and creep testing is necessary to evaluate the behaviour of the solid wooden frame under cyclic loading and sustained service conditions. This will provide essential data for assessing safety and design life. Finally, developing refined anisotropic failure models tailored to solid wood would significantly improve the predictive accuracy of finite element simulations, enabling better optimisation of frame geometry and material utilisation.

Further research on bond integrity and interfacial performance between the plywood core and the composite skins is recommended for the IMOCA sandwich panels, especially given the harsh marine environment in which they are used, where moisture ingress, salt exposure and cyclic stresses may weaken adhesion. It is equally important to investigate the fatigue and impact resistance of these reinforced panels, given that IMOCA hulls are regularly subjected to slamming loads and high-cycle fatigue. Furthermore, incorporating delamination and crushing mechanisms into advanced numerical models would provide a more realistic representation of failure behaviour and guide safer, more efficient hull design.

Together, these future research directions will refine the performance and reliability of wooden bicycles and IMOCA sandwich structures, strengthening their potential as sustainable alternatives in high-performance transport engineering.

REFERENCES

- [1] M. Z. Ahmed, “A Technical Seminar report on Material, Design & Analysis of a Bicycle Frame 2014 GURU NANAK INSTITUTIONS TECHNICAL CAMPUS Department of Mechanical Engineering.”
- [2] S. T. Rassia and T. E. Tsikis, “Wooden Boats and our ‘Smart Sea Energy Gene’: an Evolutionary Approach to Naval Architecture and Marine Engineering through History, Optimization, Renewable Energy, and Sustainability,” Sep. 01, 2020, *Springer International Publishing*. doi: 10.1007/s43069-020-00018-z.
- [3] B. Castanié *et al.*, “Wood and Plywood as eco-materials for sustainable mobility: a review,” 2023. [Online]. Available: <https://www.sciencedirect.com/science/article/pii/S0263822323011364>
- [4] Eurostat, “Final energy consumption in transport – detailed statistics,” Eurostat Statistics Explained. Accessed: Jul. 28, 2025. [Online]. Available: https://ec.europa.eu/eurostat/statistics-explained/index.php?title=Final_energy_consumption_in_transport_-_detailed_statistics
- [5] European Environment Agency, “Greenhouse gas emissions from transport in Europe,” EEA — Transport and mobility. Accessed: Jul. 28, 2025. [Online]. Available: https://www.eea.europa.eu/en/analysis/publications/sustainability-of-europes-mobility-systems/climate?utm_source=chatgpt.com
- [6] “HCC_RA_2024-web-1”.
- [7] European Parliament, “CO2 emissions from cars: facts and figures (infographics),” European Parliament. Accessed: Jul. 29, 2025. [Online]. Available: <https://www.europarl.europa.eu/topics/en/article/20190313STO31218/co2-emissions-from-cars-facts-and-figures-infographics>
- [8] D. E. Kretschmann, “Wood Handbook, Wood as an Engineering Material,” 2010.
- [9] G. R. Muñoz and A. R. Gete, “Relationships between mechanical properties of oak timber (*Quercus robur* L.),” *Holzforschung*, vol. 65, no. 5, pp. 749–755, Aug. 2011, doi: 10.1515/HF.2011.053.
- [10] D. Varner -Michal and Č.-P. Dostál, “WOOD SPECIMENS UNDER STATIC BENDING LOAD: PROPERTIES AND BEHAVIOR.”

-
- [11] N. Ayrimis, U. Buyuksari, and N. As, “Bending strength and modulus of elasticity of wood-based panels at cold and moderate temperatures,” *Cold Reg Sci Technol*, vol. 63, no. 1–2, pp. 40–43, Aug. 2010, doi: 10.1016/j.coldregions.2010.05.004.
- [12] M. G. Carmona Uzcategui, R. D. Seale, F. José, and N. França, “Oak property factors,” 2020.
- [13] S. Baliram, G. Nithisha, S. Ganesh, Y. Divya, M. Praneeth Kumar, and A. Professor, “Characterization of GFRP Material,” 2021.
- [14] I. M. Brabec and I. V. Sebera, “ANALYSIS OF THE MECHANICAL BEHAVIOUR OF WOOD BY MEANS OF DIGITAL IMAGE CORRELATION DOCTORAL THESIS,” 2016.
- [15] C. Blanco, J. M. Cabrero, A. Martin-Meizoso, and K. G. Gebremedhin, “Design oriented failure model for wood accounting for different tensile and compressive behavior,” *Mechanics of Materials*, vol. 83, pp. 103–109, 2015, doi: 10.1016/j.mechmat.2015.01.001.
- [16] R. Hartmann and F. Puch, “Numerical Simulation of the Deformation Behavior of Softwood Tracheids for the Calculation of the Mechanical Properties of Wood–Polymer Composites,” *Polymers (Basel)*, vol. 14, no. 13, Jul. 2022, doi: 10.3390/polym14132574.
- [17] Ebhojiaye RS and Eboigbe CI, “DESIGN OF BAMBOO-MADE BICYCLE STRUCTURE.”
- [18] A. International and files indexed by mero, “Standard Test Method for Flexural Properties of Unreinforced and Reinforced Plastics and Electrical Insulating Materials by Four-Point Bending 1.”
- [19] K. İnce and O. Gül, “Bicycle Frame Design And Structural Analysis.” [Online]. Available: <http://as-proceeding.com/:Konya,Turkeyhttps://www.icaens.com/>
- [20] A. Chaikittiratana, S. Pornpeerakeat, K. Suwanpakpraek, S. Limrungruengrat, and J. Dietz-Röthlingshöfer, “Bicycle frame from hemp fibre filament wound composites,” *Technologies for Lightweight Structures (TLS)*, vol. 3, no. 1, Nov. 2020, doi: 10.21935/tls.v3i1.133.
- [21] J. Vanwalleghem, I. De Baere, M. Loccufier, and W. Van Paepegem, “Development of a test rig and a testing procedure for bicycle frame stiffness measurements,” *Sports Engineering*, vol. 21, no. 2, pp. 75–84, Jun. 2018, doi: 10.1007/s12283-017-0248-8.
- [22] M. G. Wong and M. L. Hull, “Analysis of road induced loads in bicycle frames,” *Journal of Mechanical Design, Transactions of the ASME*, vol. 105, no. 1, pp. 138–145, 1983, doi: 10.1115/1.3267336.

- [23] “Cycles-Safety requirements for bicycles-Part 6: Frame and fork test methods,” 2023.
- [24] J. Vanwalleghem, I. De Baere, M. Loccufier, and W. Van Paepegem, “Development of a multi-directional rating test method for bicycle stiffness,” in *Procedia Engineering*, Elsevier Ltd, 2014, pp. 321–326. doi: 10.1016/j.proeng.2014.06.055.
- [25] L. Regenwetter, C. Weaver, and F. Ahmed, “FRAMED: An AutoML Approach for Structural Performance Prediction of Bicycle Frames,” Dec. 2022, [Online]. Available: <http://arxiv.org/abs/2201.10459>
- [26] T. A. Williams, “Influence of Frame Stiffness and Rider Position on Bicycle Dynamics: An Analytical Study.” [Online]. Available: <http://dc.uwm.edu/etd>
- [27] K. Khutal, B. Simhachalam, and D. D. Jebaseelan, “ScienceDirect Design Validation Methodology for Bicycle Frames Using Finite Element Analysis,” 2020. [Online]. Available: www.sciencedirect.com
- [28] A. Kausar, I. Ahmad, S. A. Rakha, M. H. Eisa, and A. Diallo, “State-Of-The-Art of Sandwich Composite Structures: Manufacturing—to—High Performance Applications,” Mar. 01, 2023, *MDPI*. doi: 10.3390/jcs7030102.
- [29] H. Xie, H. Fang, W. Cai, L. Wan, R. Huo, and D. Hui, “Development of an innovative composite sandwich matting with GFRP facesheets and wood core,” *Reviews on Advanced Materials Science*, vol. 60, no. 1, pp. 80–91, Jan. 2021, doi: 10.1515/rams-2021-0016.
- [30] J. Susainathan, F. Eyma, E. De Luycker, A. Cantarel, and B. Castanie, “Manufacturing and quasi-static bending behavior of wood-based sandwich structures,” *Compos Struct*, vol. 182, pp. 487–504, Dec. 2017, doi: 10.1016/j.compstruct.2017.09.034.
- [31] A. Peignon, J. Serra, L. Gélard, A. Cantarel, F. Eyma, and B. Castanié, “Mode I delamination R-Curve in poplar laminated veneer lumber 1,” 2023.
- [32] A. Peignon, J. Serra, A. Cantarel, F. Eyma, and B. Castanié, “Toward the modelling of laminated veneer lumber stiffness and the influence of the number of plies,” *Wood Sci Technol*, vol. 58, no. 3, pp. 1111–1139, May 2024, doi: 10.1007/s00226-024-01558-x.
- [33] S. K. Sahu, P. S. R. Sreekanth, and S. V. K. Reddy, “A Brief Review on Advanced Sandwich Structures with Customized Design Core and Composite Face Sheet,” Oct. 01, 2022, *MDPI*. doi: 10.3390/polym14204267.
- [34] H. Hadiji, J. Serra, R. Curti, D. Gebrehiwot, and B. Castanié, “Characterization of mode II delamination behaviour of poplar plywood and LVL,” *Theoretical and Applied Fracture Mechanics*, vol. 131, Jun. 2024, doi: 10.1016/j.tafmec.2024.104354.

- [35] Dassault Systèmes, “CATIA V5,” 2023, *Dassault Systèmes: V5*. Accessed: Sep. 13, 2025. [Online]. Available: <https://www.3ds.com>
- [36] Dassault Systèmes Simulia, “Abaqus/CAE,” 2022, *Dassault Systèmes, Providence, RI, USA: 2022*. Accessed: Sep. 15, 2025. [Online]. Available: <https://www.3ds.com>
- [37] D. E. Kretschmann, “Wood Handbook, Wood as an Engineering Material,” 2010.
- [38] S. Gambarelli, J. Bošnjak, R. N. Fararoni Platas, and K. Jin, “Experimental Study on Mechanical Properties of European Oak and Norway Spruce Clear Wood,” *Materials*, vol. 18, no. 14, Jul. 2025, doi: 10.3390/ma18143257.
- [39] Resoltech, “Resoltech 8050 Structural Epoxy Adhesive.” Accessed: Aug. 12, 2025. [Online]. Available: <https://www.resoltech.com/en/markets/8050-detail.html>
- [40] Mack Kayak, “Roving 300 grammes.” Accessed: Aug. 12, 2025. [Online]. Available: <https://www.mack-kayak.com/tissus-de-verre-lins-feutres/555-roving-300-grammes.html>
- [41] AZoM, “E-Glass Fibre Properties.” Accessed: Aug. 14, 2025. [Online]. Available: <https://www.azom.com/properties.aspx?ArticleID=764>
- [42] “Processing/How to use General Information.” [Online]. Available: <https://www.westlakeepoxy.com/en-US/product/epon-resin-828>
- [43] G. Magnani, “The Simplest Bicycle Framebuilding Jig I Could Come Up With.” Accessed: Aug. 15, 2025. [Online]. Available: <https://www.instructables.com/The-simplest-bicycle-framebuilding-jig-I-could-com/>
- [44] “Test Methods for Flexural Properties of Unreinforced and Reinforced Plastics and Electrical Insulating Materials,” Jul. 01, 2017, *ASTM International, West Conshohocken, PA*. doi: 10.1520/D0790-17.
- [45] A. International and files indexed by mero, “Designation: D 3039/D 3039M-00 e1 Standard Test Method for Tensile Properties of Polymer Matrix Composite Materials 1.”
- [46] A. International and files indexed by mero, “Standard Test Method for Flexural Properties of Sandwich Constructions 1.”
- [47] B. M. Icten, C. Atas, M. Aktas, and R. Karakuzu, “Low temperature effect on impact response of quasi-isotropic glass/epoxy laminated plates,” *Compos Struct*, vol. 91, no. 3, pp. 318–323, Dec. 2009, doi: 10.1016/j.compstruct.2009.05.010.
- [48] R. Rolfes, G. Ernst, D. Hartung, and J. Teßmer, “Strength of Textile Composites — A Voxel Based Continuum Damage Mechanics Approach,” in *III European Conference on Computational Mechanics*, Springer Netherlands, 2008, pp. 32–32. doi: 10.1007/1-4020-5370-3_32.

- [49] D. Plappert, G. C. Ganzenmüller, M. May, and S. Beisel, “Mechanical properties of a unidirectional basalt-fiber/epoxy composite,” *Journal of Composites Science*, vol. 4, no. 3, 2020, doi: 10.3390/jcs4030101.
- [50] L. Parnas and N. Katirci, “Design of fiber-reinforced composite pressure vessels under various loading conditions,” *Compos Struct*, vol. 58, no. 1, pp. 83–95, Oct. 2002, doi: 10.1016/S0263-8223(02)00037-5.
- [51] P. D. Soden, B. A. Adeyefa, Y. S. Wong, and M. A. Millar, “Loads, Stresses, and deflections in Bicycle Frames,” *J Strain Anal Eng Des*, vol. 21, no. 4, pp. 185–195, Oct. 1986, doi: 10.1243/03093247V214185.
- [52] M. Dvořák *et al.*, “Experimental Development of Composite Bicycle Frame,” *Applied Sciences (Switzerland)*, vol. 12, no. 16, Aug. 2022, doi: 10.3390/app12168377.

ANNEX I

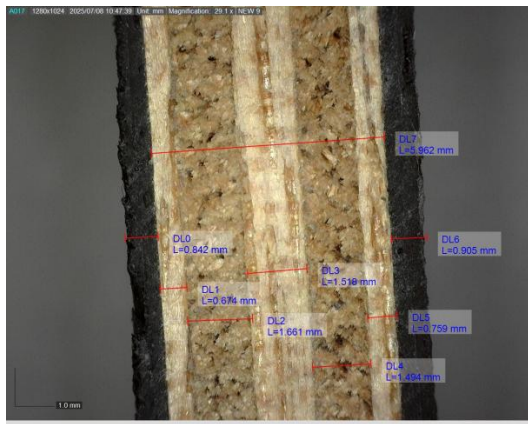


FIGURE 5.2: B1 B45 T10



FIGURE 5.3: B1 BOIS F3 5

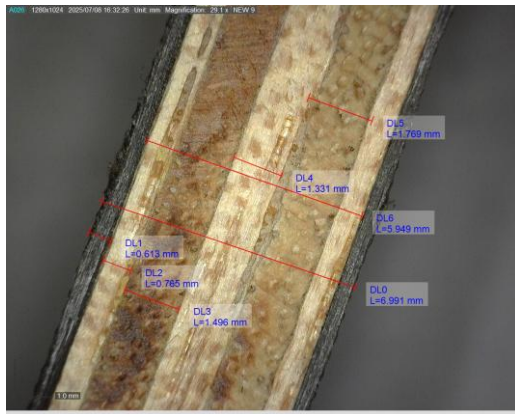


FIGURE 5.4: B2 B0 T5

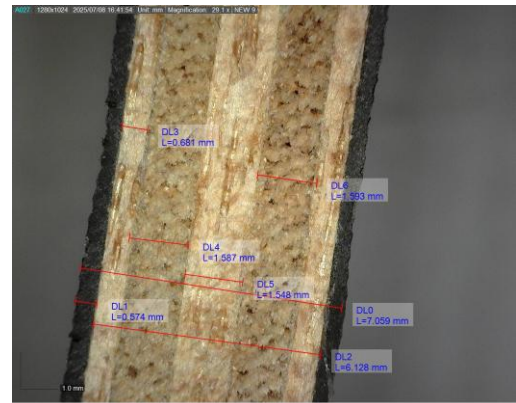


FIGURE 5.5: B3 B90 F3 10

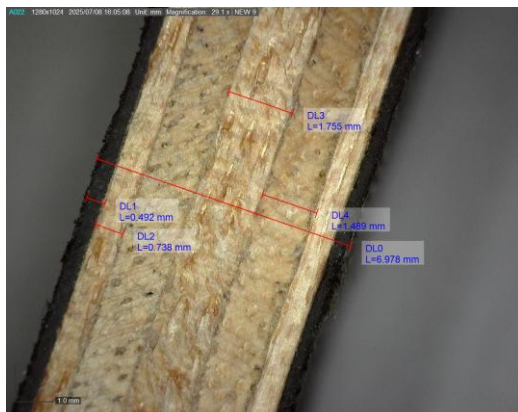


FIGURE 5.6: B3 B90 F4 5

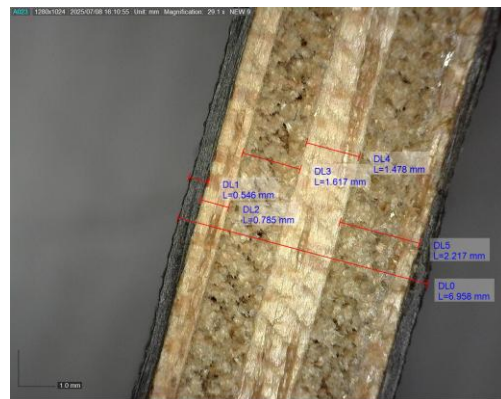


FIGURE 5.7: B4 B0 F3 10

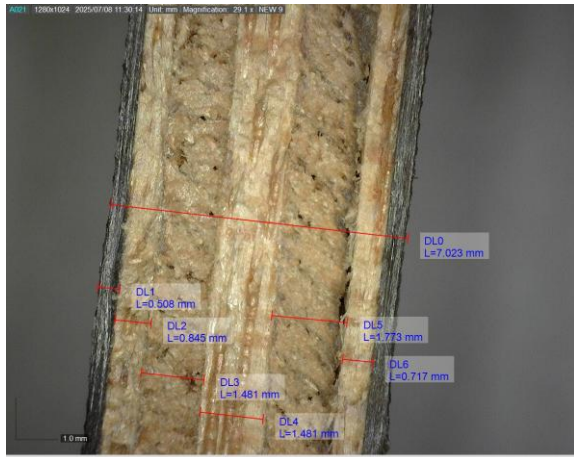


FIGURE 5.8: B4 BO F4 5

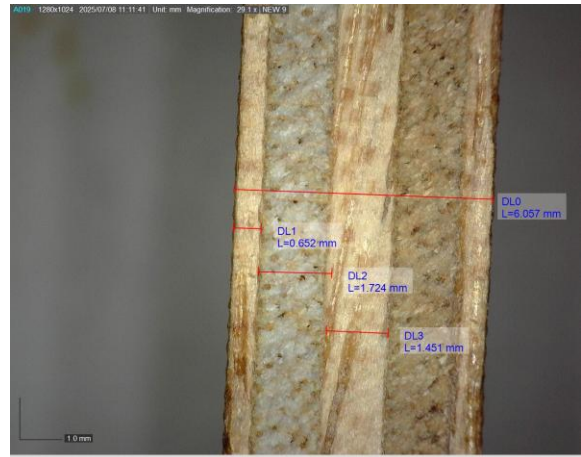


FIGURE 5.9: C1 BOIS F4 6

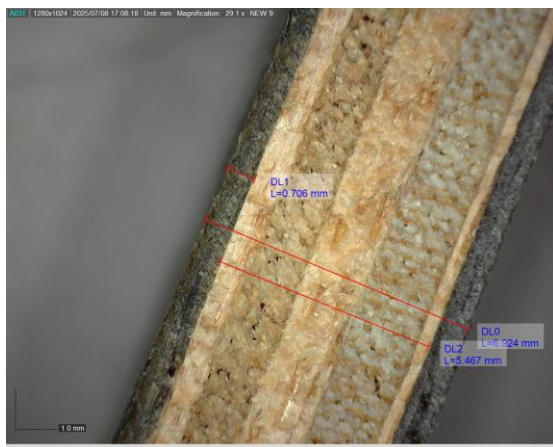


FIGURE 5.10: C1 C45 T5

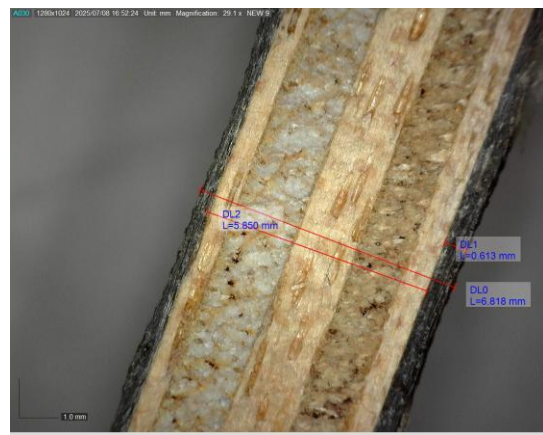


FIGURE 5.11: C2 C0 T1

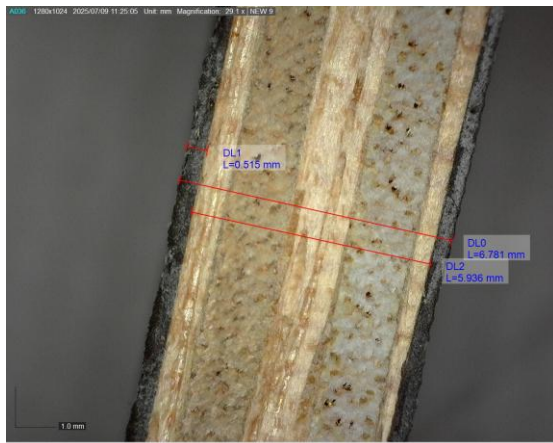


FIGURE 5.12: C2 C90 T9

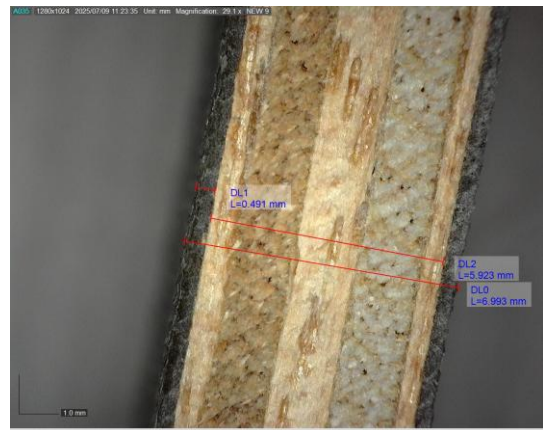


FIGURE 5.13: C3 C90 F3 5

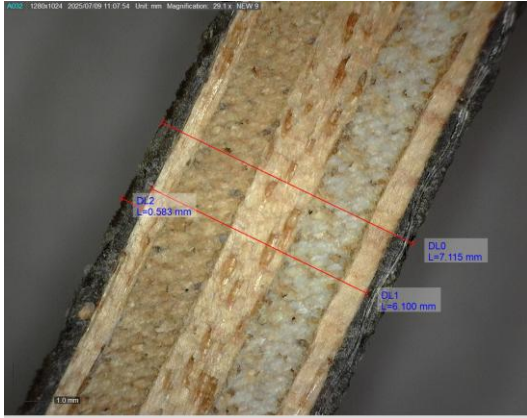


FIGURE 5.14: C3 C90 F4 TEST

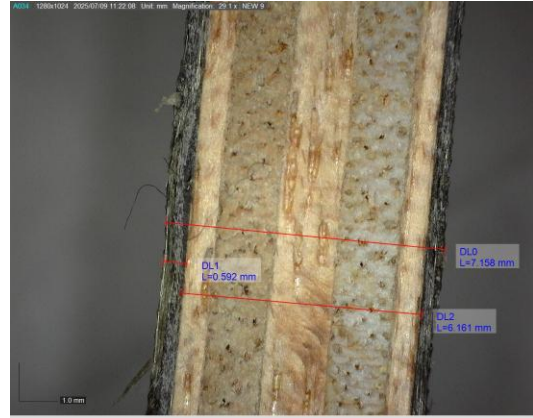


FIGURE 5.15: C4 C0 F3 10

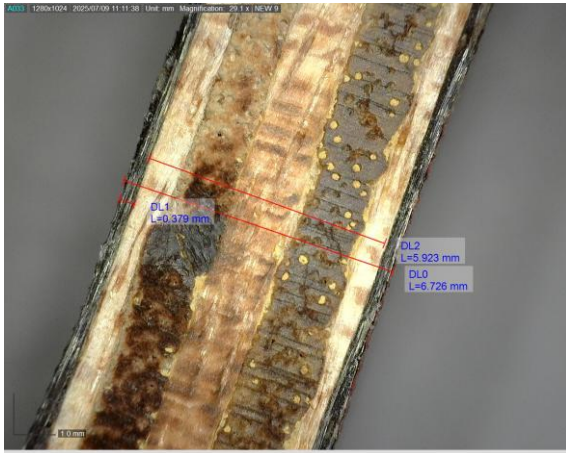


FIGURE 5.16: C4 C0 F4 5

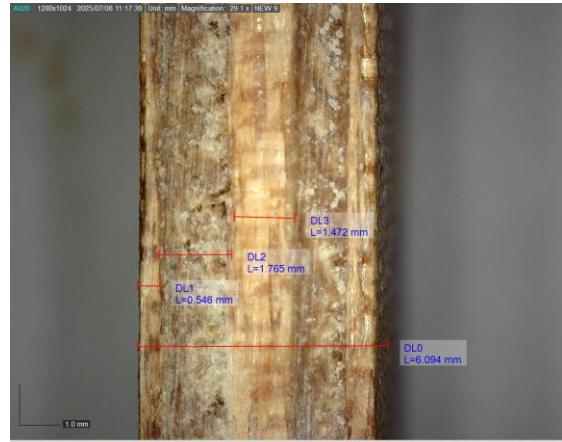


FIGURE 5.17: CPO T10

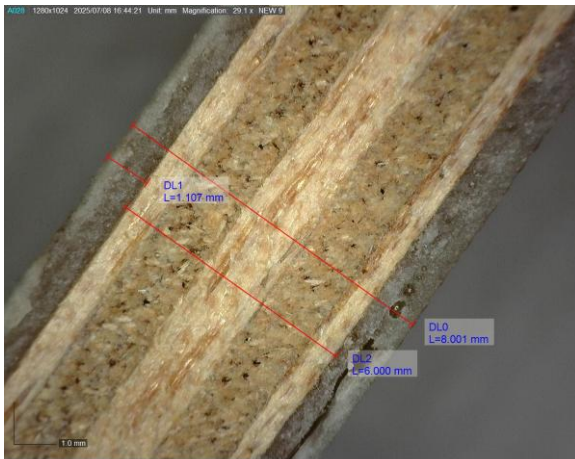


FIGURE 5.18: V1 V45 T1

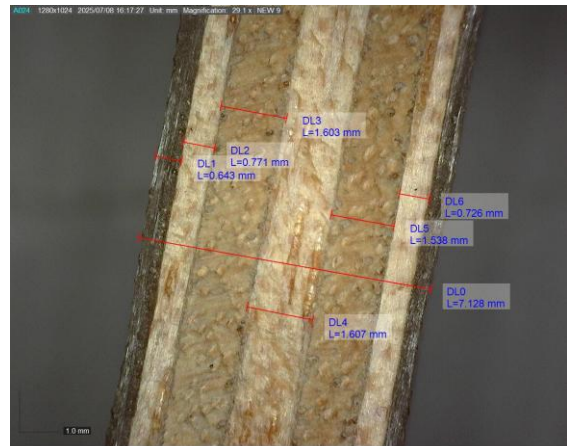


FIGURE 5.19: V2 V0 T5



FIGURE 5.20: V3 V90 F3 6

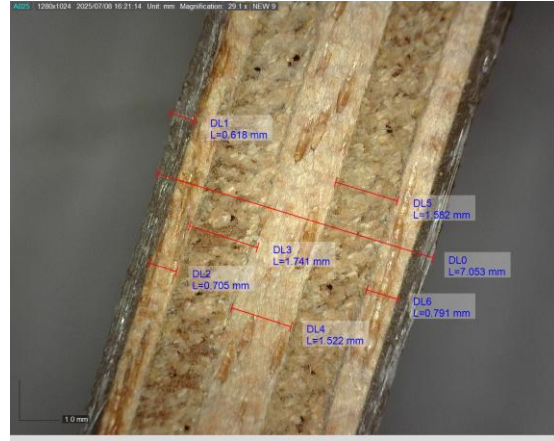


FIGURE 5.21: V4 V0 F3 5

ANNEX II

Tsai-wu Custom python code for Head-Tube Assessment

```
import pandas as pd

# === Step 1: Load the CSV ===
csv_path = r"C:\temp\My thesis\Bike Frame Project\Head Tube Stiffness\Head Tube with Laminate\HT_2 Post_Processing\HT_with_Lam.csv"
df = pd.read_csv(csv_path, low_memory=False) # avoids the dtype warning

# === Step 2: Clean headers ===
df.columns = df.columns.str.strip()
df = df.rename(columns={
    "S-S11": "S11",
    "S-S22": "S22",
    "S-S33": "S33",
    "S-S12": "S12",
    "S-S13": "S13",
    "S-S23": "S23",
    "Element Label": "Element"
})

# === Step 3: Convert stress columns to float ===
stress_cols = ["S11", "S22", "S33", "S12", "S13", "S23"]
for col in stress_cols:
    df[col] = pd.to_numeric(df[col], errors='coerce') # handles text and blanks safely

# Optional: Remove rows with NaN stress values (if any)
df.dropna(subset=stress_cols, inplace=True)

# === Step 4: Define Material Strengths (Oak Wood) ===
S1T, S1C = 80, 45 # Along grain tension/compression
S2T, S2C = 8.7, 6.4 # Transverse 1
S3T, S3C = 8.7, 6.4 # Transverse 2 (assuming same as direction 2)
S12 = 13.2
S13 = 13.2
S23 = 13.2

# === Step 5: Define Tsai-Wu Coefficients for 3D ===
F1 = (1/S1T) - (1/S1C)
F2 = (1/S2T) - (1/S2C)
F3 = (1/S3T) - (1/S3C)
F11 = 1 / (S1T * S1C)
F22 = 1 / (S2T * S2C)
F33 = 1 / (S3T * S3C)
```

```

F44 = 1 / (S23**2)
F55 = 1 / (S13**2)
F66 = 1 / (S12**2)
F12 = -1 * (F11 * F22)**0.5
F13 = -1 * (F11 * F33)**0.5
F23 = -1 * (F22 * F33)**0.5

# === Step 6: Define Tsai-Wu Failure Index Function for 3D ===
def tsai_wu_3d(s1, s2, s3, t23, t13, t12):
    return (
        F1 * s1 + F2 * s2 + F3 * s3 +
        F11 * s1**2 + F22 * s2**2 + F33 * s3**2 +
        F44 * t23**2 + F55 * t13**2 + F66 * t12**2 +
        2 * F12 * s1 * s2 + 2 * F13 * s1 * s3 + 2 * F23 * s2 * s3
    )

# === Step 7: Compute Failure Index ===
df["TsaiWuIndex"] = df.apply(lambda row: tsai_wu_3d(
    row["S11"], row["S22"], row["S33"],
    row["S23"], row["S13"], row["S12"]
), axis=1)

# === Step 8: Classify Elements ===
df["Result"] = df["TsaiWuIndex"].apply(lambda val: "FAIL" if val > 1 else
"PASS")

# === Step 9: Save Failed Elements ===
failed = df[df["Result"] == "FAIL"]["Element"].drop_duplicates().astype(int)
failed_str = ", ".join(map(str, failed.tolist()))

output_txt = r"C:\temp\My thesis\Bike Frame Project\Head Tube Stiffness\Head
Tube with Laminate\HT_2 Post_Processing\HTfailed_elements_comma.txt"
with open(output_txt, "w") as f:
    f.write(failed_str)

# === Step 10: Summary Output ===
print(f"\n✓ Tsai-Wu evaluation complete.")
print(f"→ Total elements evaluated: {len(df)}")
print(f"→ Failed elements: {len(failed)}")
print(f"→ Failed element IDs saved to:\n{output_txt}")

```

